NASA-CR-204341

Improved Finite Element Modeling of the Turbofan Engine Inlet Radiation Problem

Indranil Danda Roy and Walter Eversman
University of Missouri—Rolla
Mechanical and Aerospace Engineering and Engineering Mechanics

H. D. Meyer
United Technologies Corporation
Hamilton Standard

April 1993

NASA

National Aeronautics and
Space Administration

ABSTRACT

Improvements have been made in the finite element model of the acoustic radiated field from a turbofan engine inlet in the presence of a mean flow. The problem of acoustic radiation from a turbofan engine inlet is difficult to model numerically because of the large domain and high frequencies involved. A numerical model with conventional finite elements in the near field and wave envelope elements in the far field has been constructed. By employing an irrotational mean flow assumption, both the mean flow and the acoustic perturbation problem have been posed in an axisymmetric formulation in terms of the velocity potential, thereby minimizing computer storage and time requirements. The finite element mesh has been altered in search of an improved solution. The mean flow problem has been reformulated with new boundary conditions to make it theoretically rigorous. The sound source at the fan face has been modeled as a combination of positive and negative propagating duct eigenfunctions. Therefore, a finite element duct eigenvalue problem has been solved on the fan face and the resulting modal matrix has been used to implement a source boundary condition on the fan face in the acoustic radiation problem. In the post processing of the solution, the acoustic pressure has been evaluated at Gauss points inside the elements and the nodal pressure values have been interpolated from them. This has significantly improved the results. The effect of the geometric postion of the transition circle between conventional finite elements and wave envelope elements has been studied and it has been found that the transition can be made nearer to the inlet than previously assumed.

TABLE OF CONTENTS

LIST OF ILLUSTRATIONS

I. INTRODUCTION

A. BACKGROUND

The two predominant sources of noise in a modern jet engine are the jet noise and the fan noise. While jet noise provides a challenging opportunity for research involving highly non-linear thermal and turbulence effects, the study of fan noise has become equally important with the use of high bypass ratio turbofan engines in civil aircraft. Although the bypass design has considerably reduced the intensity of jet noise by lowering the jet velocity, there is a significant forward sound propagation from the fan. This forward radiated acoustic field propagates through the inlet duct to be radiated to the far field. Therefore the acoustic analysis of this forward propagating noise involves the noise generation by the fan, propagation inside the inlet cowling and radiation from the inlet to the far field. This radiated acoustic field is highly directional in character with its directivity dependent upon the frequency, the mode of the internally propagated acoustic waves, the inlet geometry and the mean flow in and around the inlet. The purpose of this work is to improve the modeling of the far field acoustical radiation from jet engine inlets in low Mach number flows using the finite element method.

The mathematical modeling of the radiation of turbofan generated noise is complicated by the fact that the wavelength of sound radiated may be much smaller than the characteristic dimension of the inlet. To resolve the variation in acoustic properties near the inlet, it is obvious that a fine mesh must be generated. Further complications arise from the fact that sound is radiated to an infinite domain and also because of the presence of a mean flow around the inlet.

The geometries involved in a turbofan engine inlet do not permit a classical analytical closed form solution, except when extremely simplified assumptions are

1

made. A wide range of numerical techniques, which have been successfully used in duct acoustics, can be thought of as an alternative. These include the Finite Element Method (FEM), the Method of Weighted Residuals (MWR), and the Finite Difference Method (FDM). Based on previous experience, the FEM showed promise in the acoustic radiation problem, provided there was a way to model the infinite domain effectively. Fortunately, there has been much work to date in duct acoustics which relates to the generation and propagation of noise inside the duct. The propagation of sound in the external region, which extends from the throat of the inlet to the far field, presents a more challenging computational problem and involves the imposition of proper radiation type boundary conditions at a finite but distant boundary. In this investigation, the radiation boundary condition is imposed by the use of wave envelope elements in the far field.

B. LITERATURE REVIEW

The theory relevant to this problem spans many fields in acoustics. Rather than discussing each one of them, this section emphasizes the contribution in the areas which have a direct link with the problem. Special focus is on duct acoustics and the inlet/radiation problem.

In most practical problems concerning the propagation of sound in ducts, no analytical solution is possible, unless extremely simple geometries and assumptions are considered. Therefore, the three main numerical techniques which have been used in analysis are the Finite Element Method (FEM), the Method of Weighted Residuals (MWR) and the Finite Difference Method (FDM).

Finite element methods have been sucessfully used to model various problems in duct acoustics. Astley and Eversman [1], and Eversman, Astley and Thanh [2] studied area variation in two dimensions and axisymmetric ducts with different

2

FEM formulations and compared them with MWR results. Majjigi, Sigman and Zinn [3] used various types of finite elements in the study of simple hard walled acoustically treated ducts and compared with results produced by a FDM formualtion. Various FEM methods have been used to solve the acoustics problem with a mean flow. Tag and Lumsdaine [4] used a formulation based on velocity potential to save disk storage, while Baumeister [5] indicated that the assumption of irrotational acoustic perturbation is valid only for an irrotational mean flow.

The Method of Weighted Residuals techniques in duct acoustics has been useful in situations where appropriate basis functions are obtainable such as hard walled or lined ducts with or without flow. Eversman, Astley and Thanh [2] compared the results of MWR and FEM methods as mentioned earlier. Eversman and Astley [6] investigated the accuracy of MWR compared to exact calculations of acoustic transmission based on a one dimensional model for nonuniform ducts containing high speed subsonic flow.

Finite difference methods have not been used extensively in acoustics. However, in non-linear problems, for simplified one dimensional models, it seems to have a distinct advantage over MWR and FEM. Walkington and Eversman [7] studied shocked acoustic waves with a one dimensional model using FDM methods. Walkington [8] proposed several schemes to formulate such problems, but suggested that extension of the non-linear problem to higher dimensions would be difficult.

The following discussion highlights previous investigations carried out in the field of inlet acoustics and the radiation problem. Most work involving inlet acoustics has been experimental in nature, however recently some numerical comparisons have been made. Ville and Silcox [9], and Silcox [10] presented experimental results for some standard inlets used by NASA for different flow and geometry

3

configurations. Several analytical and numerical methods have been proposed to solve the inlet acoustics problem. Ray acoustics theory (for example Kempton and Smith [11]) has been combined with numerical flow solutions to analyze various inlet geometries. Meyer, Bell and Zinn [12] considered inlet shape and liner design by computing far field directivities by an integral method. They numerically solved a Helmholtz equation and made an effort not to decouple the far field and inlet solutions. Meyer, Daniel and Zinn [13] used the same method as described in reference [12] and gave comparisons with experimental results for radiation from a pipe and a jet engine inlet. For further improvement, Horowitz, Sigman and Zinn used a hybrid FEM-integral technique for cases without mean flow [14], then extended this to cases involving mean flow [15]. The technique uses a FEM formulation to analyse the duct interior and then an integral formulation for the far field. By guessing a duct exit impedance and solving a duct problem, the far field radiation is solved using a Green's function. The outer boundary impedance is then compared to a Sommerfeld condition and the exit impedance is corrected iteratively until the results converge. Baumeister [16] used these methods to compare with experimental data for a JT15D engine under static conditions with a low Mach number flow into the inlet.

The iterative procedure proposed by Zinn et al. turns out to be lengthy and costly in terms of both computational time and storage. To overcome this problem, Astley and Eversman [17] employed FEM, wave envelope and infinite element formulations, and succesfully modeled the sound field for a one dimensional test case with no flow. The concept of infinite elements, where the element shape functions simulate decay to model an infinite domain, was first proposed by Bettess [18] in 1977. The application of infinite elements to wave propagation was significant, but Astley and Eversman found that "wave envelope" elements, which simulate

4

wavelike behavior in their interpolation functions, model far field acoustic radiation better than infinite elements. In [19] they laid the foundation for using wave envelope elements for inlet radiation in the presence of a flow. They emphasized that the use of wave envelope elements relies on the assumption that in the far field the sound field approximates that produced by a point source. This allows for a coarse mesh in the far field thereby drastically reducing the computational time and storage requirements. Astley [20] then validated the concept with simple test cases.

This work is an extension to that done by Eversman, Parrett, Preisser and Silcox [21], where they have presented several contributions to finite element modelling of acoustic radiation from turbofan inlets. This included the use of a technique combining finite elements in the near field and wave envelope elements in the far field. The use of a frontal solution scheme of Irons [22] resulting in drastic reduction of in-core storage was also significant. The numerical results were verified by comparison with both model scale [10] and full scale [23] test data.

C. ENHANCEMENTS OF THE TURBOFAN FINITE ELEMENT MODEL

The finite element model of the jet engine inlet developed in [21] had some shortcomings which have been addressed in this study. The finite element mesh of the original model had elements whose aspect ratios[1] were not properly maintained. The zone of conventional finite elements outside of the nacelle was originally generated in two adjacent regions. This was found to be superfluous and was therefore reduced to a single region. In this single region, conventional eight-node isoparametric finite elements were generated with their radial thicknesses

---

[1]Aspect ratio of a two dimensional finite element is the ratio of any two adjacent sides of an element. Rule of thumb says that it should not be more than 4:1 to be on the safe side.

increasing in geometric progression, thereby maintaining aspect ratios of the elements below the safe allowable value.

The time invariant mean flow problem of the model has a Laplace's differential equation with Neumann boundary conditions and the previous solution technique to this problem was not theoretically rigorous. The boundary conditions of the problem have been modified and a proper solution technique has been incorporated.

A finite element duct eigenvalue problem has been solved on the fan face mesh and the resulting finite element modal matrix has been used to model the acoustic potential at the fan face boundary as a combination of incident and reflected uniform duct eigenfunctions. This boundary condition has been implemented in the acoustic radiation problem.

The problem has been set up with both eight and nine-node quadratic isoparametric elements and results from both the cases have been compared. In the post-processing of the solution, the acoustic pressure was observed to be discontinuous across inter-element boundaries. This is expected because it can be shown that the acoustic potential solution is continuous across inter-element boundaries, but its derivative is not. In the original model, the acoustic pressure at a node was calculated from the four elements sharing that node and the value of the pressure at that node was defined as the average of the these four values. This technique gave inadequate results. The improved model evaluates acoustic pressure at gauss points inside the element and interpolates the pressure from the interior points to the nodes. This has resulted in significantly better results.

The position of the transition circle, which separates the conventional finite element region in the near field and the wave envelope region in the far field, was

6

seen to be creating a significant effect on the final results. It was found out that the wave envelope elements were not only capable of modeling the far field but also the moderately near field outside the nacelle. Therefore, the transition circle could be brought in much closer to the inlet than thought before, and this has lead to better results with drastic reduction in the number of degrees of freedom. This is probably the most significant result of this study.

II. THEORETICAL FOUNDATIONS

A. THE PROBLEM

The problem posed here is that of a stationary turbofan inlet with internal and external mean flow. The results obtained are applicable for an observer fixed to the inlet. For an observer on the ground, Doppler shift corrections have to be applied to obtain the proper results.

The turbofan inlet is assumed to be axially symmetric, as is the flow field in and around the inlet. The acoustic field generated within the inlet and radiated to the far field is generally not axially symmetric, but is conveniently expressed in terms of Fourier components in the angular coordinate. Therefore, it is appropriate to express the inlet geometry and the entire computational domain in a cylindrical coordinate system.

Figure 1 shows the top half of the symmetric inlet geometry in an x-r plane. The surface C_n is the nacelle. The nacelle is regarded impervious to both steady flow and acoustic perturbations. The surface C_f (fan plane) is the one on which the sound source, i.e. the turbofan, is defined (it may or may not have a center-body). The acoustic pressure field on the fan face is modelled as a combination of incident and reflected (positive and negative) uniform duct eigenfunctions. The surface C_b (baffle surface) is a boundary of the computational region which for a completely accurate representation would be the negative x-axis. However, in order to decrease the size of the domain, and also to avoid modeling the rear of the engine, C_b is chosen at least 90° past the direction of maximum acoustic radiation. It may be thought of as a baffle which would admit flow through, yet interfere with the forward radiated acoustic field minimally. The boundary C_∞ is the outer boundary of the computational domain in the far field such that at points on C_∞
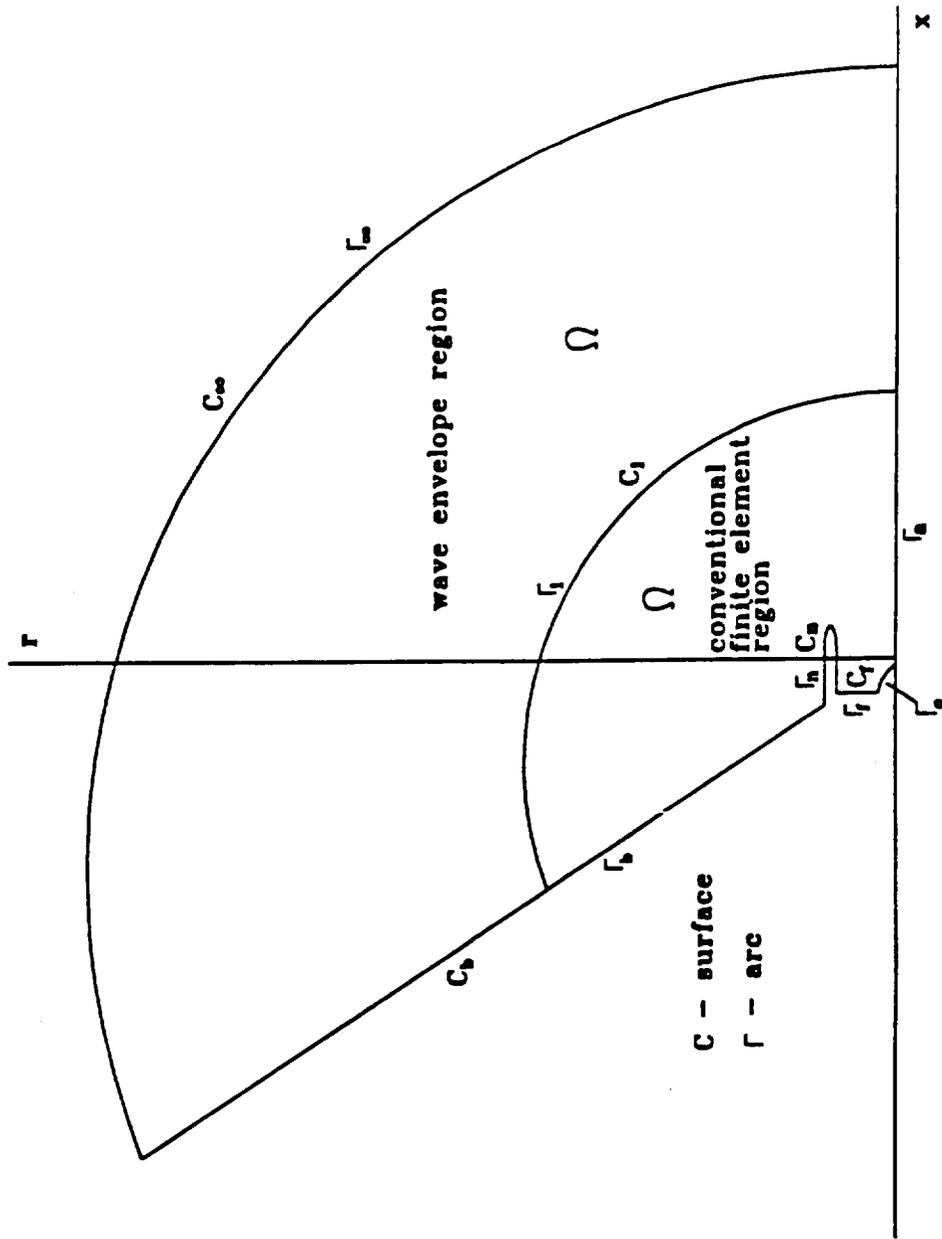
Figure 1: Computational domain

C — surface
Γ — arc

9

the acoustic field can be viewed locally as propagating plane waves. Thus the computational domain is made finite by imposition of a suitable radiation boundary condition at a distant but finite boundary. The boundary C_∞ should be several duct radii from the inlet. The large domain and the fine mesh near the inlet gives rise to very large number of degrees of freedom in the finite element model. The boundary conditions will be dealt with in more detail in a later section.

To minimize the problem of huge data storage, an axisymmetric formulation based on velocity potential has been adopted, thereby reducing the number of unknowns to one per node. The assumptions of an inviscid fluid and also that of an irrotational flowfield has been made (both in steady flow and acoustic perturbations). The mean flowfield is assumed to be steady, uniform, of low Mach number and parallel to the centerline of the engine. These assumptions are quite valid for a jet engine during take off or landing approaches.

B. THE FIELD EQUATIONS

This sub-section outlines the derivation of the steady mean flow and acoustic field equations. It is assumed that the medium is inviscid and non heat conducting and that all the processes are isentropic. The field equations have been derived in non-dimensional form. Reference density ρ_r and reference speed of sound c_r are defined at a large distance from the inlet. The reference length is taken as the duct radius R. Pressure is non-dimensionalized by $\rho_r c_r^2$, density by ρ_r, velocities and speed of sound by c_r, velocity potential by $c_r R$ and time by R/c_r.

The governing equations for the problem may be written in nondimensional form as

Mass conservation :

$$\frac{\partial \rho'}{\partial t'} + \nabla \bullet (\rho' \mathbf{V}') = 0 \tag{1}$$

Momentum conservation :

$$\frac{\partial \mathbf{V}'}{\partial t'} + (\mathbf{V}' \bullet \nabla)\mathbf{V}' = -\frac{1}{\rho'}\nabla p' \tag{2}$$

Equation of state :

$$p' = \left(\frac{1}{\gamma}\right)(\rho')^\gamma \tag{3}$$

where γ is the ratio of specific heats. The non-dimensional speed of sound can be written as

$$(c')^2 = \frac{\gamma p'}{\rho'} = (\rho')^{\gamma-1} \tag{4}$$

C. VELOCITY POTENTIAL FORMULATION

As stated previously, a velocity potential formulation has been proposed to reduce the computational time and storage requirements. Since the flow field is assumed to be irrotational, the non-dimensional velocity $\mathbf{V}'$ can be related to the non-dimensional velocity potential Φ' by

$$\mathbf{V}' = \nabla \Phi' \tag{5}$$

The mass conservation equation (1) in terms of density and velocity potential becomes

$$\frac{\partial \rho'}{\partial t'} + \nabla \bullet (\rho' \nabla \Phi') = 0 \tag{6}$$

If it is assumed that the reference conditions are taken to be stagnation conditions, i.e. $|\mathbf{V}'| = 0$, $c' = 1$, $\partial/\partial t = 0$, the momentum equation (2) in terms of density and velocity potential may be cast as

$$(c')^2 = 1 - (\gamma - 1)[\frac{\partial \Phi'}{\partial t} + \frac{1}{2}(\nabla \Phi' \bullet \nabla \Phi')] \tag{7}$$

11

or,

$$\rho' = [1 - (\gamma - 1)\{\frac{\partial \Phi'}{\partial t} + \frac{1}{2}(\nabla \Phi' \bullet \nabla \Phi')\}]^{1/(\gamma-1)} \tag{8}$$

D. LINEARIZED PERTURBED EQUATIONS

It is assumed that the acoustic quantities consist of small perturbations superimposed on a steady mean flow field, so that

$$\Phi' = \phi_o + \phi \tag{9}$$

$$\rho' = \rho_o + \rho \tag{10}$$

where o subscript denotes the mean flow field variables and the unsubscripted ones represent the acoustic perturbation variables.

Substitution of equations (9) and (10) in equations (7) and (8) and linearization to first order in acoustic perturbations yields

$$\rho_o = [1 - \frac{(\gamma - 1)}{2}\nabla \phi_o \bullet \nabla \phi_o]^{1/(\gamma-1)} \tag{11}$$

$$\rho = -\frac{\rho_o}{c_o^2}[\frac{\partial \phi}{\partial t} + (\nabla \phi_o \bullet \nabla \phi)] \tag{12}$$

where, $c_o^2 = \rho_o^{\gamma-1}$ is the local speed of sound in the mean flow.

Similarly, linearization of the mass conservation equation (6) to first order in acoustic perturbations yields

$$\frac{\partial \rho}{\partial t} + \nabla \bullet (\rho_o \nabla \phi_o + \rho_o \nabla \phi + \rho \nabla \phi_o) = 0 \tag{13}$$

Equation (13) is a linear superposition of the mass conservation equation for the steady mean flow and the mass conservation equation for the acoustic flow. For steady mean flow

$$\nabla \bullet (\rho_o \nabla \phi_o) = 0 \tag{14}$$

12

and for acoustic perturbation

$$\frac{\partial \rho}{\partial t} + \nabla \bullet (\rho_o \nabla \phi + \rho \nabla \phi_o) = 0 \qquad (15)$$

Of the field variables, the physical quantity that can be measured for any comparison between theory and experiment is the acoustic pressure. The acoustic pressure is related to the acoustic potential through the linearized isentropic equation of state[2] by

$$p = -\rho_o [\frac{\partial \phi}{\partial t} + (\nabla \phi_o \bullet \nabla \phi)] \qquad (16)$$

Equations (12) and (15) are the basic field equations for the acoustic perturbation flow. Equation (12) can be used to eliminate ρ in equation (15) to yield a "generalized wave equation" in ϕ. Equation (16) can then be used to find the acoustic pressure field from the acoustic potential field obtained from a solution of (15). The velocity potential field of the steady mean flow needs to be computed using equation (14).

E. THE FINITE ELEMENT MESH AND WAVE ENVELOPE CONCEPT

The problems for both the mean flow and the acoustic perturbation have been solved on the same mesh using a standard Galerkin finite element procedure. This sub-section discusses the finite element mesh and introduces the concept of wave envelope elements, with the next section discussing the mesh generating scheme in detail.

As shown in Figure 1, the computational region is divided into two major regions for conveniently constructing the mesh. The curve C_1 marks the border

---

[2] The linearized isentropic equation of state is

$$p = \rho c_n^2$$

13

between these two regions. It is important to note that there is a difference in the physics involved in generating the mesh in these two regions. In the inner region, inside the curve C_1, a conventional finite element mesh based on quadratic isoparametric rectangles has been used. The mesh spacing in the general direction of noise propagation should be maintained at 4 to 5 elements per wavelength. The mesh spacing across the inlet is made fine enough to resolve the transverse modes present. In the outer region between C_1 and C_∞, a transition occurs between the fine mesh and elements which are several wavelengths long. These outer layers of elements are called wave envelope elements.

The major drawback of using a conventional finite element mesh throughout the whole domain is apparent when dealing with realistic frequencies. The variations of the shape functions of an eight or nine-node isoparametric element are quadratic in the local coordinates within each element. Several elements are therefore required to accurately represent a single wavelength variation of the solution in the radial and angular directions. For realistic frequencies, the typical far field wavelength of the acoustic field may be several orders of magnitude smaller than the overall dimension of the domain. This would demand a very fine mesh in the far field and therefore the number of degrees of freedom would become prohibitively large.

To reduce the dimensionality of the problem, wave envelope elements have been used in the outer region as an alternative. It has already been assumed that C_∞ is sufficiently far away from the inlet so that the radiated field will behave *locally* as a plane wave propagating outwards from the origin and normal to C_∞. Therefore, in the outer region, the inlet is assumed to behave as a stationary complex source in a uniform flow. Hence the acoustic field in the outer region is assumed to be propagating outward with exponential character $e^{-i\eta_r \psi(z,r)}$, where

η_r is the frequency and $\psi(x, r)$ is the phase, being constant on constant phase surfaces. The form of the constant phase surfaces can be visualized by considering a simple source in uniform flow (see Figure 2). Note that C_∞ should be at a distance from the inlet sufficient for the exterior flow field to be uniform. The constant phase surfaces are found to be

$$\psi(x, r) = \frac{-Mx + \sqrt{x^2 + \beta^2 r^2}}{\beta^2} \tag{17}$$

where $\beta^2 = 1 - M^2$. They are circles (of radius R_c) of the form

$$(x - MR_c)^2 + r^2 = R_c^2 \tag{18}$$

The Mach number M here is the Mach number of the exterior flow.

The shape/basis functions of a typical wave envelope element in the outer region are modified from the usual quadratic form to incorporate the complex exponential propagation corresponding to a locally outward travelling wave, and the reciprocal decay with distance corresponding to a simple source (the velocity potential field of a simple source varies as $1/r$ where r is the radial distance from the origin). Since the gross features of the harmonic and reciprocal decay solution are incorporated into the shape functions, the elements in the outer region are required to resolve only the discrepancy between the actual solution and the implied harmonic and amplitude variations included in the shape functions. As a result, the wave envelope elements can afford to be several wavelengths long and the dimensionality of the problem reduces dramatically.

The modified shape function of node j in a wave envelope element is

$$N_j' = N_j \frac{R_j}{R} e^{-i\eta_r(\psi - \psi_j)} \tag{19}$$

where,

$$R = \sqrt{x^2 + \beta^2 r^2} \tag{20}$$

and

$$\psi = \frac{-Mx + R}{\beta^2} \tag{21}$$

as shown earlier. Here N_j is the standard shape function corresponding to the jth node. The modified shape function of the wave envelope element assumes a value of unity at its corresponding node and zero at all other nodes, thereby preserving the fundamental property of basis functions. Since the wave envelope elements represent the field generated by a simple source in uniform flow, it is expected that the elements will be bounded by lines of constant phase and acoustic ray paths from the origin as shown in Figure 3.
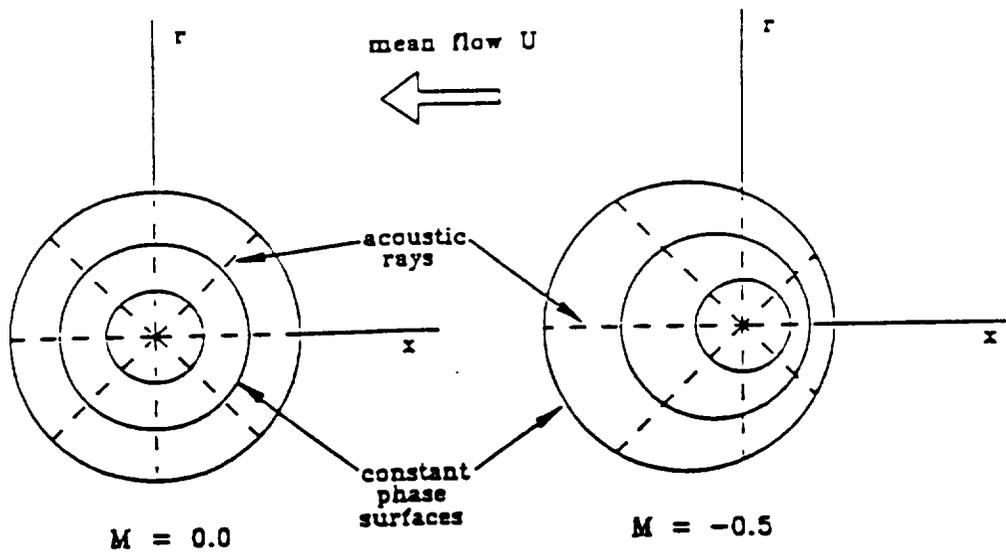
Figure 2: Constant phase circles in uniform flow
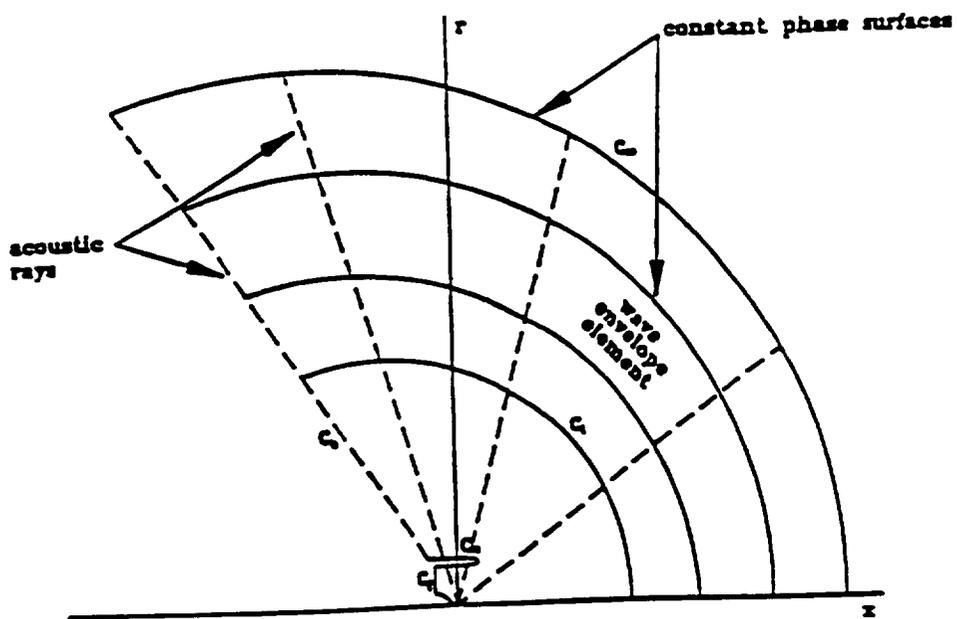
Figure 3: Geometry of a wave envelope element

III. MESH GENERATION SCHEME

This section discusses the generation of the finite element mesh which plays a vital role in the formulation of the problem. Both eight-node and nine-node quadratic isoparametric elements have been used for the analysis. The mesh generation scheme is more or less the same for both the elements, only the connectivity and certain other minor parameters need to be altered. Figure 4 shows an eight and a nine-node parent element with the local numbering of their nodes. For the convenience of constructing the mesh, the entire computational domain has been divided into three regions. Figure 5 illustrates the three regions clearly. Region I occupies the interior of the nacelle, region II extends from outside the inlet to the boundary C_1 and region III (the wave envelope region) extends from C_1 to the outer boundary C_∞.

A. REGION I

Due to the complex nature of the acoustic field inside the nacelle, a fine mesh is generated in order to resolve the variation in acoustic properties. It is separated from region II by a circle which we shall call the highlight circle. The highlight circle is drawn from the nacelle tip (also known as the highlight) in such a way that its center lies at the point of intersection of the x-axis and a line passing through the tip of the nacelle at $45°$ with the x-axis (see Figure 6).

The inner surface of the nacelle C_n extends from the fan face to the tip of the nacelle. The centerline of the inlet geometry extends from the intersection of the centerbody curve with the x-axis and the intersection of the highlight circle with the x-axis. Three-node quadratic line elements lie along the inner surface of the nacelle, the centerbody and the centerline. The coordinates of these nodes are given as input to generate the mesh in region I. The number of input nodes on
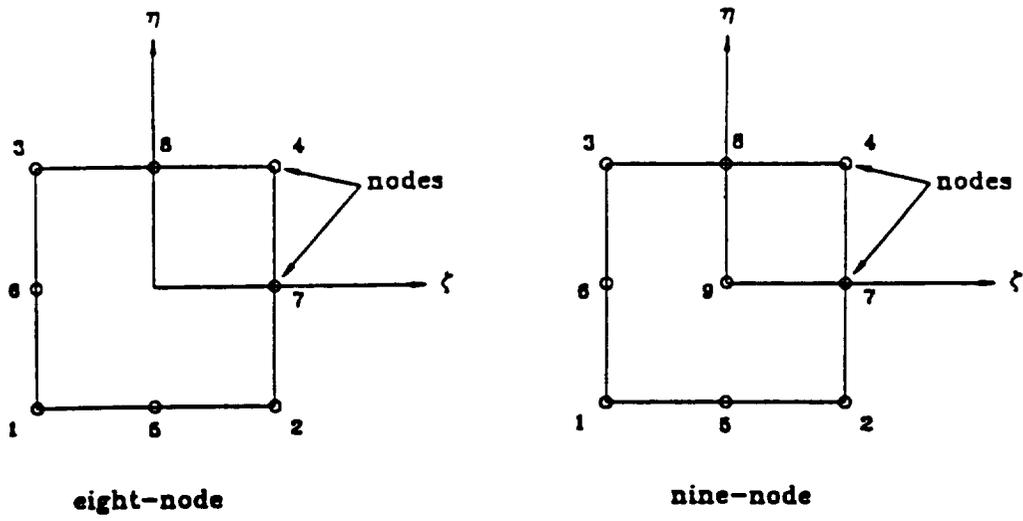
Figure 4: Parent element in local coordinates
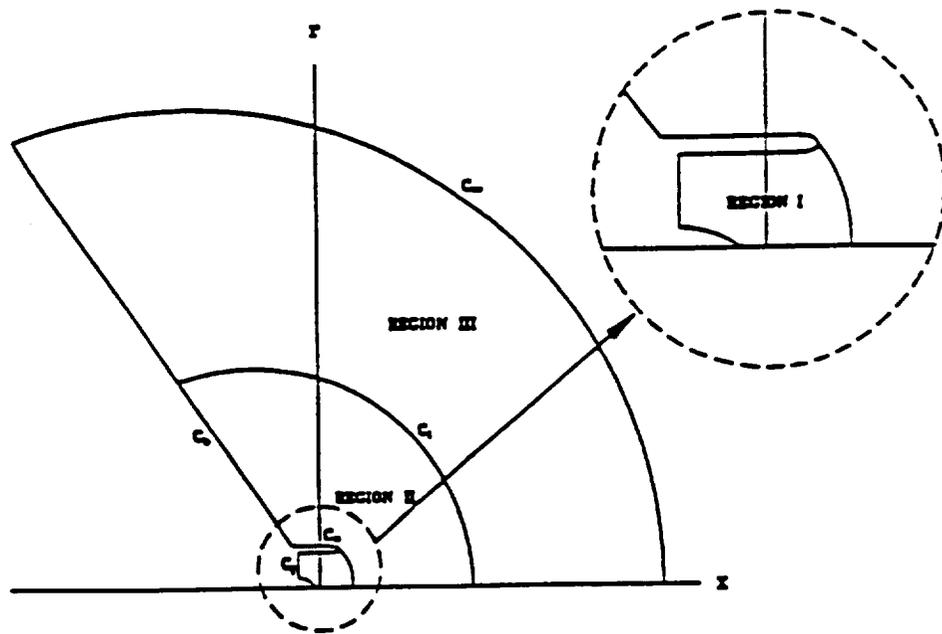
Figure 5: Mesh generation regions

19
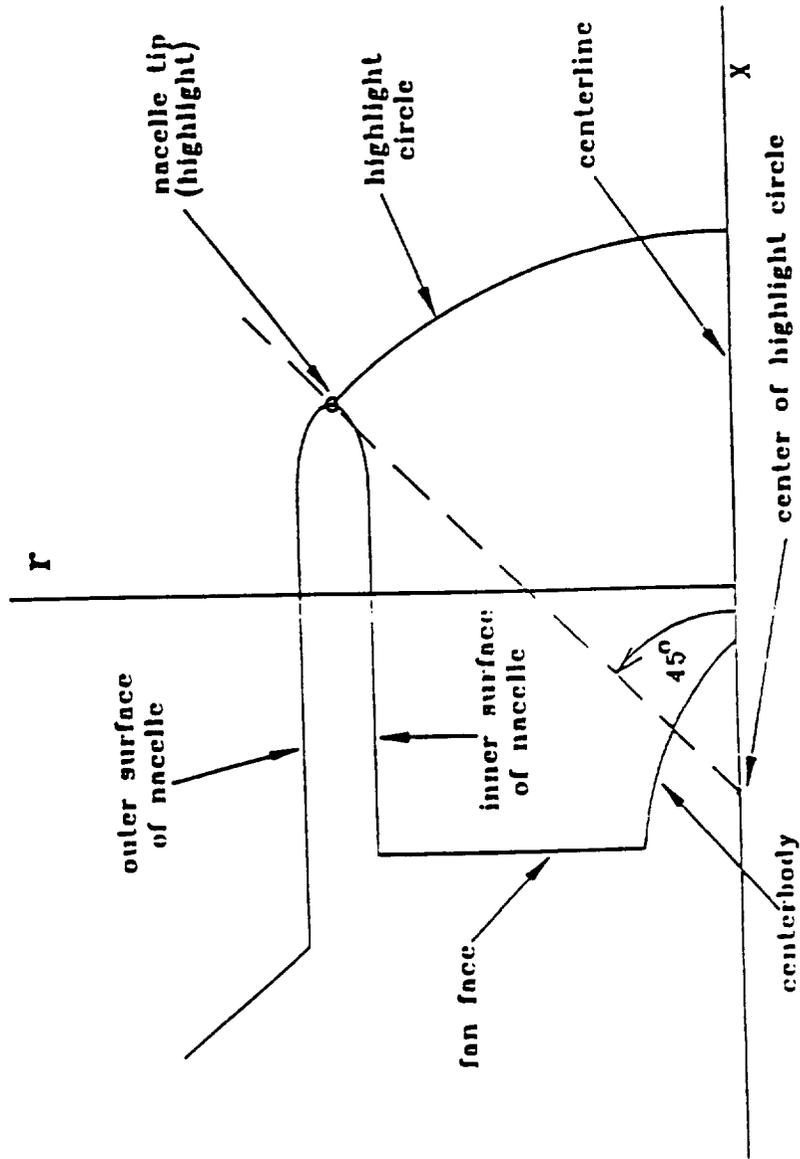
Figure 6: Geometry of region I

20

the inner surface of the nacelle and on the centerbody and centerline is the same, to produce a mesh of generally rectangular elements.

The input data file for the mesh generation program is prepared by a cubic spline interpolation routine. The configuration for each of these curves in the inlet geometry (i.e. inner surface of the nacelle, centerbody and centerline) is fed into the interpolation program in the form of discrete data points. The program then fits a smooth curve through these data points to represent that curve by solving a tridiagonal system of equations. Convenient nodal points are then chosen on the interpolated curve at any desired fraction of the total length. The node points on the centerbody and centerline are generated first. These are followed by the node points on the inner surface of the nacelle which are at the same fractional distance from the fan face (fraction based on the curve length) as their corresponding node points on the centerbody and centerline. This has been done to prevent distortion in the mesh.

The fan face has also been divided into several elements not necessarily of equal width, each to be represented by a three-node quadratic line element. Figure 7 illustrates the meshing scheme in this region. The "vertical" element boundaries inside the nacelle are formed by arcs of circles. These arcs are drawn through corresponding nodal points on the upper and lower boundaries (for example, the fifth node on the nacelle inner surface and on the centerbody and centerline, counted from the fan face) with the center of the circles lying on the x-axis. Such circles are easily constructed as illustrated by Figure 8. (x_1, y_1) and (x_2, y_2) are coordinates of any two corresponding nodal points on the nacelle inner surface and the centerbody and centerline respectively. Then the x-coordinate of the center of a circle passing through these two points and having its center on the x-axis is

21
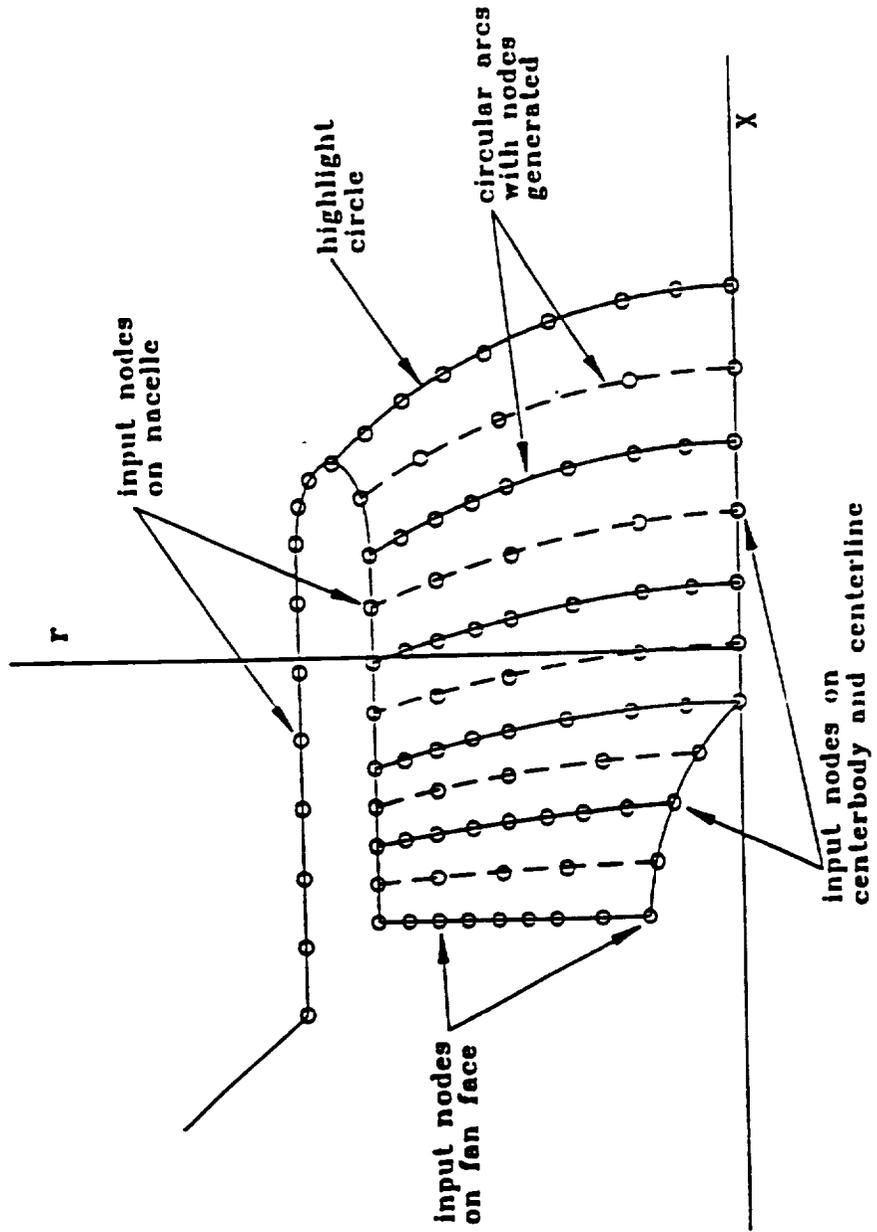
Figure 7: Node generation in region I

highlight circle

input nodes on nacelle

circular arcs with nodes generated

input nodes on centerbody and centerline

input nodes on fan face

r

X

the x-axis is given by

$$x_c = \frac{(x_2^2 - x_1^2 + y_2^2 - y_1^2)}{2(x_2 - x_1)} \qquad (22)$$
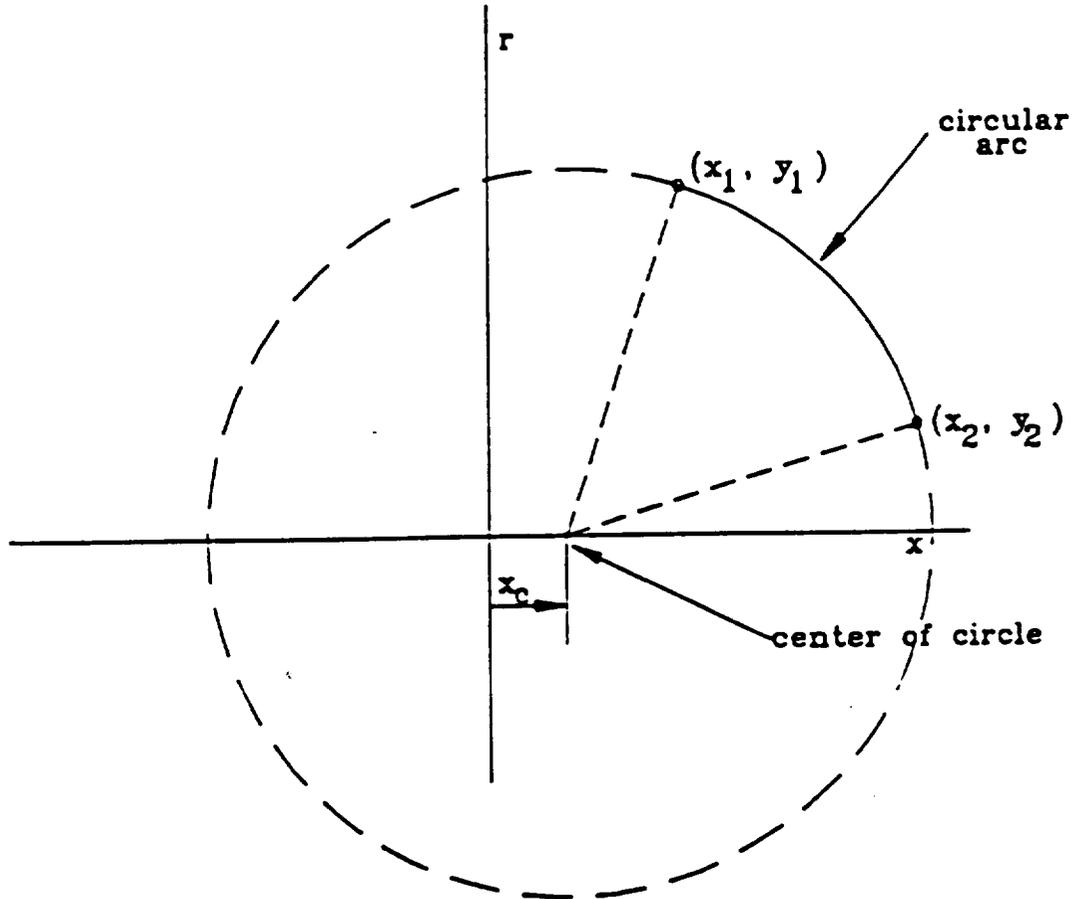
Figure 8: Geometry of a circular arc in region I

Now, to preserve the rectangular mesh, each of these circular arcs should have the same number of three noded line elements on them and this should equal the number of three noded line elements on the fan face. Therefore, each of these arcs is divided into the same number of elements with the same fractional length (fraction based on the arc length) as on the fan face. Thus, the nodal

23

elements on each of these circular arcs is determined. The nodal coordinates are stored in a topology array $AD(I, J, K)$ where I is the global element number, J is the local node number and $K = 1$ assigns the x coordinate, $K = 2$ the r coordinate, respectively, to the array. Proper connectivity relating the local node to its global numbering is also generated and stored in a connectivity array $AN(I, J)$, where $I =$ element number, $J =$ local node number. This array stores the global node number for each node.

The global node numbering goes from top to bottom of each of the circular arcs (see Figure 9) starting from fan face onwards. The element numbering is also down each column of elements between adjacent circular arcs and sequenced from fan face onwards (see Figure 9).

B. REGION II

The mesh in region II becomes polar in nature essentially because of the configuration of the domain outside the inlet duct. Region II is separated from the wave envelope region III by a constant phase circle, as described previously, whose x-intercept is given as input. The constant phase circles are expanding radially with the local speed of sound (c) and their centers are moving away along the x-axis with the speed of uniform exterior flow (U) (see Figure 10). This phenomenon is very similar to the successive circles of outward ripples created on the surface of still water when a pebble is thrown into it. The only difference is that in still water the centers of the successive layers of outward moving circular ripples coincide and here the centers of the constant phase circles move at a constant velocity.

From Figure 10, we obtain the equation of a constant phase circle (of radius R_c) displaced along the positive x-axis with velocity U (positive direction of U is

24

indicated in Figure 10)

$$(x - Ut)^2 + r^2 = R_c^2 \qquad (23)$$

where $R_c = ct$ is the radius of the circle Therefore,

$$(x - U\frac{R_c}{c})^2 + r^2 = R_c^2 \qquad (24)$$

or,

$$(x - MR_c)^2 + r^2 = R_c^2 \qquad (25)$$

where M is the Mach number of the uniform exterior flow[3]. By setting $r = 0$ in equation (25) we obtain the x-intercept of the circle

$$\bar{x} = (M \pm 1)R_c \qquad (26)$$

The positive sign corresponds to the x-intercept on the positive x-axis,

$$\bar{x} = (1 + M)R_c$$

while the negative x-axis corresponds to the x-intercept on the negative x-axis,

$$\bar{x} = -(1 - M)R_c$$

The circles can be expressed in polar coordinates R and θ by,

$$(R cos\theta - MR_c)^2 + (R sin\theta)^2 = R_c^2 \qquad (27)$$

Solving for R in terms of θ yields,

$$R = R_c[\sqrt{1 - M^2 + (M cos\theta)^2} - M cos\theta] \qquad (28)$$

Hence, the radial distance R at every angular position θ on the outer boundary of region II is known.

---

[3] Equation 25 is similar to equation 18 in Section II.
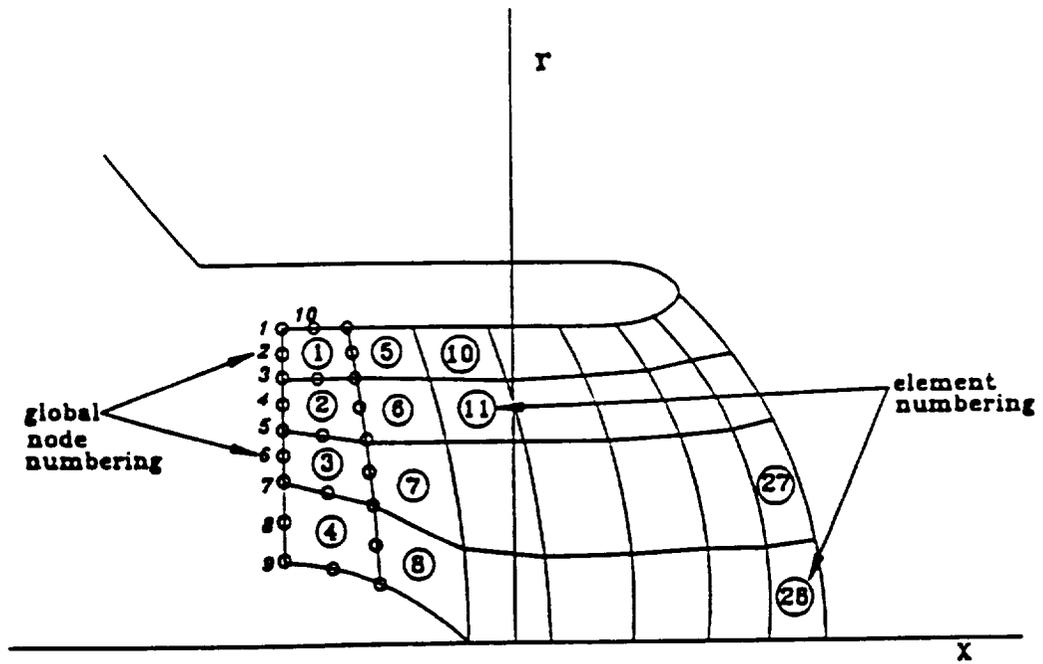
Figure 9: Element and node numbering in region I

U is positive in this direction
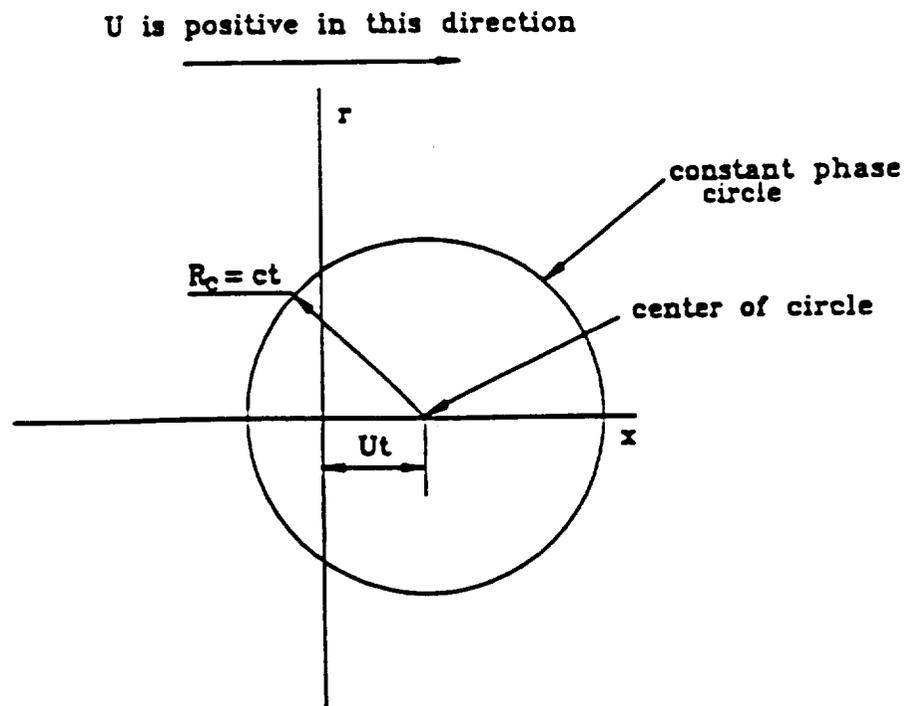
Figure 10: Geometry of a constant phase circle in uniform flow

The outer surface of the nacelle (portion of the nacelle surface C_n starting from the baffle C_b to the highlight) which forms a part of the inner boundary of region II has three-node quadratic line elements along it. The input data preparation for this region is the same as in region I. The configuration of the curve representing the outer surface of the nacelle is fed into the cubic interpolation routine in the form of discrete data points. The program then fits a smooth curve through them. Suitable nodal points are then selected at any arbitrary distance along the curve. Since the mesh generation in region I precedes that in this region, the coordinates of the three-node line elements lying along the highlight circle arc are known. The nodal points on the outer surface of the nacelle and on the highlight circle arc serve as input for the mesh generation in region II (see Figure 11).

In this region and also in the subsequent region III, the nodes have been generated on and along the acoustic rays from origin. Since the mesh is polar, the angular thickness of the elements increases with radial distance because the acoustic rays are radial lines diverging from the origin. To maintain proper aspect ratio of the elements in this region, the radial thickness of the elements should also increase accordingly along acoustic rays moving away from the origin. Now, corresponding to each nodal point on the outer nacelle surface and highlight circle arc, an acoustic ray is defined and its point of intersection with the outer bounding circle of region II is calculated (see Figure 11). Therefore, the radial distance along that ray in region II is known. This radial distance is then divided according to the number of elements required along the general direction of noise propagation, in geometric progression, from the inner boundary to the boundary C_1. From elementary mathematics, we know that if $r_1, r_2, \ldots, r_n$ are n members of a series in geometric progression, then the members are related to each other in the following

outer radius of
wave envelope layer

mean radius of
wave envelope layer

inner radius of
wave envelope layer

acoustic
rays

C_1

r

x

points of
intersection
of acoustic rays
with constant
phase circles

input nodes for region II
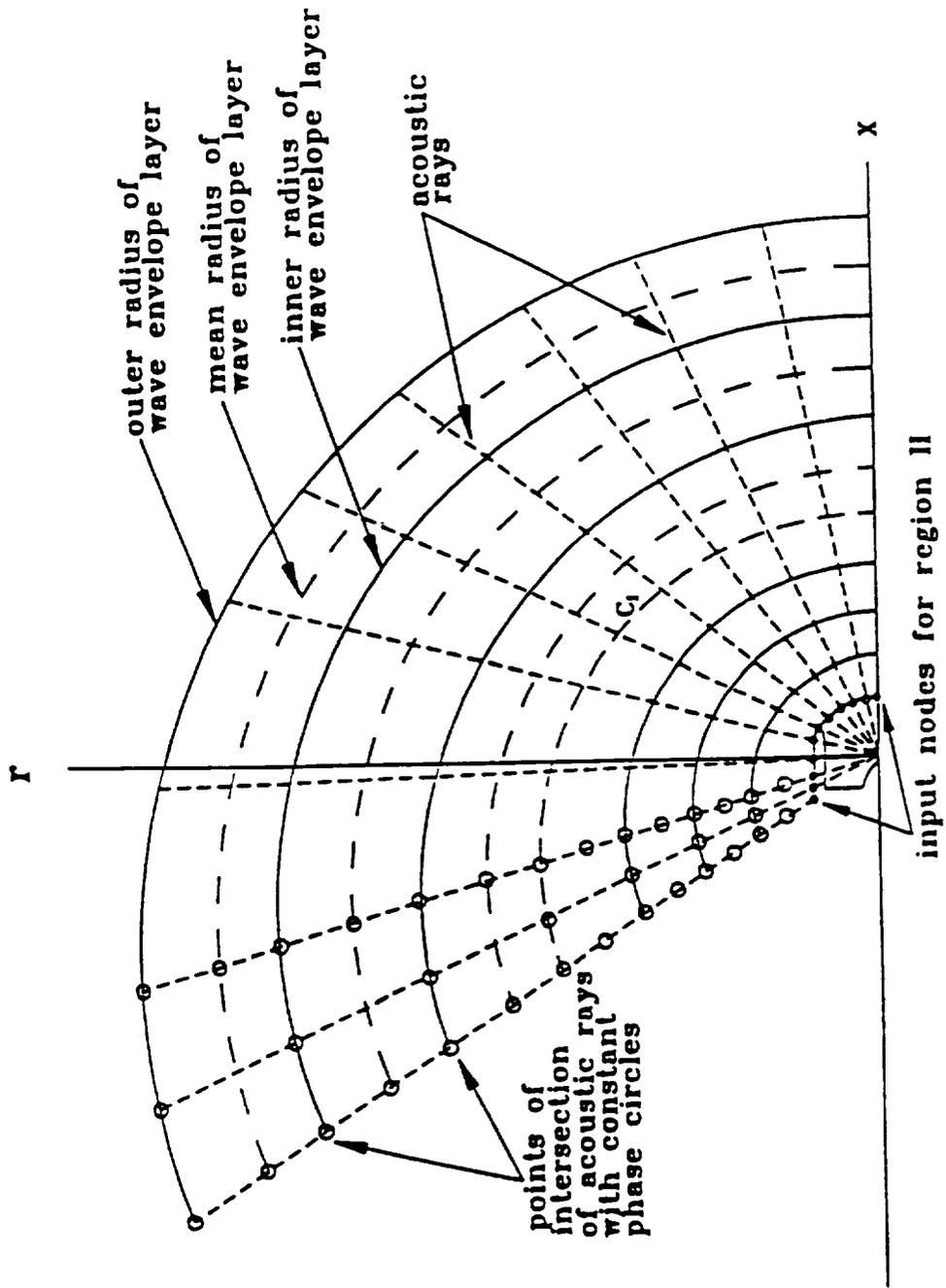
Figure 11: Node generation in regions II and III

way,

$$\left.\begin{array}{rcl} r_2 & = & cr_1 \\ r_3 & = & cr_2 \\ \vdots & \vdots & \vdots \\ r_n & = & cr_{n-1} \end{array}\right\} \tag{29}$$

where c is the *common ratio* of increment. So, the last member is related to the first member by

$$r_n = c^{n-1} r_1 \tag{30}$$

Referring to Figure 12 where an acoustic ray intersects with the two boundaries of region II, it is obvious that the first and the last members of the geometric progression series, i.e. intersection points on the inner boundary and the outer bounding circle C_1 respectively, are known. Since the number of elements n in the radial direction of region II is an input, the common ratio of geometric progression is found out using equation (30),

$$common\ ratio = \left(\frac{\text{outer bounding circle}}{\text{inner bounding circle}}\right)^{\frac{1}{n}}$$

Once the *common ratio* is known, the successive intervals are found out by multiplication with the *common ratio* as in equations (29). Hence, the nodal points of the line elements along that acoustic ray are located. Geometric progression provides a gradual increment in the radial thicknesses of elements which is sufficient to a maintain proper aspect ratio.

The nodal coordinate values are stored in rectangular cartesian form in a topology array $AD(I, J, K)$ as mentioned before. The connectivity array $AN(I, J)$ is also created. As illustrated in Figure 13, the element numbering in this region, continues after region I and goes down each column of elements running from the baffle surface to the x-axis. The global node numbering also goes down each side of the element columns sequenced from the inner boundary consisting of the upper surface of the nacelle and highlight circle arc.

29
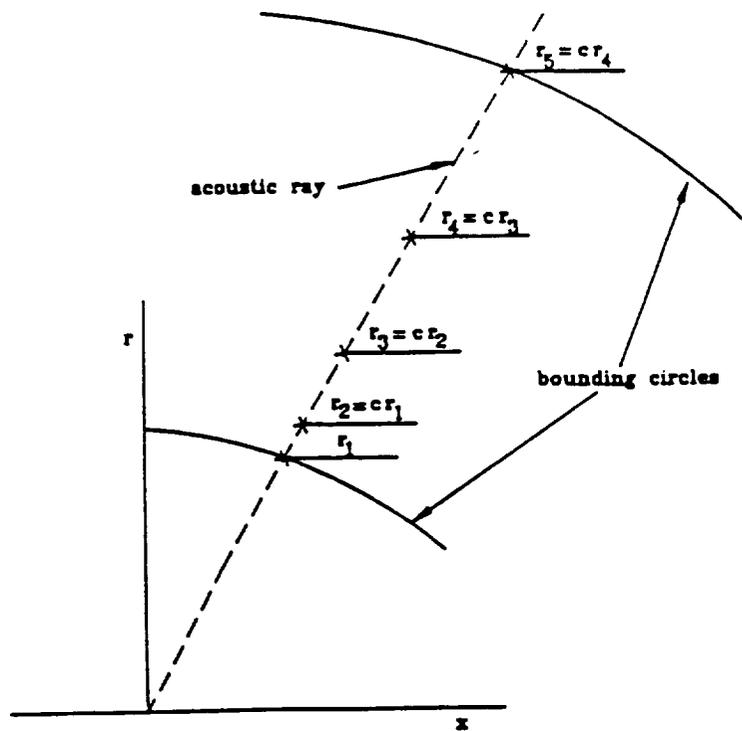
Figure 12: Geometric progression in region II
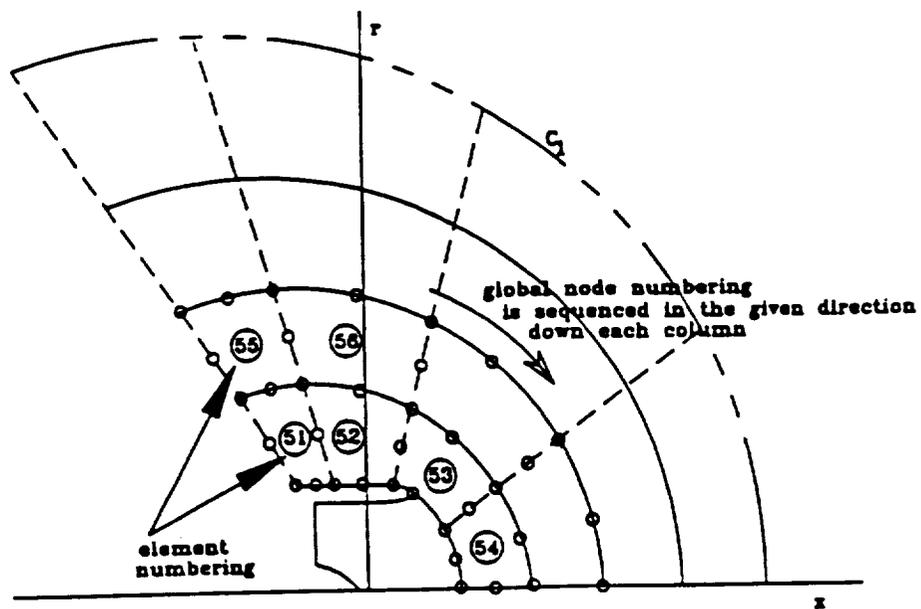
Figure 13: Element and node numbering in region II

30

C. REGION III

Region III which consists entirely of wave envelope elements is bounded by the transition boundary C_1, the outer boundary C_∞, the baffle C_b and the x-axis. The wave envelope elements, as discussed before, are large elements bounded by acoustic rays and constant phase circles. The string of elements between any two successive constant phase circles is referred to as a wave envelope layer. The input for mesh generation in this region is the number of wave envelope layers and the x-intercept of the constant phase circles bounding each layer. Using equations (26) and (28), the inner and outer radii of the constant phase circles bounding each such layer is determined. The mean radius of each layer, which is just the average of the inner and outer radii, is also calculated. Since the mesh generation in region II is complete at this stage, the three-node line elements (note that a three-node line element forms a side of an eight or nine-node isoparametric element) on the outer bounding circle C_1 of region II have been located completely and their global numbering is also known. Therefore, corresponding to each nodal point on C_1, an acoustic ray is defined (see Figure 11) and thereby its points of intersection with the inner, mean and outer radii of each wave envelope layer are calculated. The rectangular cartesian coordinate values of these intersection points on which the nodes lie are stored in the topology array $AD(I, J, K)$. The connectivity array $AN(I, J)$ is similarly calculated as in region II. The element and the global node numbering follows after region II and is similar to region II. Since the mesh in region II is quite fine and that in region III is coarse, care should be taken to make a gradual transition in the size of the elements.

After the mesh is generated, a connectivity check is performed to ensure a proper connection between local and global numbering of nodes and uniqueness of nodal coordinate values.

31

D. IDENTIFICATION OF THE BOUNDARY ELEMENTS

Identification of the boundary elements is necessary for proper imposition of boundary conditions in the finite element calculations. After the mesh is constructed in the whole domain, the topology (i.e. nodal coordinate) array and the nodal connectivity array for the line elements on each of the boundaries of the domain are calculated separately. An element identification array $NETYPE$ is set up and different values are assigned to it for different boundary elements for identification purposes.

The setting up of topology and nodal coordinate arrays for each boundary surface is accomplished in several subroutines. The nodal connectivity array for a boundary is $ANL(I,J)$, where I = element number from 1 to the number of line elements along that boundary, and J = the local node number in a quadratic line element. This array defines the global node number of the corresponding node on that boundary. The topology array is $ADL(I,J,K)$, where I and J are the same as above and $K = 1$ defines the global x-coordinate value of the node, whereas $K = 2$ defines the r-coordinate value of the node.

An input and output data description for the mesh generation program has been described in the appendix.

E. SOME COMMENTS ABOUT THE FINITE ELEMENT MESH

The acoustic radiation problem is highly mesh dependent but the mean flow problem is not very sensitive to the mesh parameters. Since both of these problems have been solved on the same finite element mesh, a mesh conforming to the acoustic parameters is desired. One of the important factors governing the mesh is the number of elements per wavelength which must always be maintained above

a minimum value in the main direction of noise propagation to resolve the fine variation in acoustic properties. According to the rule of thumb the minimum ratio of the number of elements to the wavelength for quadratic elements should be 4 or 5. Here a somewhat crude estimate has been made to evaluate that ratio along the main direction of sound propagation.

Since the nondimensional input frequency η_r (it is an input to the problem) of the sound source on C_f is known, we obtain a ratio of the effective wavelength λ_e (the wavelength of the sound radiated is altered in the presence of mean flow) to the reference duct radius R in the following way :

$$\eta_r = \frac{\omega R}{c} = \frac{2\pi R}{\lambda}$$

since

$$\lambda_e = (1 - M)\lambda$$

therefore,

$$\eta_r = \frac{2\pi R}{\lambda_e}(1 - M)$$

or,

$$\frac{\lambda_e}{R} = \frac{2\pi}{\eta_r}(1 - M) \tag{31}$$

The Mach number M is positive if directed towards the inlet. Now if the number of elements per duct radius length is N_R and Δ is the average width of an element within that length, then

$$\frac{R}{\Delta} = N_R$$

Therefore, using equation (31), the ratio of the number of elements per unit duct radius can be expressed as

$$N_R = \frac{\eta_r}{2\pi(1 - M)}N_{\lambda_e} \tag{32}$$

where $N_{\lambda_e}(= \lambda_e/\Delta)$ is the number of elements per effective wavelength. For a specified number of elements per effective wavelength (for the elements used here

33

N_{λ_c} is the goal), equation (32) can be used to determine the number of elements per unit of nondimensional length required. This varies as the flow towards the inlet varies, and would generally be highest within the nacelle near the fan face. The number of elements in the transverse direction within the nacelle or in the angular direction in region II is not as critical and is adjusted to maintain the aspect ratio of the elements. Another very important mesh parameter affecting the final solution is the geometric position of the outer bounding circle C_1 (the transition circle) of region II. This is discussed in a later section.

Since the position of the constant phase circles bordering the wave envelope layers are user input, care should be maintained to make a gradual transition from the small conventional finite elements to the relatively large wave envelope elements. For this, the user should be aware of the radial thickness of the last layer of conventional elements along C_1. Since the radial thicknesses of the elements in region II have been incremented in geometric progression, the radial thickness of the last element in region II on the x-axis is

$$\Delta r = (c^n - c^{n-1})r_o$$

where c is the common ratio of increment, n is the number of elements radially in region II and r_o is the x-intercept of C_1. This information is valuable to the user for making a smooth transition from region II to III. An example of a finite element mesh with 3441 elements (52 elements along the x-direction in region I, 40 elements radially in region II and 9 wave envelope layers) and 10624 degrees of freedom is given in Figures 14, 15, and 16, where Figures 15 and 16 show the mesh in regions I and II in detail. The transition circle C_1 starts at a nondimensional distance of 3.5 from the origin. In region I, a very fine mesh has been generated in the x-axis direction due to the complexity of the acoustic field. In the direction of the duct radius the mesh has been made gradually more coarse towards the

centerbody since the region quite close to the x-axis does not usually fall in the main direction of sound propagation. Outside the nacelle, in region II, the mesh is coarser than in region I, but still quite dense in the sector bordered by $30°$ on the lower side and $85°$ on the upper side. This sector usually corresponds to the main direction of sound propagation at moderate frequencies (for example, 15.0) and low angular mode numbers (for example, 10). The mesh shown as an example will be suitable for frequencies upto 15.0. At frequencies higher than 15.0, the mesh must be refined in the radial direction to satisfy the number of elements per wavelength criterion. The wave envelope elements in the region III allow us to have a very coarse mesh in the far field.
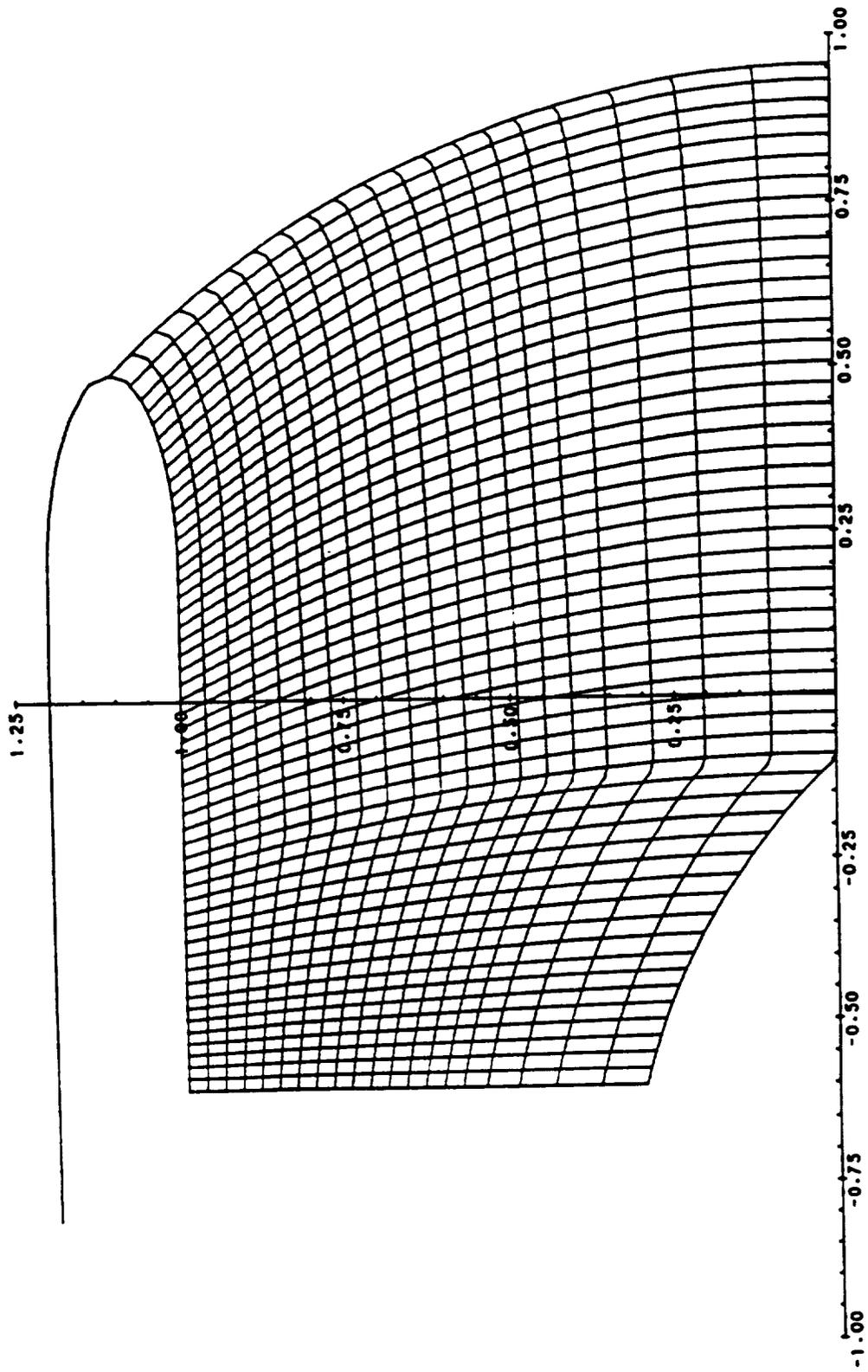
Figure 14: Finite element mesh inside the nacelle
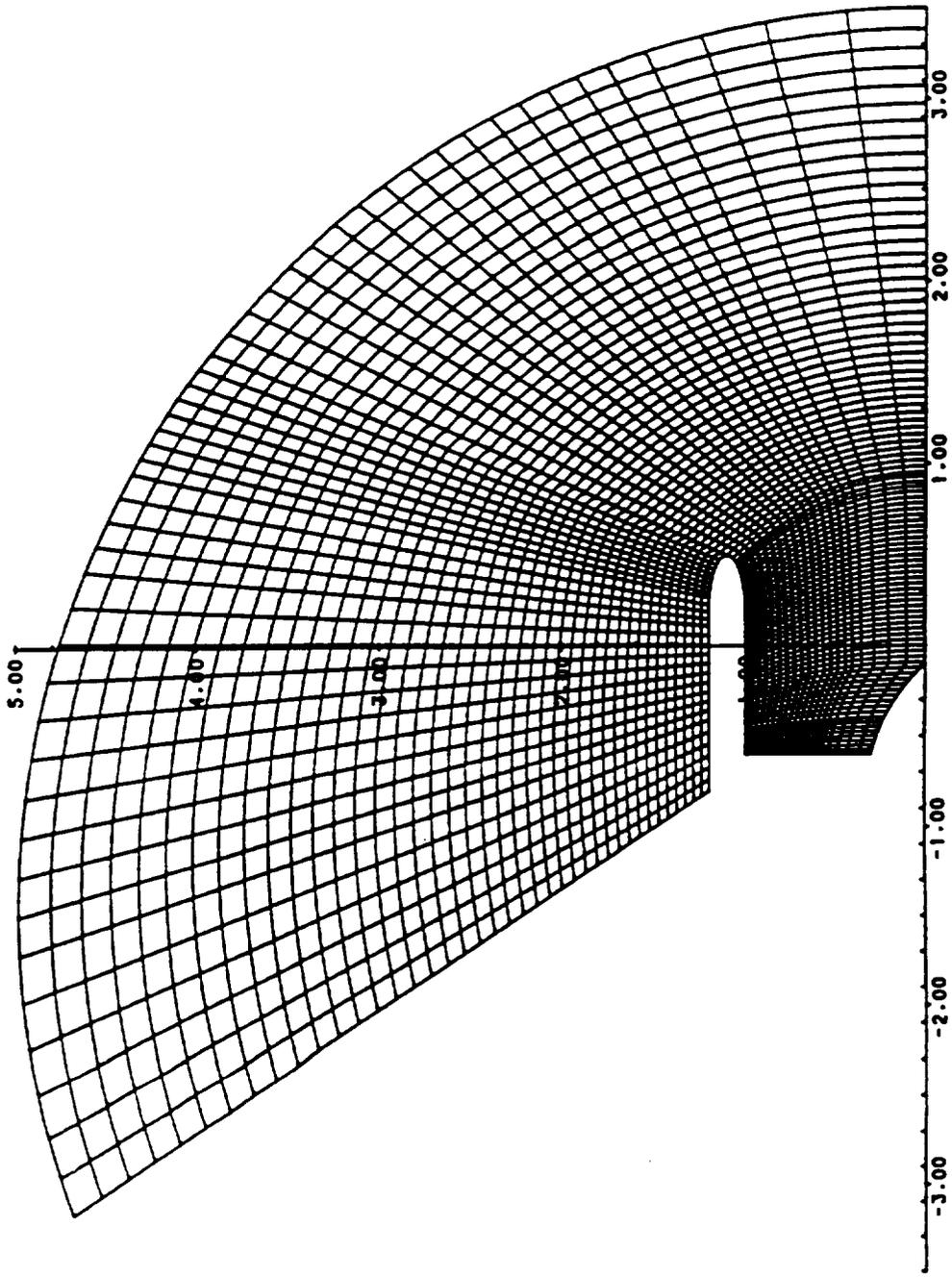
Figure 15: Finite element mesh in regions I and II
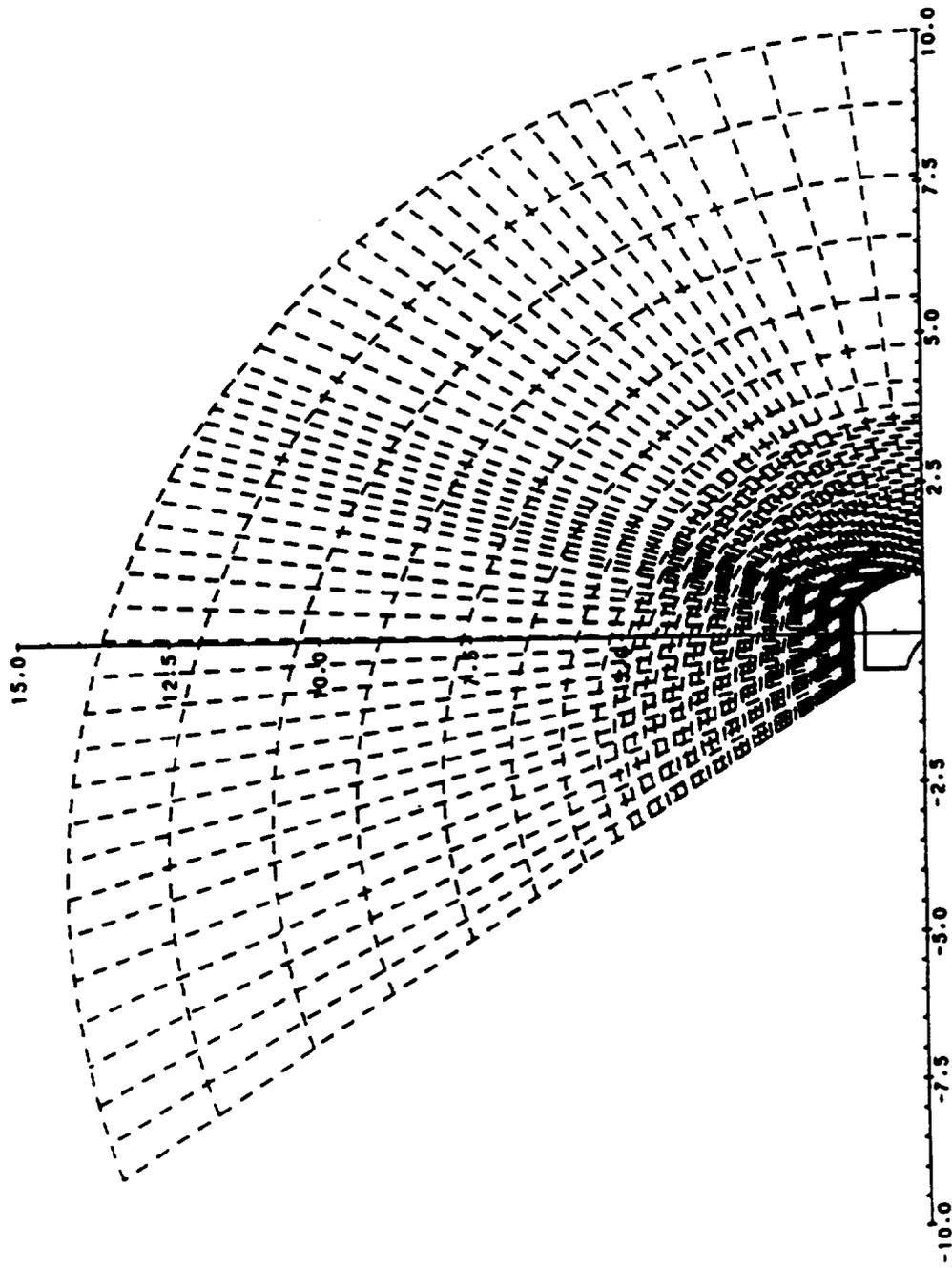
Figure 16: Finite element mesh in the whole domain

IV. UNIFORM DUCT EIGENVALUE PROBLEM

For the radiation problem the eigenvectors representing the acoustic modes in a uniform duct are used to implement boundary conditions at the fan face. They are conveniently calculated when the mesh is generated. The formulation of the eigenvalue/eigenvector problem is discussed in this section.

A. ONE DIMENSIONAL BOUNDARY VALUE PROBLEM

The fan face C_f is taken to be at a locally uniform part of the inlet. To specify the acoustic potential there, a finite element eigenvalue problem has been solved in the inlet duct on the fan face. The eigenvalues and eigenvectors obtained from the problem are used later to evaluate the boundary condition at the fan face for the acoustic radiation problem. The nondimensional acoustic field equation for

circular duct   annular duct
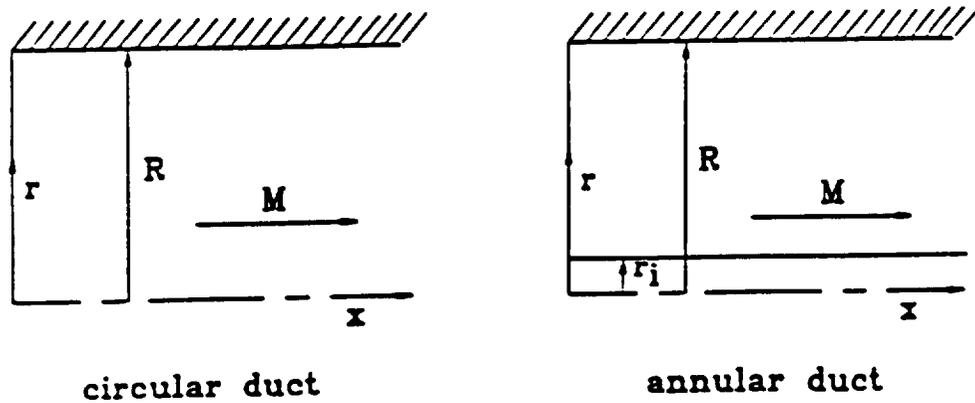
Figure 17: Duct geometry

the axisymmetric duct with uniform mean flow shown in Figure 17 is

$$(\frac{\partial}{\partial t} + M\frac{\partial}{\partial x})^2\phi - \nabla^2\phi = 0 \qquad (33)$$

where M is the local Mach number of the uniform flow. It is assumed that the acoustic potential in the case of a harmonic acoustic source on the surface C_f, with time dependence $e^{i\eta_l t}$, has axial and azimuthal variations of the form

$$\phi = \phi_r(r)e^{i(\eta_l t - m\theta - k_z z)} \qquad (34)$$

where $\eta_l = \omega R/c_l$ is the local nondimensional frequency (c_l is the local speed of sound in the duct), k_z is the axial wave number and m is an integer representing the angular (spinning) mode number[4].

Substitution of equation (34) in (33) yields

$$\frac{d^2\phi_r}{dr^2} + \frac{1}{r}\frac{d\phi_r}{dr} + [\eta_l^2\{(1 - \frac{Mk_z}{\eta_l})^2 - (\frac{k_z}{\eta_l})^2\} - \frac{m^2}{r^2}]\phi_r = 0 \qquad (35)$$

It is important to note that the Mach number M in the above equation (35) is the local Mach number at the fan face.

Define

$$\kappa_m^2 = \eta_l^2[(1 - \frac{Mk_z}{\eta_l})^2 - (\frac{k_z}{\eta_l})^2] \qquad (36)$$

and substitute in equation (35) to obtain Bessel's equation

$$\frac{d^2\phi_r}{dr^2} + \frac{1}{r}\frac{d\phi_r}{dr} + (\kappa_m^2 - \frac{m^2}{r^2})\phi = 0 \qquad (37)$$

Since the duct has hard walls, the boundary condition prescribed at the wall $\nabla\phi \bullet \mathbf{n} = 0$ ($\mathbf{n}$ is the unit outward normal vector on the duct wall) when interpreted in the one dimensional case yields,

• For Circular Duct   A circular duct corresponds to the case with no centerbody.

$$\text{at } r = 0, \quad \phi_r \text{ is finite} \qquad (38a)$$

---

[4]The factor $e^{-im\theta}$ accounts for the spinning acoustical modes generated by steady blade loading or by the interaction between the rotor and the exit guide vanes.

$$at \quad r = R, \quad \frac{d\phi_r}{dr} = 0 \tag{38b}$$

• <u>For Annular Duct</u> An annular duct corresponds to the case with a centerbody.

$$at \quad r = r_i, \quad \frac{d\phi_r}{dr} = 0 \tag{39a}$$

$$at \quad r = R, \quad \frac{d\phi_r}{dr} = 0 \tag{39b}$$

B. FINITE ELEMENT FORMULATION

A standard Galerkin finite element formulation has been used with three-node quadratic Lagrangian elements. A finite element mesh that fits these elements on to the fan face has already been dealt with in the previous section. The differential equation (35) and the boundary conditions (equations (38) and (39)) which compose the boundary value problem for both the circular and the annular duct, are approximated by a weak form of the boundary value problem for both the circular and annular duct.

Let $\psi : \Omega \longrightarrow \mathbf{R}$ be a smooth function where, the domain Ω is $[0, \ r_o]$ for a circular duct and $[r_i, \ r_o]$ for an annular one. Multiplication of the differential equation (35) with the test function ψ and integration over the domain yields

$$\int_\Omega \psi[\frac{d^2\phi_r}{dr^2} + \frac{1}{r}\frac{d\phi_r}{dr} + (\kappa_m^2 - \frac{m^2}{r^2})\phi_r]d\Omega = 0$$

or

$$\int_\Omega \frac{d}{dr}(r\frac{d\phi_r}{dr})\psi dr + \int_\Omega (\kappa_m^2 - \frac{m^2}{r^2})\phi_r\psi r dr = 0 \tag{40}$$

Integration of the first term in equation (40) by parts, yields

$$r\frac{d\phi_r}{dr}\psi\Big|_\Gamma - \int_\Omega \frac{d\phi_r}{dr}\frac{d\psi}{dr}r dr + \int_\Omega (\kappa_m^2 - \frac{m^2}{r^2})\phi_r\psi r dr = 0 \tag{41}$$

where $|_\Gamma$ indicates that the given term is evaluated at the boundary Γ. This term goes is zero for both the circular and annular duct cases.

41

After discarding the boundary term in equation (41) and rearranging the rest, the weak formulation is written as

$$\int_\Omega (\frac{d\phi_r}{dr}\frac{d\psi}{dr} + \frac{m^2}{r^2}\phi_r\psi)r\,dr - \kappa_m^2 \int_\Omega \phi_r\psi r\,dr = 0 \qquad (42)$$

The following weak problem is posed: find a trial function $\phi_r : \Omega \longrightarrow \mathbf{R} \ni$ equation (42) holds $\forall$ smooth $\psi : \Omega \longrightarrow \mathbf{R}$. $\phi_r(r)$ and $\psi(r)$ are suitable classes of functions whose derivatives are square integrable (from H^1 space).

A Galerkin finite element approximation has been used with three-node Lagrangian quadratic elements. Basis functions $N_1, N_2, \ldots, N_n$ are chosen from an n-dimensional subspace of H^1. Hence, the test and trial functions can be finitely approximated as

$$\psi(r) = c_i N_i(r) \qquad (43)$$

$$\phi_r(r) = d_j N_j(r) \qquad (44)$$

where c_i's and d_j's are suitable scalars[5].

Substitution of equations (43) and (44) in (41) yields a finite element matrix formulation of the problem

$$(\underbrace{\int_\Omega \left(\frac{dN_i}{dr}\frac{dN_j}{dr} + \frac{m^2}{r^2}N_iN_j\right) r\,dr}_{K_{ij}} d_j - \kappa_m^2 \underbrace{\int_\Omega N_iN_j r\,dr}_{M_{ij}} d_j = 0 \qquad (45)$$

K_{ij} and M_{ij} are the i, j entries of the stiffness [K] and mass [M] matrices respectively.

Non-trivial solutions of equation (45) for the vector d are found if λ is an eigenvalue of the equation

$$([K] - \lambda[M])\mathbf{d} = 0$$

---

[5] Since ϕ_r is being suitably interpolated between the nodes, the d_j's here represent nodal values of the acoustic potential.

or

$$([M]^{-1}[K] - [I])\mathbf{d} = 0 \tag{46}$$

Here $\lambda = \kappa_m^2$ is the transverse eigenvalue for the mth radial mode, $[I]$ is the identity matrix and $\mathbf{d}$ is the vector of nodal values of the acoustic potential.

The calculations of the global stiffness and the mass matrix are carried out at the elemental level and assembly is accomplished using proper connectivity of the nodes since,

$$[K] = \sum^{n_e}[K]^e$$

$$[M] = \sum^{n_e}[M]^e$$

where n_e is the number of elements in the domain. The element stiffness matrix $[K]^e$ and element mass matrix $[M]^e$ are given by

$$K_{ij}^e = \int_{\Omega_e} (\frac{dN_i^e}{dr}\frac{dN_j^e}{dr} + \frac{m^2}{r^2}N_i^e N_j^e) r\, dr$$

$$M_{ij}^e = \int_{\Omega_e} N_i^e N_j^e r\, dr$$

where $\int_{\Omega_e}$ is the integral over the element and N_i^e is the shape function of the ith node of an element.

The matrix eigenvalue problem (equation (46)) is then solved using a QR solver. Since the problem is of first order, all of the transverse eigenvalues λ are real. It is interesting to note that the eigenproblem could have been posed with the eigenvalue defined as (k_z/η_l). The resultant system would have been of second order and twice as large as the present one.

The exact analytical solutions to the differential equation (35) are transcendental functions called *Bessel functions of the first kind* $J_m(\kappa_m r)$ and *Bessel functions of the second kind* $Y_m(\kappa_m r)$ of order m,

$$\phi_r(r) = AJ_m(\kappa_m r) + BY_m(\kappa_m r) \tag{47}$$

43

Bessel functions are oscillating functions whose amplitudes diminish as $\kappa_m r$ increases, and the $Y_m(\kappa_m r)$ become unbounded in the limit as $\kappa_m r \to 0$. Therefore for the circular duct $B = 0$ and for the annular one both the constants A and B are evaluated by boundary conditions. Application of the boundary conditions on equation (47) evaluates the transverse eigenvalues κ_m from

$$J'_m(\kappa_m r) = 0 \tag{48}$$

for a circular duct, and

$$J'_m(\kappa_m r) + CY'_m(\kappa_m r) = 0 \tag{49}$$

for an annular duct for the mth radial mode.

C. FORMATION OF MODAL MATRIX

In classical duct acoustics, it is shown that duct modes can be categorized as propagating (cut on) or non-propagating (cut-off). Roughly speaking, lower order modes propagate and higher order modes are cut-off. Cut-off modes are those which carry no acoustic power and are therefore entirely reactive with energy trapped near the source.

Rearrangement of the terms in equation (36) yields the axial wavenumber k_z explicitly in terms of the frequency η_l and the transverse eigenvalue κ_m

$$k_z^{\pm} = \eta_l \left[\frac{-M \pm \sqrt{1 - (1 - M^2)(\frac{\kappa_m}{\eta_l})^2}}{1 - M^2} \right] \tag{50}$$

From equation (50), it is apparent that corresponding to each value of the transverse eigenvalue κ_m, there are two distinct values of the axial wavenumber k_z, one representing a positive[6] (or incident) mode and the other representing a negative

---

[6] A positive mode is a one which propagates or decays in the positive z-direction.

(or reflected) mode. The value of the discriminant in equation (50) determines whether the mode is propagating or cut-off. When the discriminant is greater than zero, the mode is cut-on. Since the axial variation of the acoustic potential has been assumed to be of the form $e^{-ik_z z}$, a positive sign in front of the discriminant indicates a positive propagating mode, whereas a negative sign indicates a mode propagating in the opposite direction. When the discriminant is less than zero, it becomes imaginary and the mode is cut-off. The axial wave number for such a mode becomes

$$k_z^{\pm} = \eta_l \left[\frac{-M \pm i\sqrt{(1 - M^2)(\frac{\kappa_m}{\eta_l})^2 - 1}}{1 - M^2} \right] \qquad (51)$$

From equation (34) it can be argued that the amplitude of a wave which is cut-off varies along the x-axis as $e^{\pm \beta z}$ where β is

$$\beta = \eta_l \left[\frac{\sqrt{(1 - M^2)(\frac{\kappa_m}{\eta_l})^2 - 1}}{1 - M^2} \right] \qquad (52)$$

Since the amplitude should decay with distance from the source, a negative sign in front of the discriminant in equation (51) indicates a positive cut-off mode whereas a positive sign indicates a negative cut-off mode.

The positive and negative duct modes, corresponding to a single transverse eigenvalue κ_m have the same mode shape (i.e. eigenvector). Since the higher order modes are increasingly cut-off, and do not contribute much to the acoustic propagation, the first few positive and negative modes have been retained in the modal matrix. The modal matrix is an NDOF $\times$ (NPOS + NNEG) matrix where NPOS is the number of positive modes retained, NNEG is the number of negative modes retained and NDOF is the number of degrees of freedom in the system. Each column in the modal matrix corresponds to a mode. All the retained positive modes have been placed first ordered according to the increasing magnitude of the eigenvalue followed by the columns which represent negative modes in increasing order. Figures 18 and 19 show the first five acoustic duct modes of an annular

45

duct corresponding to angular mode numbers 10 and 20, respectively. Each mode shape is a finite element approximation of a combination of Bessel functions of the first and second kind as given by equation (47). Note that for a duct with no acoustic lining, the positive and negative propagating mode shapes are the same. The transverse eigenvalues and the modal matrix resulting from the calculations are used to impose the boundary condition on the fan face in the acoustic radiation problem. Details of the imposition of the boundary condition are described in a later section.

The above eigenproblem calculations have been done in the mesh generation code because the finite element mesh for the problem is generated along with the mesh for the whole domain. An input and output data description for it has been elaborated in the appendix.
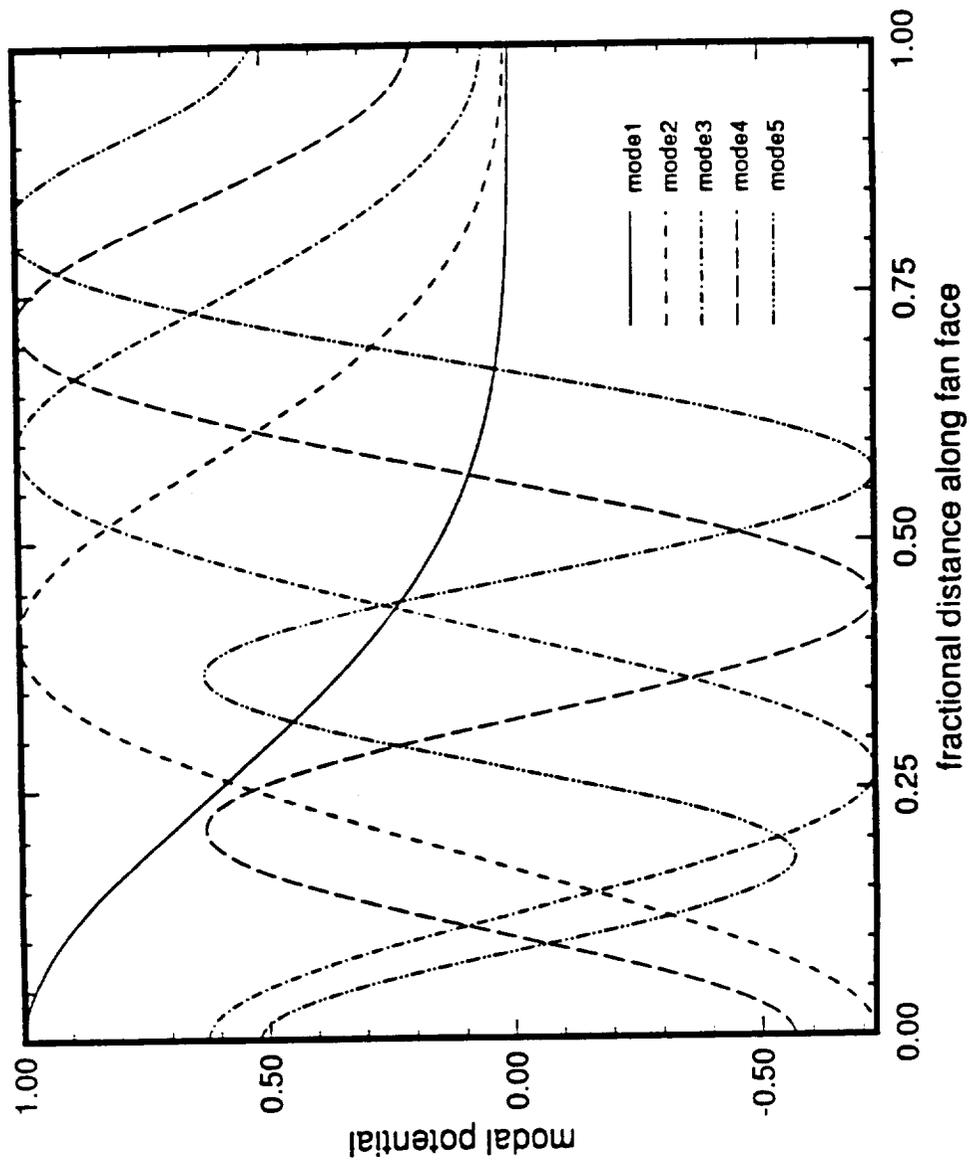
Figure 18: First five annular duct modes; angular mode number $m = 10$
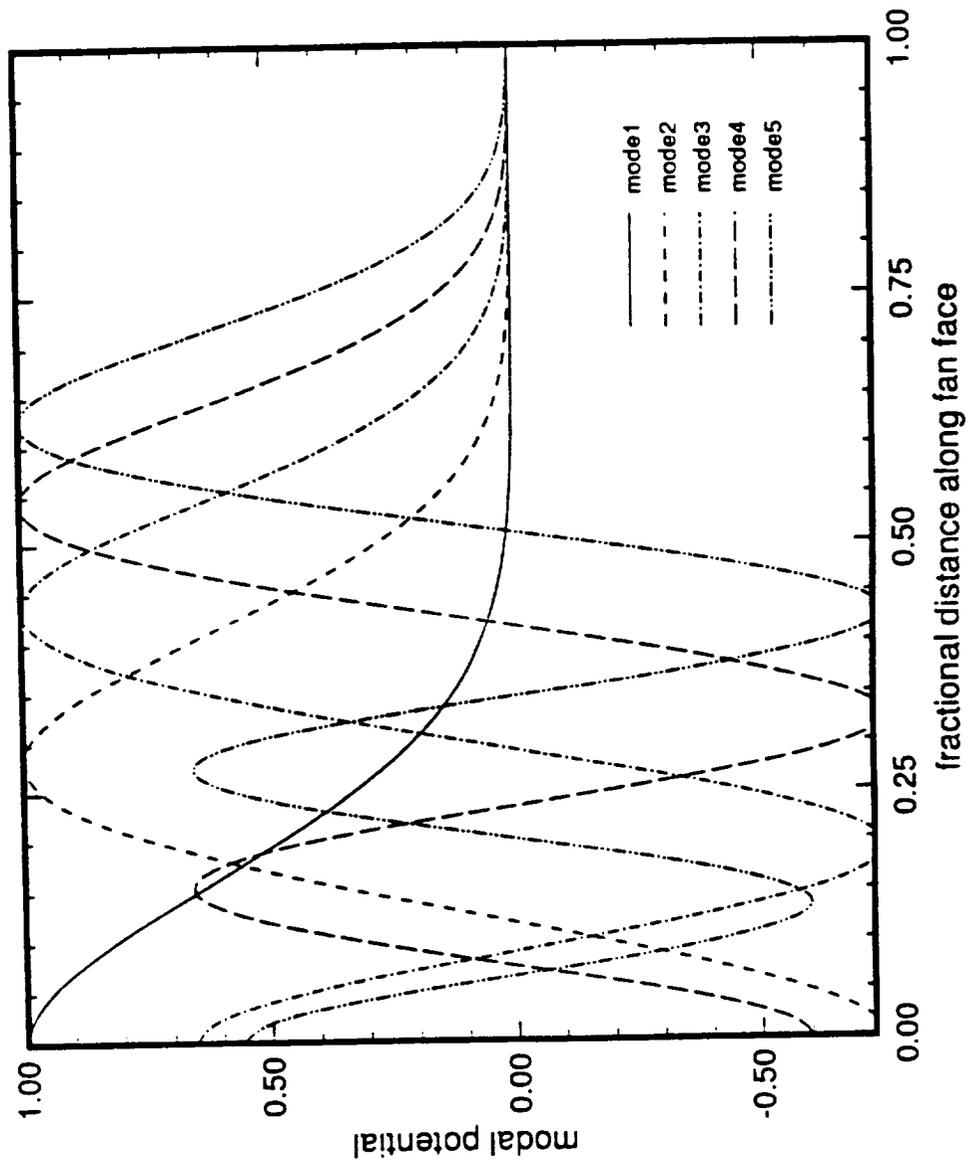
Figure 19: First five annular duct modes; angular mode number $m = 20$

48

V. TIME INVARIANT MEAN FLOW PROBLEM

A. DERIVATION OF THE FLOW PROBLEMS

Equation (14) describes the steady mean flow around the inlet of the turbofan engine. In the general case the fluid is compressible and equation (14) is nonlinear. However, under the assumption of sufficiently low flow Mach number, the flow can be approximated as an incompressible one, and equation (14) can be approximated by

$$\nabla^2 \phi_o = 0 \tag{53}$$

which is the Laplace equation. The assumption of incompressibility does not impose any extra restrictions on the acoustic perturbation flow equation (15) of Section II.D.

In Figure 1, the curves Γ in the x-r plane correspond to surfaces in the axisymmetric space around the inlet. The axis of symmetry Γ_a is not a physical boundary of the domain. In the axisymmetric integral formulation of the problem, the boundary integral corresponding to this axis ($r = 0$) vanishes. Therefore, no boundary condition needs to be specified. The far field boundary Γ_∞ is circular (spherical in axisymmetric space). Though it is several duct radii from the inlet, the flow effects due to the presence of the inlet cannot be assumed negligible. The boundary condition on this curve will be discussed later. The nacelle Γ_n and centerbody Γ_c are impervious to flow. The curve Γ_f represents the fan face. The curve Γ_b representing the baffle is a pseudoboundary that does not exist physically and corresponds to a porous baffle that admits flow through but affects the acoustic field to as small an extent as possible.

Since the differential equation (53) is linear, it can be split up into three different problems, each of which can be solved separately and upon employing

the method of superposition, the velocity potential of the actual flow field can be determined. The velocity potential for the mean flow is decomposed as follows:

$$\phi_o = \phi_u + \phi_p \qquad (54)$$

where ϕ_u is the flow field due to the external uniform flow field only (without the presence of the inlet) and ϕ_p is the flow perturbation due to the presence of the inlet only. The boundary condition to be applied at the boundaries Γ_b and Γ_∞ is not clear until and unless we formulate the problem in terms of flow perturbation. Our aim is to formulate the entire problem in such a way that the fan face and the external flow velocity do not become dependent on the perturbations; rather they govern it.

The perturbation velocity potential ϕ_p is further decomposed into

$$\phi_p = \phi_1 + \phi_2 \qquad (55)$$

where ϕ_1 is the perturbation potential due to inlet flow alone (fan flow effects only) and ϕ_2 is the perturbation potential due to flow to a blank inlet (effect of the presence of the jet engine inlet in the external uniform flow). Therefore, the three flow problems may be posed as

1. <u>Problem I</u> This problem represents the perturbation potential field due to inlet flow alone.

$$\nabla^2 \phi_1 = 0 \quad \text{in } \Omega \qquad (56a)$$

$$\nabla \phi_1 \bullet \mathbf{n} = U_f \quad \text{on } \Gamma_f \qquad (56b)$$

$$\nabla \phi_1 \bullet \mathbf{n} = 0 \quad \text{on } \Gamma_n \text{ and } \Gamma_c \qquad (56c)$$

$$\nabla \phi_1 \bullet \mathbf{n} = -\frac{A_1}{R^2}\mathbf{r} \bullet \mathbf{n} \quad \text{on } \Gamma_\infty \qquad (56d)$$

$$\nabla \phi_1 \bullet \mathbf{n} = 0 \quad \text{on } \Gamma_b \qquad (56e)$$

where U_f is the uniform fan face velocity, A_1 is a constant to be determined, n is the unit outward normal on the boundary and r is the outward radial vector on the outer boundary Γ_∞ as shown in Fig.1. It is assumed that on the outer boundary Γ_∞ the effect of the flow field is that of a simple source placed at the origin. Hence, the velocity perturbation at the outer boundary is assumed to be radially directed inwards and inversely proportional to the square of the radial distance from the origin[7]. Therefore the boundary condition (56e) at the baffle boundary Γ_b, which is a radial ray, is zero and hence it is impervious to flow perturbations.

2. Problem II This problem represents the perturbation potential field due to a flow to a blank inlet.

$$\nabla^2\phi_2 = 0 \quad \text{in } \Omega \tag{57a}$$

$$\nabla\phi_2 \bullet n = -\nabla\phi_u \bullet n \quad \text{on } \Gamma_f \tag{57b}$$

$$\nabla\phi_2 \bullet n = -\nabla\phi_u \bullet n \quad \text{on } \Gamma_n \text{ and } \Gamma_c \tag{57c}$$

$$\nabla\phi_2 \bullet n = \frac{A_2}{R^2}r \bullet n \quad \text{on } \Gamma_\infty \tag{57d}$$

$$\nabla\phi_2 \bullet n = 0 \quad \text{on } \Gamma_b \tag{57e}$$

where ϕ_u is the external uniform flow velocity potential, A_2 is a constant to be determined and r and n are as mentioned before. Here also the flow at the outer boundary is assumed to be that of a simple source placed at the origin. The flow perturbation is assumed to be radially outwards and varying as $1/R^2$, where R is the radial distance from the origin. As a result, the baffle boundary (equation (57e)) again becomes impervious to flow perturbations.

3. Problem III The uniform external flow field is generated by

$$\nabla^2\phi_u = 0 \quad \text{in } \Omega \tag{58a}$$

---

[7] The velocity field of a simple source varies as $1/R^2$.

51

$$\nabla \phi_u \bullet \mathbf{n} = U_o \,\mathbf{i} \bullet \mathbf{n} \quad \text{on } \Gamma_\infty \text{ and } \Gamma_b \tag{58b}$$

where U_o is the external uniform flow velocity.

Problems I and II are boundary value problems with Neumann boundary conditions. Solutions to these problems are non-unique if the value of the unknown variable is not specified at one point in the domain Ω. The problems also have to satisfy a compatibility criterion which balances the flux of flow across different boundaries. This criterion fixes the values of the constants A_1 and A_2 relative to the flow parameters and, therefore, they are not arbitrary.

A linear superposition of the problems I, II and III gives us the overall boundary value problem of the mean flow

$$\nabla^2 \phi_o = 0 \quad \text{in } \Omega \tag{59a}$$

$$\nabla \phi_o \bullet \mathbf{n} = U_f \quad \text{on } \Gamma_f \tag{59b}$$

$$\nabla \phi_o \bullet \mathbf{n} = 0 \quad \text{on } \Gamma_n \text{ and } \Gamma_c \tag{59c}$$

$$\nabla \phi_o \bullet \mathbf{n} = -\frac{A_1}{R^2}\mathbf{r} \bullet \mathbf{n} + \frac{A_2}{R^2}\mathbf{r} \bullet \mathbf{n} + U_o \,\mathbf{i} \bullet \mathbf{n} \quad \text{on } \Gamma_\infty \tag{59d}$$

$$\nabla \phi_o \bullet \mathbf{n} = U_o \,\mathbf{i} \bullet \mathbf{n} \quad \text{on } \Gamma_b \tag{59e}$$

The flow perturbation effects of the inlet at the outer boundary are small due to the distance of the boundary from the inlet. Also it is to be noted that the perturbation boundary condition at the outer boundary Γ_∞ for problems I and II (equations (56d) and (57d)) tend to balance each other. Therefore, under these conditions the superposed boundary condition (59d) on Γ_∞ can be written approximately as $\nabla \phi_o \bullet \mathbf{n} \approx U_o \,\mathbf{i} \bullet \mathbf{n}$. The superposition of the elementary solutions from problems I, II and III is based on the assumption that the outer boundary condition is imposed at a large distance from the inlet. This effectively makes U_f and U_o independent of each other. For a given value of U_o, any value of U_f can be

chosen once the elementary solutions are available. Variations in U_o requires new potential flow solutions to be computed because the mesh depends on U_o.

B. FINITE ELEMENT FORMULATION

1. Problem I Since the mean flow field is axisymmetric, there is no variation of flow variables in the angular direction. Therefore, the test and trial functions are independent of the angular coordinate θ. Let ψ be a real valued smooth function defined in the axisymmetric domain Ω. Multiplication of the Laplace equation with the test function ψ and integration over the domain yields

$$\int_\Omega \nabla^2 \phi_1 \psi \, d\Omega = 0 \qquad (60)$$

By using Green's theorem, it is determined that

$$\int_\Omega \nabla \phi_1 \bullet \nabla \psi \, d\Omega = \int_S \psi \nabla \phi_1 \bullet \mathbf{n} \, dS \qquad (61)$$

where S denotes surfaces of the axisymmetric volume Ω. Since the problem is independent of θ, the volume integral becomes a surface integral in the x-r plane, and the surface integral becomes a line integral, so that

$$\int_r \int_z \left(\frac{\partial \phi_1}{\partial x} \frac{\partial \psi}{\partial x} + \frac{\partial \phi_1}{\partial r} \frac{\partial \psi}{\partial r} \right) r \, dx \, dr = \int_\Gamma \psi \nabla \phi_1 \bullet \mathbf{n} \, r \, d\Gamma \qquad (62)$$

Incorporation of the natural boundary conditions into equation (62) results in the weak form of the problem

$$\int_r \int_z \left(\frac{\partial \phi_1}{\partial x} \frac{\partial \psi}{\partial x} + \frac{\partial \phi_1}{\partial r} \frac{\partial \psi}{\partial r} \right) r \, dx \, dr = U_f \int_{\Gamma_f} \psi \, r \, d\Gamma - A_1 \int_{\Gamma_\infty} \psi \frac{1}{R^2} \mathbf{r} \bullet \mathbf{n} \, r \, d\Gamma \qquad (63)$$

Therefore the following weak problem may be posed: find $\phi_1 : \Omega \longrightarrow \mathbf{R}^2 \ni$ equation (63) holds $\forall$ smooth $\psi : \Omega \longrightarrow \mathbf{R}^2$. It is to be noted that ϕ and ψ are suitable classes of functions whose derivatives are square integrable (from the space H^1).

A standard Galerkin finite element approximation has been used for the matrix formulation. Basis functions $N_1, N_2, \ldots, N_n$ have been chosen from a finite

dimensional (of dimension n) subspace of H^1. Hence, the test and trial functions can be finitely approximated as

$$\psi = c_i N_i(x, r) \tag{64}$$

$$\phi_1 = d_j N_j(x, r) \tag{65}$$

where c_i's and d_j's are suitable scalars[8]. Substitution of equations (64) and (65) in (63) results in the matrix formulation of the problem

$$\underbrace{\left[\int_r \int_z (\frac{\partial N_i}{\partial x} \frac{\partial N_j}{\partial x} + \frac{\partial N_i}{\partial r} \frac{\partial N_j}{\partial r}) r dx dr \right]}_{K_{ij}} d_j = \underbrace{U_f \int_{\Gamma_f} N_i r d\Gamma - A_1 \int_{\Gamma_\infty} N_i \frac{1}{R^2} \mathbf{r} \bullet \mathbf{n} \, r d\Gamma}_{F_i} \tag{66}$$

where K_{ij} is the i, j entry of the stiffness matrix $[K]$ and F_i is the ith entry in the load vector $\{F\}$.

2. **Problem II**   In a procedure similar to that of problem I, the weak form of problem II is

$$\int_r \int_z (\frac{\partial \phi_1}{\partial x} \frac{\partial \psi}{\partial x} + \frac{\partial \phi_1}{\partial r} \frac{\partial \psi}{\partial r}) r dx dr = - \int_{\Gamma'} \psi \nabla \phi_o \bullet \mathbf{n} \, r d\Gamma + A_2 \int_{\Gamma_\infty} \psi \frac{1}{R^2} \mathbf{r} \bullet \mathbf{n} \, r d\Gamma \tag{67}$$

where $\Gamma' = \Gamma_n \cup \Gamma_f \cup \Gamma_c$ and, ϕ and ψ are from H^1.

As in problem I, a standard Galerkin finite element approximation has been used for the matrix formulation. The matrix formulation of problem II yields

$$\underbrace{\left[\int_r \int_z (\frac{\partial N_i}{\partial x} \frac{\partial N_j}{\partial x} + \frac{\partial N_i}{\partial r} \frac{\partial N_j}{\partial r}) r dx dr \right]}_{K'_{ij}} d_j =$$

$$\underbrace{- \int_{\Gamma_t} N_i \nabla \phi_o \bullet \mathbf{n} \, r d\Gamma + A_2 \int_{\Gamma_\infty} N_i \frac{1}{R^2} \mathbf{r} \bullet \mathbf{n} \, r d\Gamma}_{F'_i} \tag{68}$$

---

[8]Since ϕ is being suitably interpolated between the nodes, d_j's here imply nodal values of the mean flow potential.

where K'_{ij} is the i, j entry of the stiffness matrix $[K']$ and F'_i is the ith entry in the load vector $\{F'\}$.

Details of the stiffness matrix and load vector calculations are dealt with in the next sub-section. The constants A_1 and A_2 of the problems are found by imposing the compatibility condition which balances the flux across the boundaries. For problem I, it balances the flux across the fan face with the flux across the outer boundary Γ_∞, i.e.,

$$U_f \int_{\Gamma_f} rd\Gamma = A_1 \int_{\Gamma_\infty} \frac{1}{R^2} \mathbf{r} \bullet \mathbf{n} \, rd\Gamma$$

or,

$$A_1 = \frac{U_f \int_{\Gamma_f} rd\Gamma}{\int_{\Gamma_\infty} \frac{1}{R^2} \mathbf{r} \bullet \mathbf{n} \, rd\Gamma} \tag{69}$$

For problem II, it balances the flux across the nacelle, centerbody and fan face with the flux across Γ_∞, i.e.,

$$\int_{\Gamma'} \nabla \phi_o \bullet \mathbf{n} \, rd\Gamma = A_2 \int_{\Gamma_\infty} \frac{1}{R^2} \mathbf{r} \bullet \mathbf{n} \, rd\Gamma$$

or,

$$A_2 = \frac{\int_{\Gamma'} \nabla \phi_o \bullet \mathbf{n} \, rd\Gamma}{\int_{\Gamma_\infty} \frac{1}{R^2} \mathbf{r} \bullet \mathbf{n} \, rd\Gamma} \tag{70}$$

C. FINITE ELEMENT CALCULATIONS

The global stiffness matrices and the global load vectors as defined in equations (66) and (68), can be written as the composition of the element stiffness matrices and element load vectors respectively. Therefore, for example, in problem I, we can write

$$[K] = \sum^{n_e} [K^e]$$

$$\{F\} = \sum^{n_e} \{F^e\}$$

55

where n_e is the number of elements in the domain. The element stiffness matrix $[K^e]$ and the element load vector $\{F^e\}$ for the problem are given by

$$K_{ij}^e = \int_{\Omega_e} \left(\frac{\partial N_i^e}{\partial x} \frac{\partial N_j^e}{\partial x} + \frac{\partial N_i^e}{\partial r} \frac{\partial N_j^e}{\partial r} \right) r\, dx\, dr$$

$$F_i^e = U_f \int_{\Gamma_f} N_i^e\, r\, d\Gamma - A_1 \int_{\Gamma_\infty} N_i^e \frac{1}{R^2} \mathbf{r} \bullet \mathbf{n}\, r\, d\Gamma$$

where $\int_{\Omega_e}$ is the surface integral over the domain of the element, $\int_{\Gamma_f}$ and $\int_{\Gamma_\infty}$ are line integrals along element boundaries on the fan face and the outer boundary respectively, and N_i^e is the shape function of the ith node of the element.

Finite element calculations are done based on a parent element with local coordinates ς and η as shown in Figure 4. The element shape functions $\tilde{N}_i^e$ corresponding to each node i in the parent element are standard functions and therefore known.

1. Surface Integrals To perform the finite element calculations on a parent element, an element map is constructed. The transformation under which each element Ω_e in the mesh is the image of a fixed parent element under a coordinate map T_e is constructed as

$$T_e : x = \sum_{i=1}^{nodes} x_i \tilde{N}_i^e(\varsigma, \eta) \tag{72a}$$

$$T_e : r = \sum_{i=1}^{nodes} r_i \tilde{N}_i^e(\varsigma, \eta) \tag{72b}$$

where *nodes* is the number of nodes on the parent element, and is 8 or 9 depending on whether it is an eight or nine-node element. The element Ω_e to which T_e maps the parent element is completely determined by specifying the x, r coordinates (x_i, r_i) of all the nodal points of Ω_e. Element shape functions $N_i^e(x, r)$ are simply

obtained from standard parent element shape functions $\tilde{N}_i^e(\varsigma, \eta)$ by

$$N_i^e(x, r) = \tilde{N}_i^e(\varsigma(x, r), \eta(x, r)) \tag{73}$$

The derivatives of shape functions are obtained by the chain rule of differentiation,

$$\frac{\partial N_i}{\partial x} = \frac{\partial \tilde{N}_i}{\partial \varsigma} \frac{\partial \varsigma}{\partial x} + \frac{\partial \tilde{N}_i}{\partial \eta} \frac{\partial \eta}{\partial x} \tag{74a}$$

$$\frac{\partial N_i}{\partial r} = \frac{\partial \tilde{N}_i}{\partial \varsigma} \frac{\partial \varsigma}{\partial r} + \frac{\partial \tilde{N}_i}{\partial \eta} \frac{\partial \eta}{\partial r} \tag{74b}$$

According to the element map,

$$\frac{\partial x}{\partial \varsigma} = \sum_{k=1}^{nodes} x_k \frac{\partial \tilde{N}_k^e}{\partial \varsigma} \tag{75a}$$

$$\frac{\partial x}{\partial \eta} = \sum_{k=1}^{nodes} x_k \frac{\partial \tilde{N}_k^e}{\partial \eta} \tag{75b}$$

$$\frac{\partial r}{\partial \varsigma} = \sum_{k=1}^{nodes} r_k \frac{\partial \tilde{N}_k^e}{\partial \varsigma} \tag{75c}$$

$$\frac{\partial r}{\partial \eta} = \sum_{k=1}^{nodes} r_k \frac{\partial \tilde{N}_k^e}{\partial \eta} \tag{75d}$$

By using the above relations (equations (72) through (75)), the element stiffness expression K_{ij}^e may be expressed as

$$\int_{\Omega_e} f(x, r) \, r \, dr \, dx = \int_{\Omega_p} \tilde{g}(\varsigma, \eta) \, \tilde{r}(\varsigma, \eta) J(\varsigma, \eta) d\varsigma d\eta \tag{76}$$

where $\int_{\Omega_p}$ is the domain integral over the parent element and $J(\varsigma, \eta)$ is the Jacobian of the transformation T_e given by

$$J(\varsigma, \eta) = \frac{\partial x}{\partial \varsigma} \frac{\partial r}{\partial \eta} - \frac{\partial x}{\partial \eta} \frac{\partial r}{\partial \varsigma} \tag{77}$$

A standard 4 × 4 Gaussian quadrature rule has been used to evaluate the integral. It is important to note that the mean flow calculations have been done both with and without the wave envelope elements. In one case, no distinction has been

made between the elements in regions I and II and the elements in region III. All the regions have isoparametric rectangular finite elements. In another case, shape functions for the wave envelope elements in region III, differ from the rest in the mesh due to the fact that they simulate the inverse square decay behaviour as expected in a field due to a simple source. Mathematically a shape function may be expressed as

$$N_i^{we} = N_i^e \left(\frac{r_i}{r} \right) \tag{78}$$

where N_i^e is the standard shape function of node i at radius r_i. The results in both cases were virtually identical for the flow velocity we are concerned with. For compatibility with the radiation calculations the wave envelope elements were retained.

2. __Boundary Integrals__   Three-node quadratic line elements lie along the boundaries and the generation of their topology and their nodal connectivity have already been discussed in the mesh generation scheme. The calculations of the line integrals are carried out by integrating along those sides of the parent element that are mapped onto the sides Γ^e of the actual element Ω_e along which natural boundary conditions are prescribed. For definiteness, it has been assumed that the side $\varsigma = 1$ has been mapped onto Γ^e. The line integrals have been parametrized with respect to η.

The shape functions used for the line integrals are identical to the standard shape functions for the three-node Lagrangian line element. Element maps are created as discussed before and the elemental arc length is found by

$$d\Gamma = \sqrt{dx^2 + dr^2}$$

or,

$$dΓ = \underbrace{\sqrt{(\frac{\partial x}{\partial \eta})^2 + (\frac{\partial r}{\partial \eta})^2}}_{j} \, d\eta \qquad (79)$$

where j is the jacobian of the transfomation of η onto the arc length parameter in the x-r plane. The dot products, $\nabla \phi_o \bullet n$ for problem I and $r \bullet n$ for problems I and II need to be computed at each node on the relevant boundaries to evaluate the line integrals. Note that the constants A_1 and A_2 need to be evaluated before constructing the load vector.

D. THE SOLUTION PROCEDURE

All of the boundary conditions are of the Neumann type and the differential equation is the Laplace equation. Hence, there is no unique solution to the problems unless a reference value of the mean flow velocity is specified at any point in the domain. This does not affect the results because we are interested in the derivatives of the potential and not in the absolute values of the mean flow potential. By penalization, the potential has been made zero at the intersection of the boundaries $Γ_b$ and $Γ_\infty$. This penalization has been made at the elemental level. When the stiffness matrix of the element which occupies that node at the intersection of $Γ_b$ and $Γ_\infty$, is calculated, a very large value (1.0e15) is added to the diagonal entry in the matrix corresponding to that boundary node. Hence the velocity potential at that node is forced to zero after solution. The penalized stiffess matrix for that boundary element looks like the following :

$$\begin{bmatrix} K_{11} & \cdots & K_{1m} & \cdots & K_{1n} \\ \vdots & \vdots & \vdots & \vdots & \vdots \\ K_{m1} & \cdots & K_{mm} + \frac{1}{\epsilon} & \cdots & K_{mn} \\ \vdots & \vdots & \vdots & \vdots & \vdots \\ K_{n1} & \cdots & K_{nm} & \cdots & K_{nn} \end{bmatrix}$$

where m is the penalized node number (local) and ϵ (1.0e-15) is the penalty param-

eter. As a check, penalization was carried out at a different point in the domain, and the solution was found to differ from the previous solution by an arbitrary constant only.

Since the penalization is carried out at the element level, the stiffess matrix and the load vector are never stored in assembled form. As each element stiffness matrix and load vector is formed, it is written down onto disk along with its nodal connectivity. The frontal solution method of Irons [22] has been used to solve the algebraic system of equations $[K]\{\phi\} = \{F\}$. The principles of this technique are implied by the Gaussian process of forward elmination and back substitution. The frontal process alternates between accumulation of element coefficients (assembly) and elimination. Whenever an element is assembled its nodes are kept in active storage until their elimination. The active in-core storage at a point of time depends only on the "frontwidth" (number of active nodes at that time) which is much smaller than the dimension of the assembled matrix. This drastic reduction in in-core storage is the most important aspect of this scheme. Details of the scheme are, however, not discussed here.

E. SUPERPOSITION OF THE SOLUTION FROM THE THREE PROBLEMS

After the solutions to problems I and II are obtained, they are added to the exterior field velocity potential to obtain the overall mean flow velocity potential of the flow field. Solution to the problem III is the uniform flow field whose velocity potential is given by

$$\phi_u = U_o x + C \tag{80}$$

where C is any arbitrary constant. Problems I and II have been solved by penalizing the velocity potential at the intersection of C_b and C_∞ to be zero. Therefore, in order to be theoretically rigorous, the uniform flow field velocity potential ϕ_u

should be penalized to zero at that point before superposing the three solutions. In this process, the solution vector from the three problems have the same datum of reference. Hence, the value of the constant C no longer remains arbitary and is calculated as

$$C = -U_o x_p \tag{81}$$

where x_p is the x-coordinate of the penalized node at the intersection of C_b and C_∞.

The overall mean flow velocity potential is found out by pointwise addition of the solution vectors from the three flow problems

$$\phi_o = \phi_1 + \phi_2 + \phi_u \tag{82}$$

The solutions to the problems I, II and III have been obtained by an input of unit velocity at the fan face and in the exterior flow field i.e. $U_f = 1$ and $U_o = 1$. Therefore, if the fan face flow Mach number and exterior flow field Mach number are M_f and M_u respectively, the superposed solution is found by

$$\phi_o = M_f \phi_1 + M_u(\phi_2 + \phi_u) \tag{82}$$

F. RESULTS AND DISCUSSIONS

The solution to the mean flow problems I and II are the velocity potential values at the nodes in the finite element mesh. Contours of constant velocity potential in the field have been plotted in Figures 20 and 21. Figure 20 corresponds to inlet flow alone (problem I) with a unit velocity on the fan face and Figure 21 corresponds to flow into a blank inlet (problem II) with a unit far field flow velocity. The contour curves for both the problems are more or less parallel to the fan face C_f inside the nacelle and they form concentric circles outside the inlet.

61

The equipotential lines are always orthogonal to the streamlines in a flow field, and since the velocity on C_∞ is radially directed for problems I and II, the constant potential curves in the far field are supposed to meet C_∞ tangentially. From Figures 20 and 21 it is obvious that this condition is satisfied upto a certain angular distance from the x-axis but at high angles, the contour curves do not quite meet C_∞ tangentially. This is probably because the finite element mesh for the acoustic radiation problem is also used for solving the mean flow problem. The mesh in region III, corresponding to the wave envelope elements for the acoustic radiation problem, is quite coarse for the mean flow problem. This may lead to slight numerical inaccuracies in the finite element solution in the far field. However, it is not of much concern for the present problem because the perturbation potential in the far field is small. Therefore, when the two flow fields are superposed with the external uniform mean flow, the effect of the flow perturbation in the superposed far field is not noticeable. This is apparent from Figure 22 which shows the equipotential lines in the superposed field with a fan face Mach number of 0.5 and a uniform far field Mach number of 0.3. It is also to be noted from Figure 22 that on the far field boundary, the flow is almost fully dominated by the external uniform mean flow. Therefore the comment made at the end of Section V.A, that the perturbation boundary condition on C_∞ for problems I and II (equations (56d) and (57d)) balance each other, is very well satisfied.
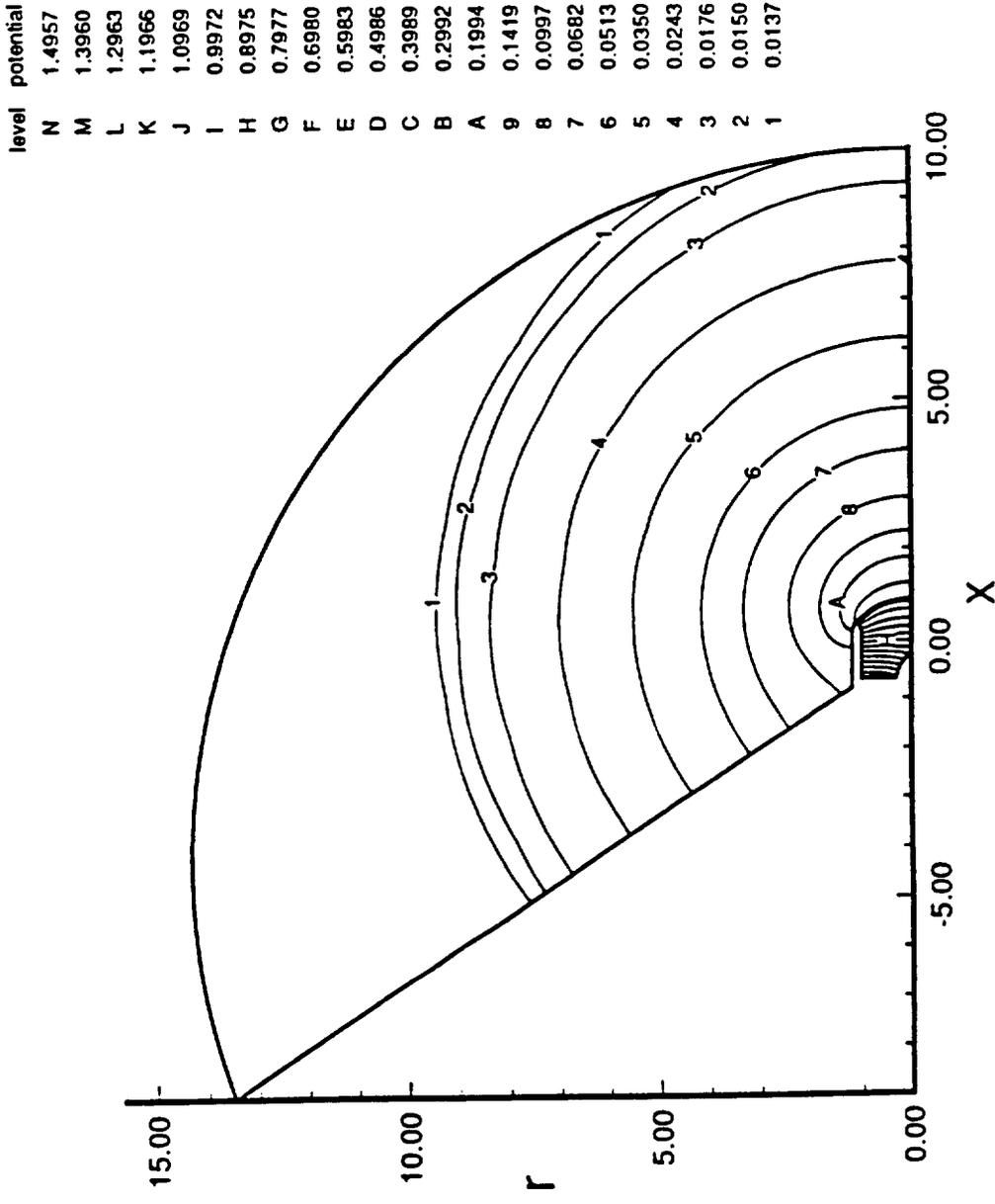
Figure 20: Contours of mean flow perturbation potential due to inlet flow alone; $U_I = 1$

level	potential
N	1.4957
M	1.3960
L	1.2963
K	1.1966
J	1.0969
I	0.9972
H	0.8975
G	0.7977
F	0.6980
E	0.5983
D	0.4986
C	0.3989
B	0.2992
A	0.1994
9	0.1419
8	0.0997
7	0.0682
6	0.0513
5	0.0350
4	0.0243
3	0.0176
2	0.0150
1	0.0137

level	potential
M	-0.0211
L	-0.0231
K	-0.0295
J	-0.0424
I	-0.0637
H	-0.1026
G	-0.1368
F	-0.1847
E	-0.2367
D	-0.3550
C	-0.4734
B	-0.5917
A	-0.7100
9	-0.8284
8	-0.9467
7	-1.0651
6	-1.1834
5	-1.3017
4	-1.4201
3	-1.5384
2	-1.6568
1	-1.7751
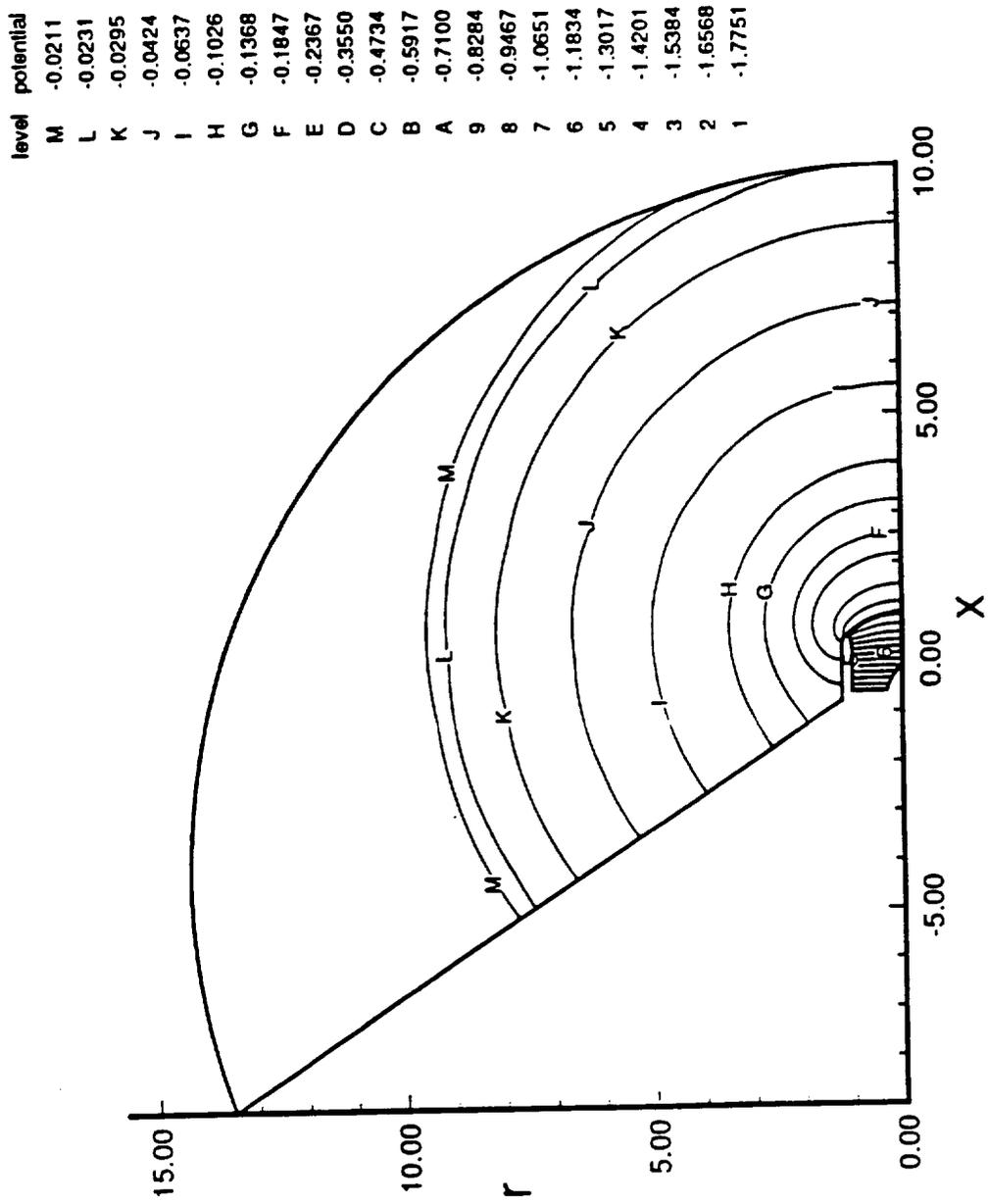
Figure 21: Contours of mean flow perturbation potential due to flow to a blank inlet; $U_o = 1$

level	potential
H	-0.2477
G	-0.7432
F	-1.2387
E	-1.7342
D	-2.2296
C	-2.4003
B	-2.5978
A	-2.7251
9	-2.8660
8	-3.0391
7	-3.2206
6	-3.4683
5	-3.7161
4	-3.9638
3	-4.4593
2	-4.9548
1	-5.4502
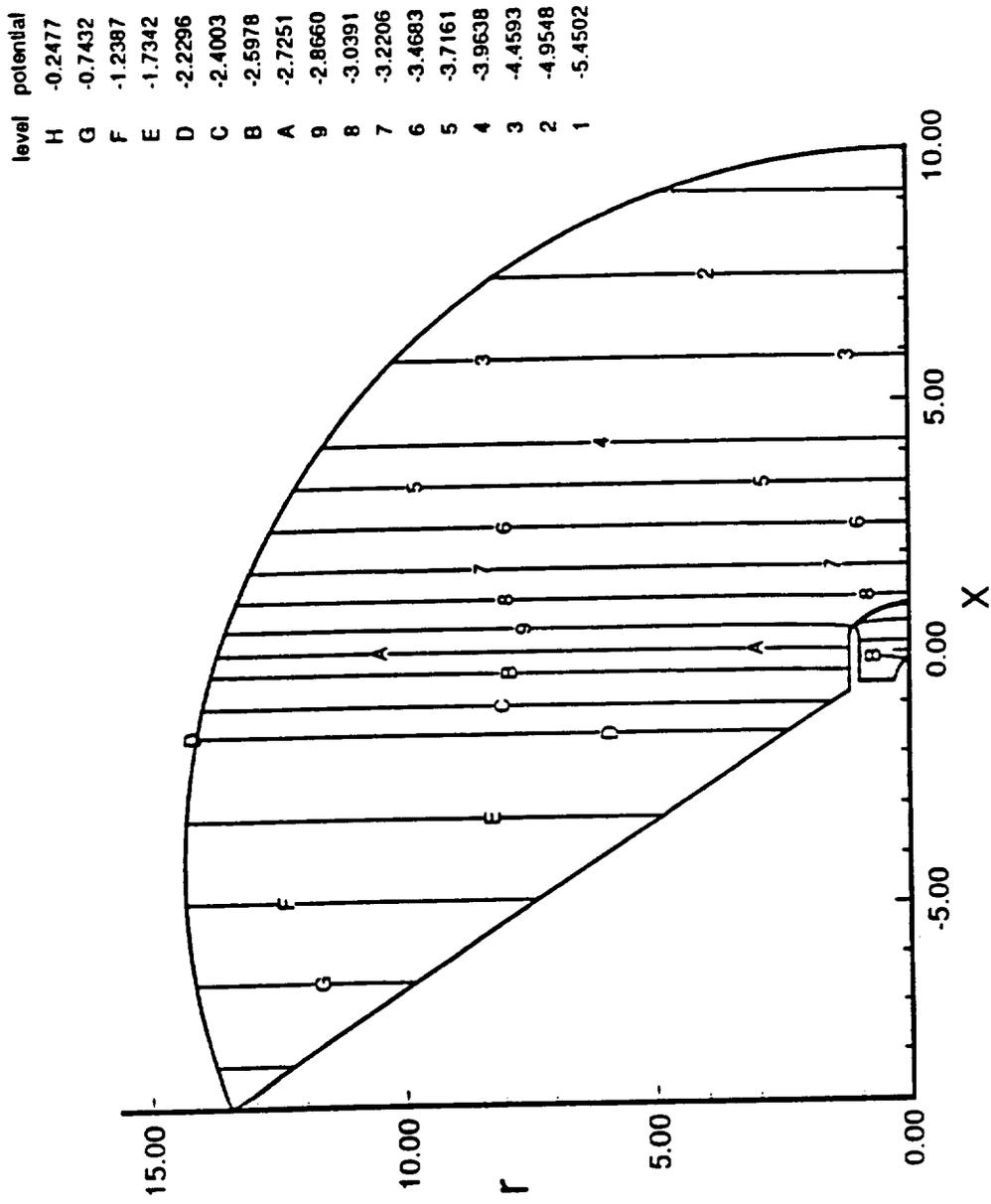
Figure 22: Contours of superposed mean flow velocity potential; far field Mach number -0.3, fan face Mach number -0.5

VI. ACOUSTIC RADIATION PROBLEM

A. WEAK FORM AND FINITE ELEMENT FORMULATION

The governing equation for the acoustics problem with flow is given by equation (15) in Section II.D

$$\frac{\partial \rho}{\partial t} + \nabla \bullet (\rho_o \nabla \phi + \rho \nabla \phi_o) = 0$$

where ρ is given by equation (12) of Section II.D,

$$\rho = -\frac{\rho_o}{c_o^2}[\frac{\partial \phi}{\partial t} + (\nabla \phi_o \bullet \nabla \phi)]$$

c_o being the nondimensional speed of sound in mean flow.

Solutions to the above two equations are desired in the case of a harmonic source on the fan face C_f with time and angular dependence given by $e^{i(\eta_r t - m\theta)}$, where η_r is the nondimensional input frequency ($\eta_r = \omega R/c_r$, ω is the input frequency) and m is the angular mode number. Since a steady state solution is sought, temporal derivatives of acoustic variables are replaced by $\partial/\partial t = i\eta_r$. To formulate a weak problem, let us assume that the trial and test functions are of the form

$$\phi(x,r,\theta,t) \quad = \quad \phi(x,r)e^{i(\eta_r t - m\theta)} \tag{83}$$

$$\psi(x,r,\theta,t) \quad = \quad \psi(x,r)e^{-i(\eta_r t - m\theta)} \tag{84}$$

The fact that the test function is taken to be the complex conjugate of the trial function is consistent with the definition of the inner product of a complex Hilbert space.

Multiplication of the governing equation (15) with the test function ψ and integration over the domain yields

$$\int_V [\psi \frac{\partial \rho}{\partial t} + \psi \nabla \bullet (\rho_o \nabla \phi + \rho \nabla \phi_o)] \, dV = 0 \tag{85}$$

66

Integration of the divergence term in equation (85) by parts yields

$$\int_V [\psi \frac{\partial \rho}{\partial t} - \nabla \psi \bullet (\rho_o \nabla \phi + \rho \nabla \phi_o)] \, dV = - \int_S \psi (\rho_o \nabla \phi + \rho \nabla \phi_o) \bullet \mathbf{n} \, dS \qquad (86)$$

where $\int_V$ and $\int_S$ are the volume integral and the surface integral respectively in the three dimensional space in and around the inlet. Since the trial and test functions have been conveniently chosen, the following weak problem is posed in the (x, r) domain Ω : find $\phi(x,r) : \Omega \longrightarrow \mathbf{C}^2 \ni$ equation (86) holds $\forall$ smooth $\psi(x,r) : \Omega \longrightarrow \mathbf{C}^2$ where

$$\psi \frac{\partial \rho}{\partial t} - \nabla \psi \bullet (\rho_o \nabla \phi + \rho \nabla \phi_o) \;=\; i\eta_r \rho \psi - \rho_o \frac{m^2}{r^2} \phi \psi - \rho u \psi_{,x}$$
$$- \rho v \psi_{,r} - \rho_o \phi_{,x} \, \psi_{,x} - \rho_o \phi_{,r} \, \psi_{,r} \qquad (87)$$

Here u $(= \partial \phi_o / \partial x)$ and v $(= \partial \phi_o / \partial r)$ are the x and r components of the mean flow velocities in the domain Ω. $()_{,x}$ and $()_{,r}$ are the derivatives of variables with respect to x and r in the field.

Substitution of ρ in the right hand side of equation (87) by equation (12) of Section II.D yields

$$\psi \frac{\partial \rho}{\partial t} - \nabla \psi \bullet (\rho_o \nabla \phi + \rho \nabla \phi_o) =$$
$$\frac{\rho_o}{c_o^2} [(\eta_r^2 - \frac{c_o^2 m^2}{r^2}) \phi \psi + i\eta_r c_o u (\phi_{,x} \psi - \phi \psi_{,x}) + i\eta_r c_o v (\phi_{,r} \psi - \phi \psi_{,r})$$
$$- (c_o^2 - u^2) \phi_{,x} \, \psi_{,x} - (c_o^2 - v^2) \phi_{,r} \, \psi_{,r} + uv (\phi_{,x} \psi_{,r} + \phi_{,r} \psi_{,x})] \qquad (88)$$

It is to be noted that the right hand side of equation (88) has products of the functions ϕ and ψ or their derivatives with respect to x and r. Since the functions are complex conjugates of one another, the exponential terms of ϕ and ψ as in equations (83) and (84) cancel out here. Therefore the right hand side of equation (88) is an expression in coordinates x and r only. The volume integral in the left hand side of equation (86) reduces to a surface integral over the domain Ω in the

following way

$$\int_V g(x,r,\theta,t)\, r\, dr\, dx\, d\theta \;=\; \int_V f(x,r)\, r\, dr\, dx\, d\theta$$
$$=\; 2\pi \int_\Omega f(x,r)\, r\, dr\, dx \tag{89}$$

Similarly we can take out a factor 2π from the right hand side of equation (86) and reduce the surface integral to a line integral.

$$\int_S h(x,r,\theta,t)\, r\, d\theta\, ds \;=\; \int_S p(x,r)\, r\, d\theta\, ds$$
$$=\; 2\pi \int_\Gamma p(x,r)\, r\, ds \tag{90}$$

where ds is the elemental arc length. The constant factor of 2π therefore cancels out from both sides in equation (86).

The trial and the test functions ϕ and ψ respectively are from complex H^1 space. In an analogous procedure to that carried out in Section V.B for the mean flow problem, the trial and test functions are finitely approximated using the standard Galerkin method. The resulting finite dimensional subspace of H^1 is then constructed. The resulting matrix formulation of the problem yields the global stiffness matrix expression of the problem

$$K_{ij} = \int_r \int_x h(x,r)\, r\, dr\, dx \tag{90}$$

where

$$\begin{aligned}
h(x,r) \;=\; & \frac{\rho_o}{c_o^2}\,[(\eta_r^2 - \frac{c_o^2 m^2}{r^2})N_i N_j + i\eta_r c_o u(N_{i,x}\, N_j - N_i N_{j,x}) \\
& + i\eta_r c_o v(N_{i,r}\, N_j - N_i N_{j,r}) - (c_o^2 - u^2)N_{i,x}\, N_{j,x} \\
& - (c_o^2 - v^2)N_{i,r}\, N_{j,r} + uv(N_{i,x}\, N_{j,r} + N_{i,r}\, N_{j,x})]
\end{aligned} \tag{91}$$

$N_1, N_2, \ldots, N_n$ are basis functions of the finite n-dimensional subspace of H^1.

Conventional eight-node quadratic isoparametric elements have been used to model the regions I and II and hence the interpolation functions used here were the

same as those for the mean flow problem. The outer region III has been modeled with eight-node wave envelope elements. As discussed in Section II.E, the wave envelope shape functions are constructed on the assumption that at a sufficiently large distance from the inlet, the acoustic field approximates that of a point source placed at the origin and are of the form

$$\tilde{N}_i'(\varsigma, \eta) = \tilde{N}_i^e(\varsigma, \eta) \frac{R_i}{R} e^{-i\eta_r(\psi - \psi_i)}$$

where $1/R$ is the nature of decay in the acoustic field due to a point source and ψ is the equation of constant phase surfaces (refer to Section II.E). The wave envelope elements are not truly isoparametric in the sense that the element maps are created using the standard eight-node quadratic shape functions, but the solution is interpolated inside the element using the modified "wave envelope" shape functions.

B. ACOUSTIC BOUNDARY CONDITIONS

Equation (86) yields a surface integral of form

$$\int_S \psi(\rho_o \nabla \phi + \rho \nabla \phi_o) \bullet \mathbf{n} \, dS$$

which can be transformed to a line integral over the boundaries in the (x, r) domain as has been discussed before. The significance of the combination of terms in the integrand is clear because it represents the natural boundary terms which are generated by the use of the divergence theorem. The following discussion investigates what form the integrand $[\psi(\rho_o \nabla \phi + \rho \nabla \phi_o) \bullet \mathbf{n}]$ assumes on different boundaries of the computational domain Ω.

1. Far Field Boundary C_∞ On the outer boundary C_∞ in the far field a Sommerfeld radiation condition has been applied. Since there is no reflection in the far field this condition assumes that on C_∞ only an outgoing wave exists. In

69

fact, the modeling of region III with wave envelope elements is complete only when this radiation boundary condition at the outer boundary is properly implemented.

At C_∞ the acoustic field is assumed to be that of a simple source in uniform flow and placed at the origin. The potential for a harmonic acoustic monopole (simple source) in a uniform x-direction flow of Mach number M can be written as

$$\phi = \frac{A}{R} e^{(i\eta_r t - k\psi)} \tag{92}$$

where

$$A = \frac{\sqrt{1-M^2} f_o}{4\pi\rho_o} \tag{93}$$

$$R = \sqrt{x^2 + (1-M^2)r^2} \tag{94}$$

$$\psi = \frac{1}{(1-M^2)}(-Mx + R) \tag{95}$$

$$k = \frac{\eta_r}{c_o} \tag{96}$$

f_o is the source strength, η_r is the source frequency, ρ_o is the mean flow density and k is the local wave number. By taking appropriate derivatives of the acoustic potential ϕ we get

$$\frac{\partial\phi}{\partial x} = \left[\frac{-ik}{(1-M^2)}(-M + \frac{x}{R}) - \frac{x}{R^2}\right]\phi \tag{97}$$

$$\frac{\partial\phi}{\partial r} = \left[-ik\frac{r}{R} - (1-M^2)\frac{r}{R^2}\right]\phi \tag{98}$$

By expanding the right hand side terms of equation (12), we obtain the following expression for acoustic density in the field

$$\rho = -\frac{\rho_o}{c_o}\left[ik\phi + M\frac{\partial\phi}{\partial x}\right] \tag{99}$$

Substituting ρ in $(\rho_o\nabla\phi + \rho\nabla\phi_o)$ using equation (99), we obtain

$$(\rho_o\nabla\phi + \rho\nabla\phi_o) = \rho_o\left[\frac{\partial\phi}{\partial x}(1-M^2) - ikM\phi\right]\bar{x} + \rho_o\frac{\partial\phi}{\partial r}\bar{r} \tag{100}$$

70

where $\vec{x}$ and $\vec{r}$ are the unit vectors along the x and r axes respectively. Using equations (97) and (98), equation (100) can be rearranged to yield

$$(\rho_o \nabla \phi + \rho \nabla \phi_o) = \rho_o \left[-\frac{ik}{R} - \frac{(1-M^2)}{R^2} \right] (\phi)(x\vec{x} + r\vec{r}) \qquad (101)$$

Therefore, the natural boundary condition at C_∞ representing the Sommerfeld radiation condition for a harmonic acoustic monopole in a uniform flow parallel to the x-axis is

$$(\rho_o \nabla \phi + \rho \nabla \phi_o) \bullet \mathbf{n} = \frac{\rho_o}{R} \left[-ik - \frac{(1-M^2)}{R} \right] (\phi)(n_x x + n_r r) \qquad (102)$$

where n_x and n_r are the x and r components of the outward unit normal $\mathbf{n}$ on the outer boundary.

In the far field, the mesh is constructed on the basis of constant phase circles in uniform flow and acoustic rays from the origin. Hence the outer boundary C_∞ as shown in Figure 23 is a constant phase circle. By taking ψ as constant in equation (95) we obtain the equation for such a circle to be

$$(x - M\psi)^2 + r^2 = \psi^2 \qquad (103)$$

So, a constant phase circle is of radius ψ and having origin at $x = M\psi$ and $r = 0$. From Figure 23 it is obvious that

$$n_x = cos\beta = \frac{x - M\psi}{\psi} \qquad (104)$$

$$n_r = sin\beta = \frac{r}{\psi} \qquad (105)$$

thus

$$(n_x x + n_r r) = \frac{x^2 - M\psi x + r^2}{\psi} \qquad (106)$$

With some algebraic manipulation on the right hand side of equation (106) it can be shown that

$$n_x x + n_r r = R \qquad (107)$$

71

Therefore the boundary integral on C_∞ can be expressed as

$$\int_{\Gamma_\infty} \psi(\rho_o \nabla \phi + \rho \nabla \phi_o) \bullet \mathbf{n}\, r\, ds = \int_{\Gamma_\infty} \rho_o \left[-ik - \frac{(1 - M^2)}{R} \right] \phi \psi\, r\, ds \qquad (108)$$

As R becomes large (as it is for the outer boundary C_∞), the second term in the integral becomes negligible with respect to the first and the boundary integral may be approximated by

$$\int_{\Gamma_\infty} \psi(\rho_o \nabla \phi + \rho \nabla \phi_o) \bullet \mathbf{n}\, r\, ds \approx \int_{\Gamma_\infty} -\rho_o ik \phi \psi\, r\, ds \qquad (109)$$

In the right hand side of the equation (109), the local wave number $k(= \eta_r / c_o)$ can be replaced by η_r because at C_∞, $c_o = 1$. It is important to note that this form of the integral assumes a "ρc" termination i.e. the wave at C_∞ behaves *locally* as a plane wave. Therefore, it will be incorrect to compute the boundary integral given by equation (109) until and unless the outer boundary C_∞ is quite far away from the inlet.

In the finite element matrix formulation of the weak problem (86), the boundary integral (109) yields an $n \times n$ matrix A given by

$$A_{ij} = \int_{\Gamma_\infty} i\rho_o k N_i N_j\, r\, ds \qquad (110)$$

where n is the number of degrees of freedom (= number of nodes) on the outer boundary C_∞. The outer boundary matrix A is therefore transposed to the left hand side of the equation (86) and appropriately added to the stiffness matrix given by equation (90) using the nodal connectivity of the outer boundary line elements.

2. Baffle Boundary C_b In an attempt to reduce the size of the computational domain a baffle surface C_b has been modeled at an angle α to the x-axis (see Figure 24) which would allow flow through it but affect the radiated acoustic field minimally. The baffle C_b is swept back far enough from the main direction

of sound propagation with the hope that it does not interfere with the forward radiated acoustic field. In the region III of wave envlope elements, the natural boundary condition given by equation (102) is also valid on C_b since it is valid for arbitrary surface shapes. We now investigate the value of the term $(n_x x + n_r r)$ on C_b.

Referring to Figure 24, we observe that the line representing the baffle C_b is a straight line passing through the origin and at an angle α to x-axis. Therefore its equation is

$$y(x,r) = r - \gamma x = 0 \tag{111}$$

where $\gamma = \tan\alpha$ is the slope of the line. The outward unit normal n to C_b can be written as

$$\mathbf{n} = \frac{\nabla y}{|\nabla y|} = \frac{1}{\sqrt{1+\gamma^2}}(-\gamma \vec{\mathbf{x}} + \vec{\mathbf{r}}) \tag{112}$$

Thus

$$(n_x x + n_r r) = \frac{1}{\sqrt{1+\gamma^2}}(-\gamma x + r) = 0 \tag{113}$$

So the boundary integral vanishes on C_b in the wave envelope region. Since the region II is much smaller than region III, the same approximation has been made there while computing the boundary integral on C_b with the expectation that any errors induced will be localised and will not contribute significantly to the forward radiated acoustic field.

3. The Centerline   Since the centerline corresponds to $r = 0$, the boundary integral on the centerline provides no contribution for the axisymmetric formulation, just as in the mean flow problem.

4. The Nacelle Surface C_n and Centerbody   The nacelle surface C_n and the centerbody are impervious to both steady mean flow and acoustic perturbations.
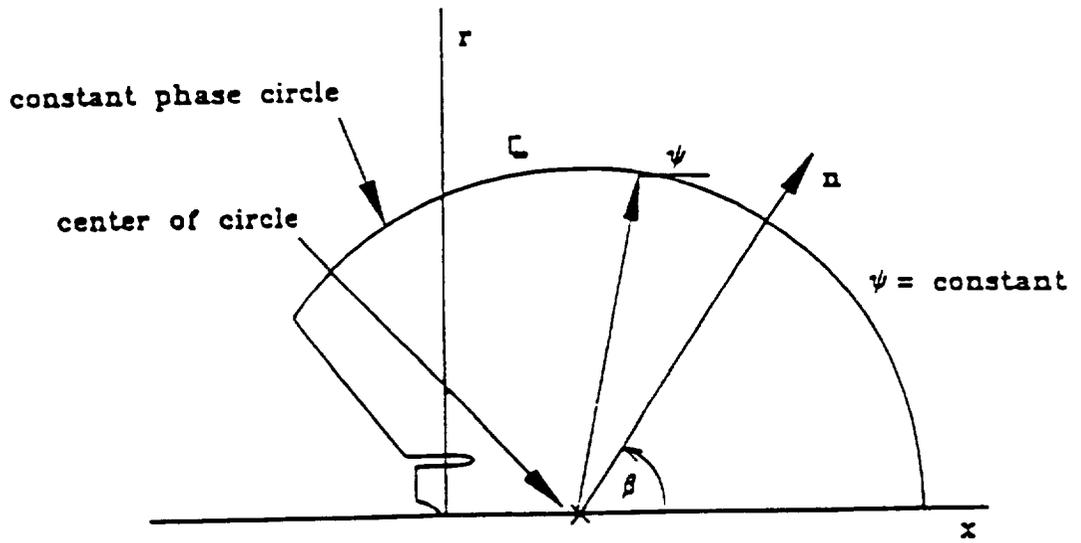
Figure 23: Far field mesh geometry
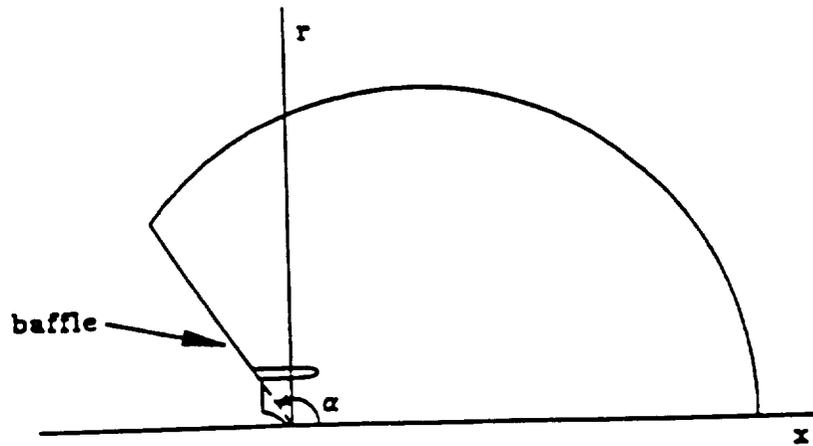
Figure 24: Baffle geometry

Therefore

$$\nabla \phi_o \bullet \mathbf{n} = 0$$

$$\nabla \phi \bullet \mathbf{n} = 0$$

Hence there is no contribution to the boundary integral in equation (86) from the nacelle surface and the centerbody.

5. The Fan Face   The sound source at the fan face C_f has been modeled in terms of the duct mode amplitudes. The boundary C_f has been taken to be at a locally uniform part of the inlet. The acoustic potential field due to it has been expressed as a combination of incident and reflected (positive and negative) uniform duct eigenfunctions. The eigenvalues and the eigenvectors from the finite element duct eigenvalue problem discussed in Section IV have been used to model the natural boundary condition on the fan face C_f. The acoustic potential can be conveniently written as

$$\phi = \sum_{n=1}^{N} \phi_n^+ e^{-k_{x_n}^+ z} e_n(r) + \sum_{r=1}^{N} \phi_n^- e^{-k_{x_n}^- z} e_n(r) \tag{114}$$

where ϕ^+ and ϕ^- are incident and reflected duct modal amplitudes, $k_{x_n}^{\pm}$ is the axial wavenumber corresponding to positive or negative modes given by equation (50), N is the number of modes retained in the expansion and $e_n(r)$ is the continuous duct eigenfunction corresponding to each retained duct mode. Note that the eigenfunctions $e_n(r)$ are the same for propagation in the positive and negative direction.

On the fan face boundary the integrand of the boundary integral can be expressed by using equation (12) as

$$(\rho_o \nabla \phi + \rho \nabla \phi_o) \bullet \mathbf{n} = -\rho_o \left[\left(1 - M_f^2 \right) \frac{\partial \phi}{\partial x} - i \frac{\eta_r}{c_o} M_f \phi \right] \tag{115}$$

75

where M_f ($= \nabla\phi_o/c_o$) is the axially directed local fan face Mach number. Substitution of equation (114) in (115) yields

$$(\rho_o \nabla\phi + \rho\nabla\phi_o) \bullet \mathbf{n} = \sum_{n=1}^{N} i\rho_o \left[\left(1 - M_f^2\right) k_{x_n}^+ + \eta_r \frac{M_f}{c_o} \right] \phi_n^+ e^{-k_{x_n}^+ x} e_n(r)$$
$$+ \sum_{n=1}^{N} i\rho_o \left[\left(1 - M_f^2\right) k_{x_n}^- + \eta_r \frac{M_f}{c_o} \right] \phi_n^- e^{-k_{x_n}^- x} e_n(r) \quad (116)$$

where c_o is the nondimensional local speed of sound in flow at the fan face.

On the fan face ($x = 0$, x being measured from the fan face) the acoustic velocity potential can be conveniently expressed in terms of duct mode amplitudes by substituting $x = 0$ in equation (114)

$$\phi = \left\{ \begin{array}{ccccccc} e_1(r) & \ldots & e_N(r) & e_1(r) & \ldots & e_N(r) \end{array} \right\} \left\{ \begin{array}{c} \phi_1^+ \\ \vdots \\ \phi_N^+ \\ \phi_1^- \\ \vdots \\ \phi_N^- \end{array} \right\} \quad (117)$$

Similarly equation (115) can be rewritten as

$$(\rho_o \nabla\phi + \rho\nabla\phi_o) \bullet \mathbf{n} = i \left\{ \begin{array}{ccccccc} \alpha_1^+ e_1(r) & \ldots & \alpha_N^+ e_N(r) & \alpha_1^- e_1(r) & \ldots & \alpha_N^- e_N(r) \end{array} \right\} \left\{ \begin{array}{c} \phi_1^+ \\ \vdots \\ \phi_N^+ \\ \phi_1^- \\ \vdots \\ \phi_N^- \end{array} \right\}$$
$$(118)$$

where

$$\alpha_n^\pm = \rho_o \left[\left(1 - M_f^2\right) k_{x_n}^\pm + \eta_r \frac{M_f}{c_o} \right] \quad (119)$$

So the boundary integral on the fan face C_f can be cast as

$$\int_{\Gamma_f} \psi(\rho_o \nabla\phi + \rho\nabla\phi_o) \bullet \mathbf{n} \, r ds = i \int_{\Gamma_f} \psi \{\alpha^\pm B\} \left\{ \begin{array}{c} \phi_n^+ \\ \phi_n^- \end{array} \right\} r ds \quad (120)$$

where

$$\{B\} = \{e_1(r) \ldots e_N(r) \ e_1(r) \ldots e_N(r)\} \quad (121)$$

76

a. Forced Input to the Acoustics Problem   The input to the acoustic radiation problem has been given in terms of specified values of the incident modal amplitudes ϕ^+, the reflected modal amplitudes ϕ^- are obtained as a part of the solution. To be precise, the acoustic pressure amplitudes p_n^+ are the inputs and by using equation (16) in Section II.D, they are related to the velocity potential modal amplitudes by

$$p_n^\pm = -i\rho_0\eta_r \left(1 - U_f \frac{k_{z_n}^\pm}{\eta_r}\right) \phi_n^\pm \tag{122}$$

In order to use a forced input on the fan face C_f, generalized coordinates have been used on the fan face rather than the nodal values of the velocity potential. The generalized coordinates used for this problem are the velocity potential modal amplitudes $\phi^\pm$. Equation (117) suggests a convenient transformation from the nodal values of the velocity potential on C_f to the generalized coordinates by

$$\{\phi\}_{C_f} = [M] \left\{ \begin{array}{c} \phi_n^+ \\ \\ \phi_n^- \end{array} \right\} \tag{123}$$

where $\{\phi\}_{C_f}$ is a $NF \times 1$ column vector, NF being the number of nodes on the fan face, and $[M]$ is the $NF \times 2N$ transformation matrix (N is the number of incident modes and the number of incident and reflected modes are the same). Since $[M]$ is the matrix of acoustic eigenvectors on C_f, the modal matrix resulting from the finite element duct eigenvalue problem serves the purpose.

This transformation is applied element by element on the fan face C_f. In each element on the fan face the boundary nodes (nodes which belong to a fan face element and lie on the fan face boundary C_f) are transformed to the generalized coordinates but the interior nodes (nodes which belong to a fan face element but do not lie on the fan face boundary) remain intact. This tranformation is done by

creating an element transformation matrix $[\bar{M}]^e$ given by the following relation

$$\{\phi\}^e = \left[\bar{M}\right]^e \left\{ \begin{array}{c} \phi_n^+ \\ \phi_n^- \\ \phi_i \end{array} \right\} \tag{124}$$

where $\{\phi\}^e$ is the $NODE \times 1$ column vector consisting of nodal values of velocity potential, $NODE$ being the number of nodes in a fan face element. The column vector on the right hand side is partitioned so that the first $2N$ generalized coordinates are the modal amplitudes and the remaining degrees of freedom ϕ_i are the velocity potential values of nodes which are interior. Note that the element transformation matrix $[\bar{M}]^e$ will be different for different fan face elements.

The effect of this transformation is that in the Galerkin formulation of the problem the element stiffness matrix $[K^e]$, which is basically the integral given by equation (90) when calculated over an element, corresponding to elements on the boundary C_f are expressed in the generalized coordinates given by the column vector in the right hand side of equation (124). The transformed fan face element stiffness matrices $[K_t^e]$ are of the form,

$$[K_t^e] = [\bar{M}]^{e^T}[K^e][\bar{M}]^e \tag{125}$$

Here $[K_t^e]$ is a $(NODE - NB + 2N) \times (NODE - NB + 2N)$ square matrix, where NB is the number of fan face nodes belonging to one fan face element. It is importrant to note that the first $2N$ generalized coordinates consisting of the incident and reflected modal amplitudes $\phi^\pm$ are common to all the elements along the fan face boundary C_f but, the remaining degrees of freedom ϕ_i corresponding to interior nodes of a fan face element are different for different elements.

b. Finite Element Formulation of the Boundary Integral   The boundary integral on the fan face C_f assumes a very convenient form in the Galerkin method

where the test or the weighting function is the same as the shape function. Under this condition the boundary integral given by equation (120) assumes the form

$$i \int_{\Gamma_f} \psi \{\alpha^{\pm} B\} \left\{ \begin{array}{c} \phi_n^+ \\ \phi_n^- \end{array} \right\} r ds = i \int_{\Gamma_f} \{B\}^T \{\alpha^{\pm} B\} \left\{ \begin{array}{c} \phi_n^+ \\ \phi_n^- \end{array} \right\} r ds \qquad (126)$$

Now $\{B\}$ is the row vector consisting of continuous duct eigenfunctions corresponding to each retained duct mode. The information that we have regarding the duct modes is the finite element modal matrix $[M]$ where each column represents a duct mode. But such eigenvectors are discrete. We approximate the continuous duct eigenfunctions by the discrete finite element eigenvectors in the following way

$$\{B\} = \{N\} [M] \qquad (127)$$

where $\{N\}$ is the row vector of quadratic basis functions $N_1, N_2, \ldots, N_{NF}$ corresponding to the finite element duct eigenvalue problem. Substitution of equation (127) in (126) yields

$$i \int_{\Gamma_f} \{B\}^T \{\alpha^{\pm} B\} \left\{ \begin{array}{c} \phi_n^+ \\ \phi_n^- \end{array} \right\} r ds = i[M]^T \left(\int_{\Gamma_f} \{N\}^T \{N\} r dr \right) \left[\alpha^{\pm} M \right] \left\{ \begin{array}{c} \phi_n^+ \\ \phi_n^- \end{array} \right\} \qquad (128)$$

The right hand side of equation (128) is evaluated element by element on the fan face and each of these element integrals yields a $2N \times 2N$ square matrix $[C]^e$ given by

$$[C]^e = i[\bar{M}]^{eT} \left(\int_{\Gamma_f^e} \{N^e\}^T \{N^e\} r dr \right) \left[\alpha^{\pm} \bar{M} \right]^e \left\{ \begin{array}{c} \phi_n^+ \\ \phi_n^- \end{array} \right\} \qquad (129)$$

The matrix $[C]^e$ calculated in one fan face element is then appended to its corresponding transformed element stiffness matrix $[K_t^e]$ given by equation (125). Since the first $2N$ generalized coordinates are the $\phi^{\pm}$, the matrix $[C]^e$ is appended to the topmost and leftmost $2N \times 2N$ block of $[K_t^e]$. Thus the non zero boundary conditions in the problem are introduced through the element stiffness matrices of the boundary elements.

C. THE SOLUTION PROCEDURE

The frontal scheme of Irons [22], adapted for unsymmetric problems, has been used to solve the algebraic system of equations

$$[K] \left\{ \begin{array}{c} \phi^+ \\ \phi^- \\ \phi_i \end{array} \right\} = 0 \tag{130}$$

The solution procedure is very similar to that implemented for the mean flow problem. The first N generalized coordinates corresponding to ϕ^+ are penalized to force in the required input values for the acoustic radiation problem in a manner similar to the mean flow case. Such penalization has been carried out at the elemental level.

D. RESULTS AND DISCUSSIONS

In this section several example numerical results are presented to demonstrate the improvements in the finite element model of the acoustic radiated field of the turbofan inlet. The numerical data that can be validated by experiment is that of the acoustic pressure in the field. The solution of the acoustic radiation problem yields the acoustic velocity potential at the nodes of the finite element mesh. The solution is then post processed to yield the acoustic pressure at the nodes by

$$p = -\rho_o[i\eta_r\phi + (\nabla\phi_o \bullet \nabla\phi)] \tag{131}$$

which is obtained by using equation (16) in Section II.D. From equation (131) it is obvious that the x and r derivatives of both the mean flow and acoustic velocity potential need to be evaluated at the finite element nodes before the nodal acoustic pressure can be calculated. The differential equations governing the mean flow and acoustic radiation problem are of second order and therefore the finite element solution space is from H^1. This implies that though the solution

is continuous across interelement boundaries, the derivatives need not necessarily have the same property. Once the velocity potential at the nodes of an element are known, the x and r derivatives at any point in the element can be obtained by

$$\frac{\partial \phi}{\partial x} = \sum_{i=1}^{n_e} \phi_i \frac{\partial N_i^e}{\partial x} \qquad (132a)$$

$$\frac{\partial \phi}{\partial r} = \sum_{i=1}^{n_e} \phi_i \frac{\partial N_i^e}{\partial r} \qquad (132b)$$

where n_e is the number of nodes in an element. Following the above approach, the value of the x or r derivative at a node (which is shared by more than one element) might be different when evaluated in the different elements sharing that node, since the derivative need not be continuous across interelement boundaries. In the original model, a simple average of the nodal derivatives from different elements sharing a node was performed to obtain an unique value of the derivative at that particular node. From Figure 25, it is clear that at node j, which is shared by all the four elements, the derivative with respect to x is obtained for example, by

$$\phi_{(j),x} = \frac{\phi^1{}_{,x} + \phi^2{}_{,x} + \phi^3{}_{,x} + \phi^4{}_{,x}}{4}$$

where ϕ_x^i is the derivative with respect to x evaluated at node j within element i. Similar calculations are performed to obtain the derivative with respect to r.

Test runs have been made at different combinations of source frequencies and angular mode numbers for an external uniform flow of Mach number -0.3. Only the first radial mode, among the incident ones, is present with a unit modal amplitude. Since the acoustic pressure varies over a large range, sound pressure level contours have been plotted.

Figures 26 through 31 show the sound pressure level contour plots with the nodal information obtained by the averaging technique. It is observed that the contour curves representing the main lobe of radiation in the conventional finite

81
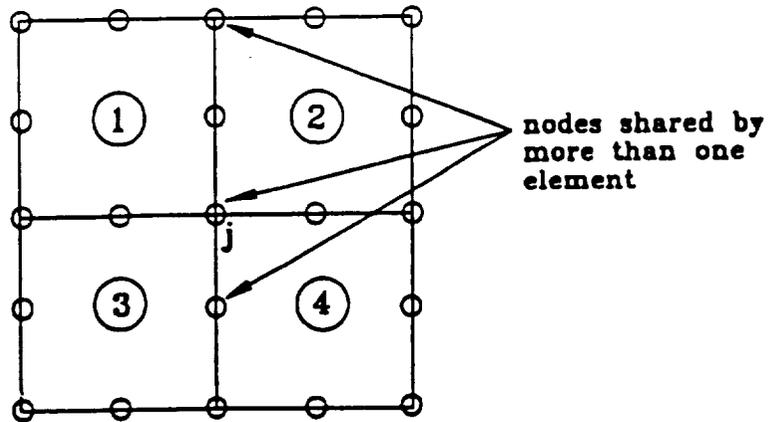
Figure 25: A node shared by all the elements in a 4 × 4 mesh

element region II are extremely jagged in nature and do not represent the true nature of the acoustic field there. But strangely enough, they smoothen out totally in the wave envelope region III. This is true for low frequencies like 12.0, which is on the lower side, and also for 20.0 which is on the higher side. Also it is noticed that this erroneous behavior is more spread out in the field at higher frequencies. Besides this, spurious reflections from the baffle are also present in the radiated field especially at high frequencies.

To improve on the results, nine noded quadratic isoparametric elements were used for the analysis instead of the eight noded ones. The presence of the extra ninth node at the element center did not provide better results. In fact, the results when compared with the eight noded ones were almost identical. Therefore, to reduce the dimensionality[9] of the problem, the nine noded elements were discarded. However the analysis is almost the same with both kinds of elements, except the

---

[9]The number of degrees of freedom associated with N eight noded elements in the mesh is less than N nine noded elements by N.

level	pressure (dB)
C	100.00
B	96.36
A	92.73
9	89.09
8	85.45
7	81.82
6	78.18
5	74.55
4	70.91
3	67.27
2	63.64
1	60.00

reference level 100dB is the maximum pressure in the domain
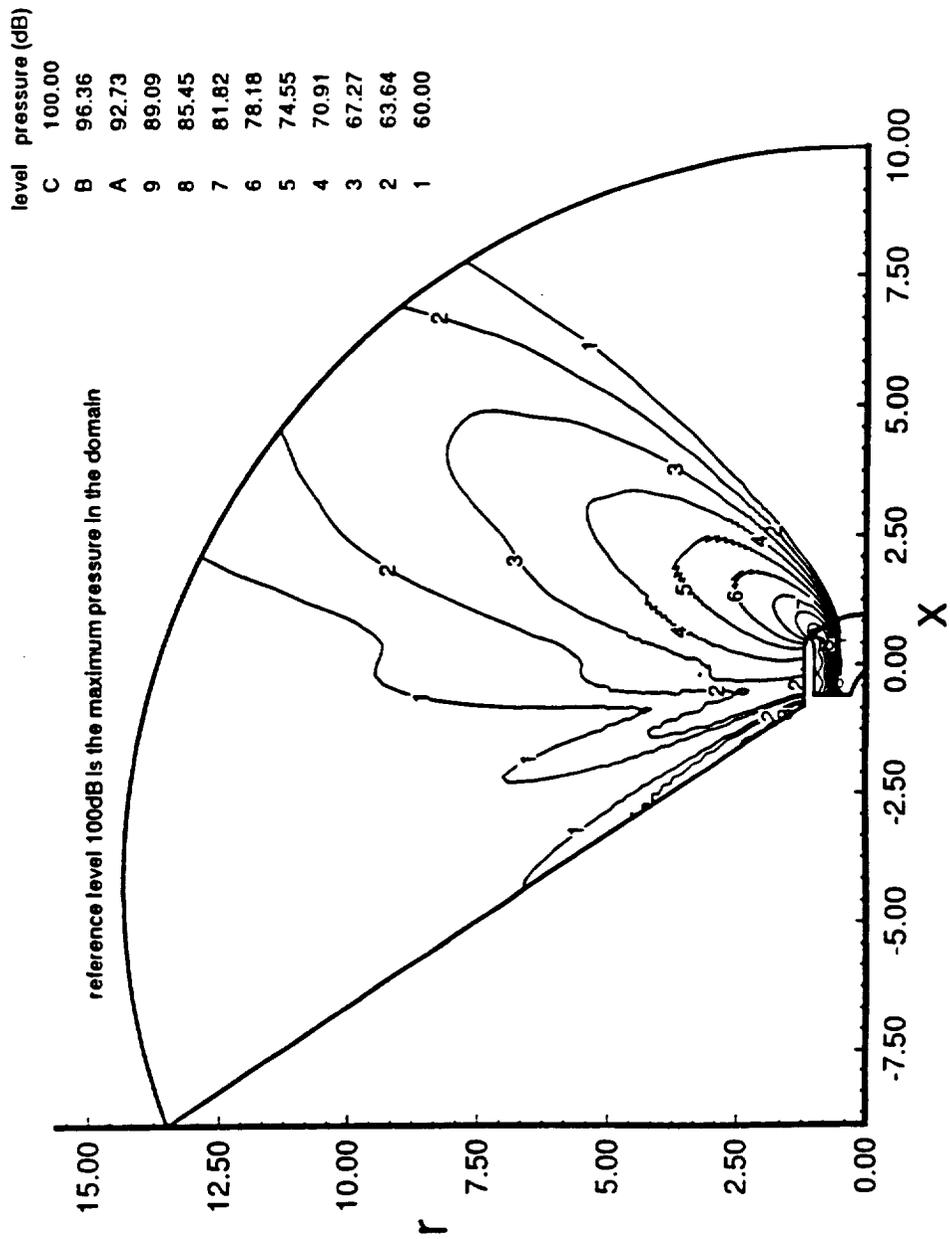
Figure 26: Sound pressure level contours in the whole domain from nodal data; $\eta_r = 12.0, m = 10$
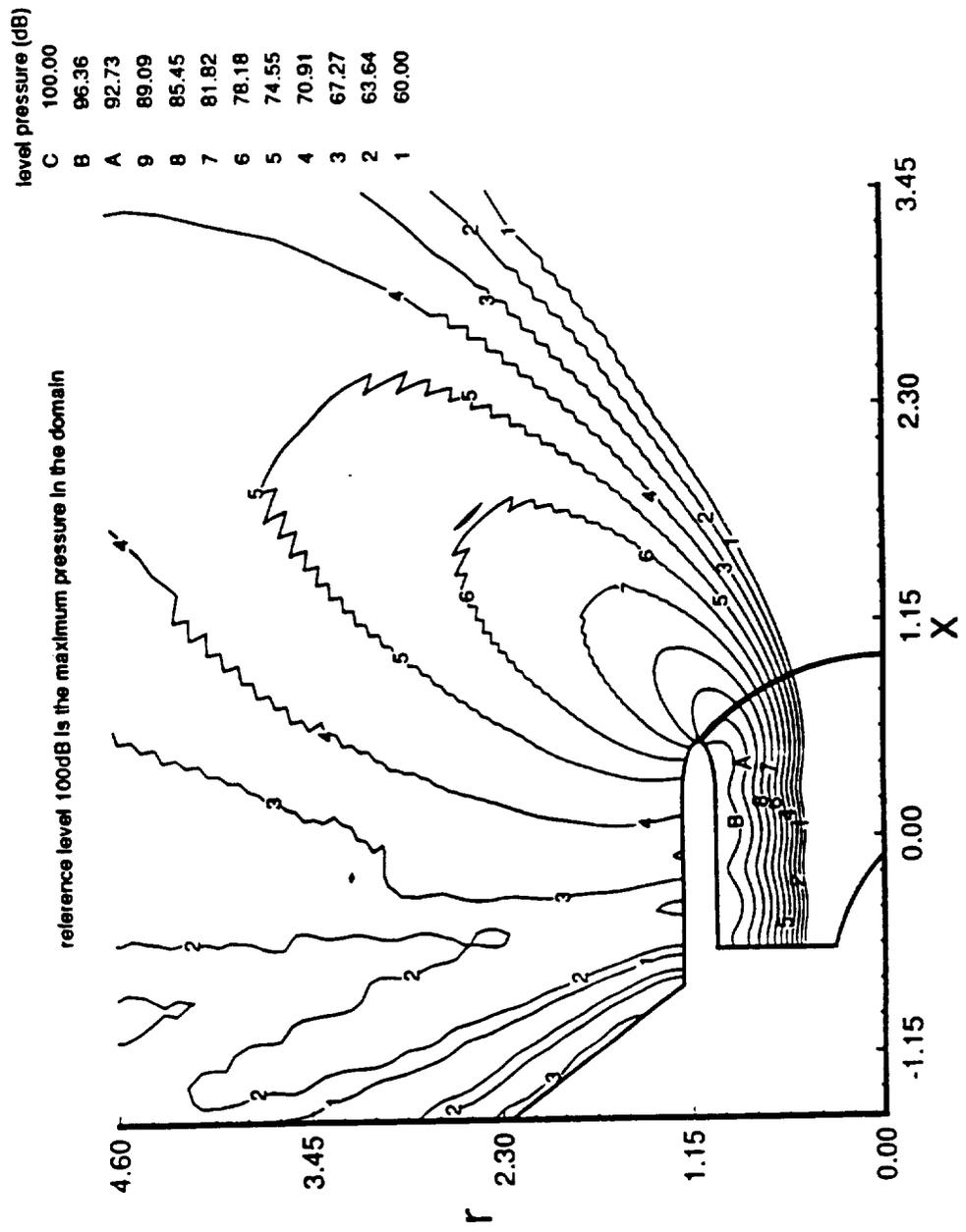
Figure 27: Sound pressure level contours inside the nacelle and in the near field from nodal data; $\eta_r = 12.0, m = 10$
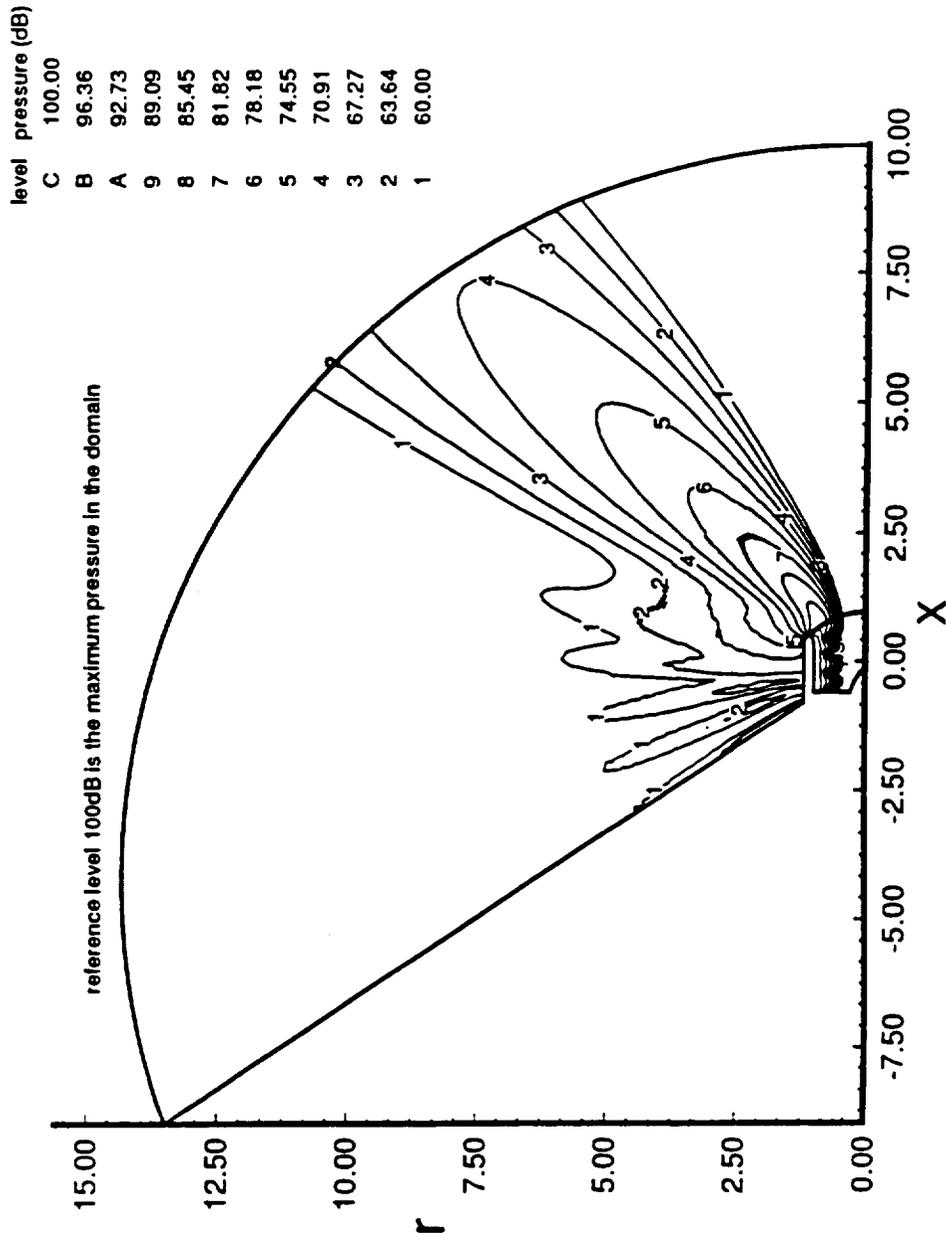
Figure 28: Sound pressure level contours in the whole domain from nodal data; $\eta_r = 15.0, m = 10$
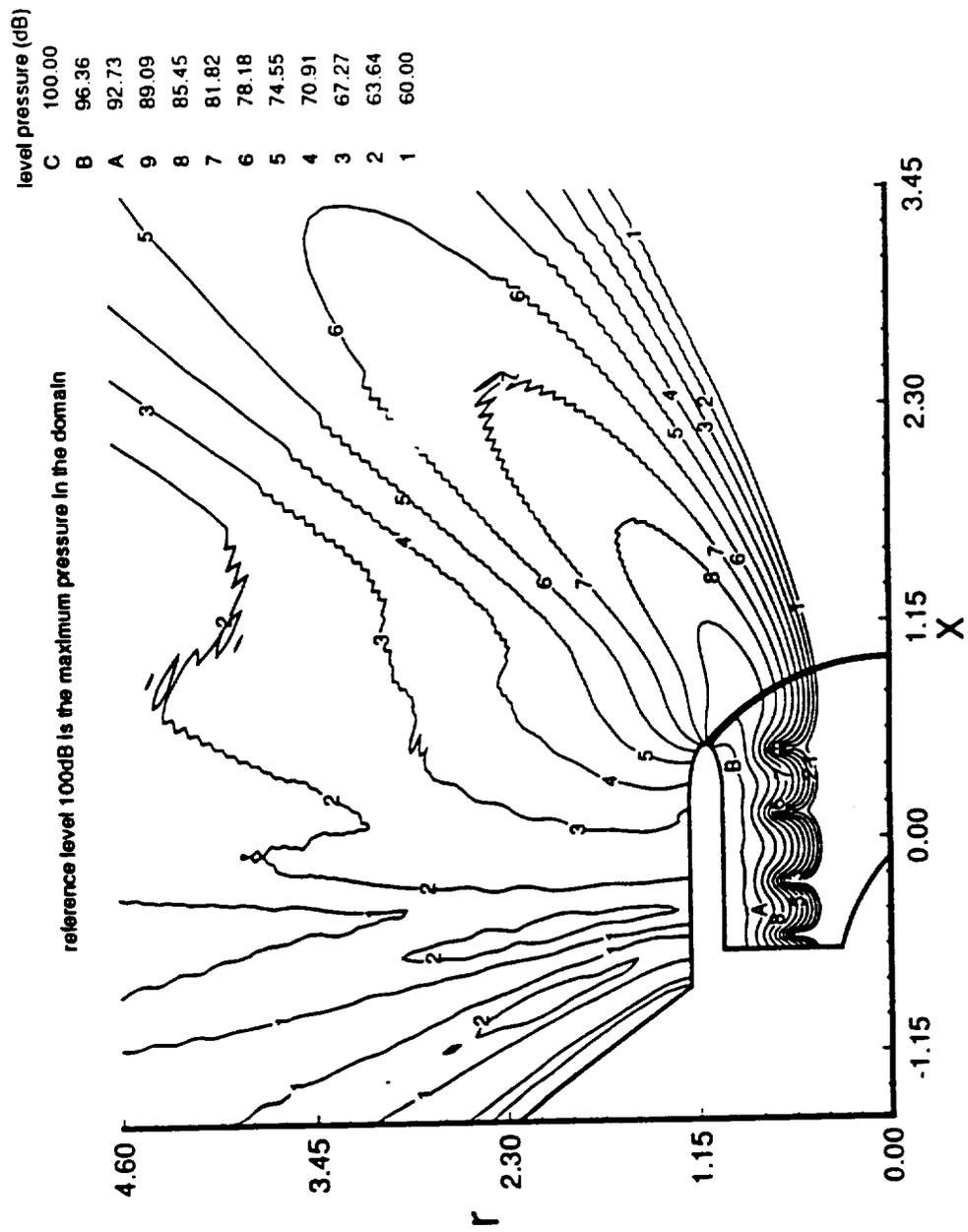
Figure 29: Sound pressure level contours inside the nacelle and in the near field from nodal data; $\eta_r = 15.0$, $m = 10$

86

level	pressure (dB)
C	135.00
B	131.82
A	128.64
9	125.46
8	122.27
7	119.09
6	115.91
5	112.73
4	109.54
3	106.36
2	103.18
1	100.00

reference level 100dB is the maximum pressure on far field boundary
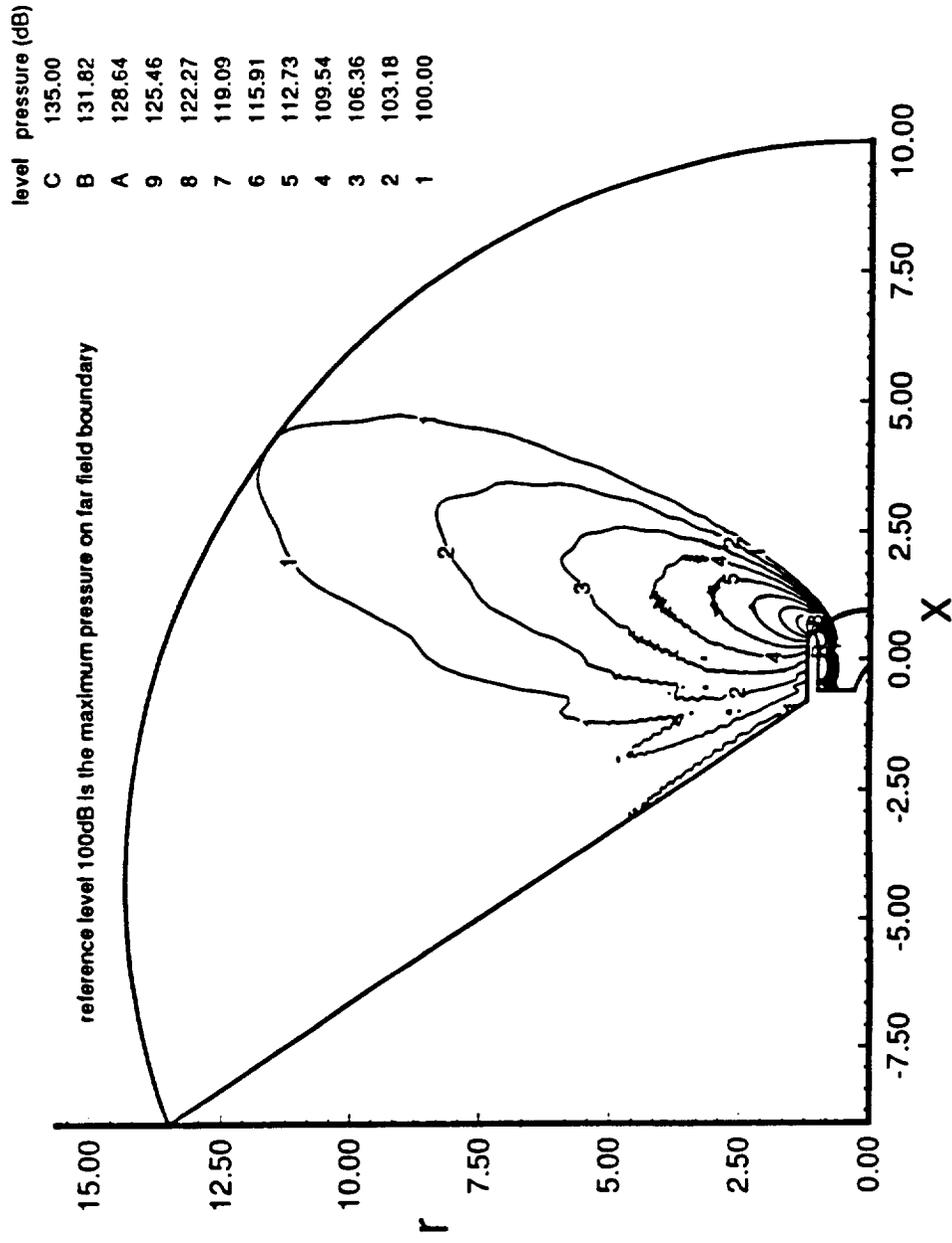
Figure 30: Sound pressure level contours in the whole domain from nodal data;
$\eta_r = 20.0, m = 20$
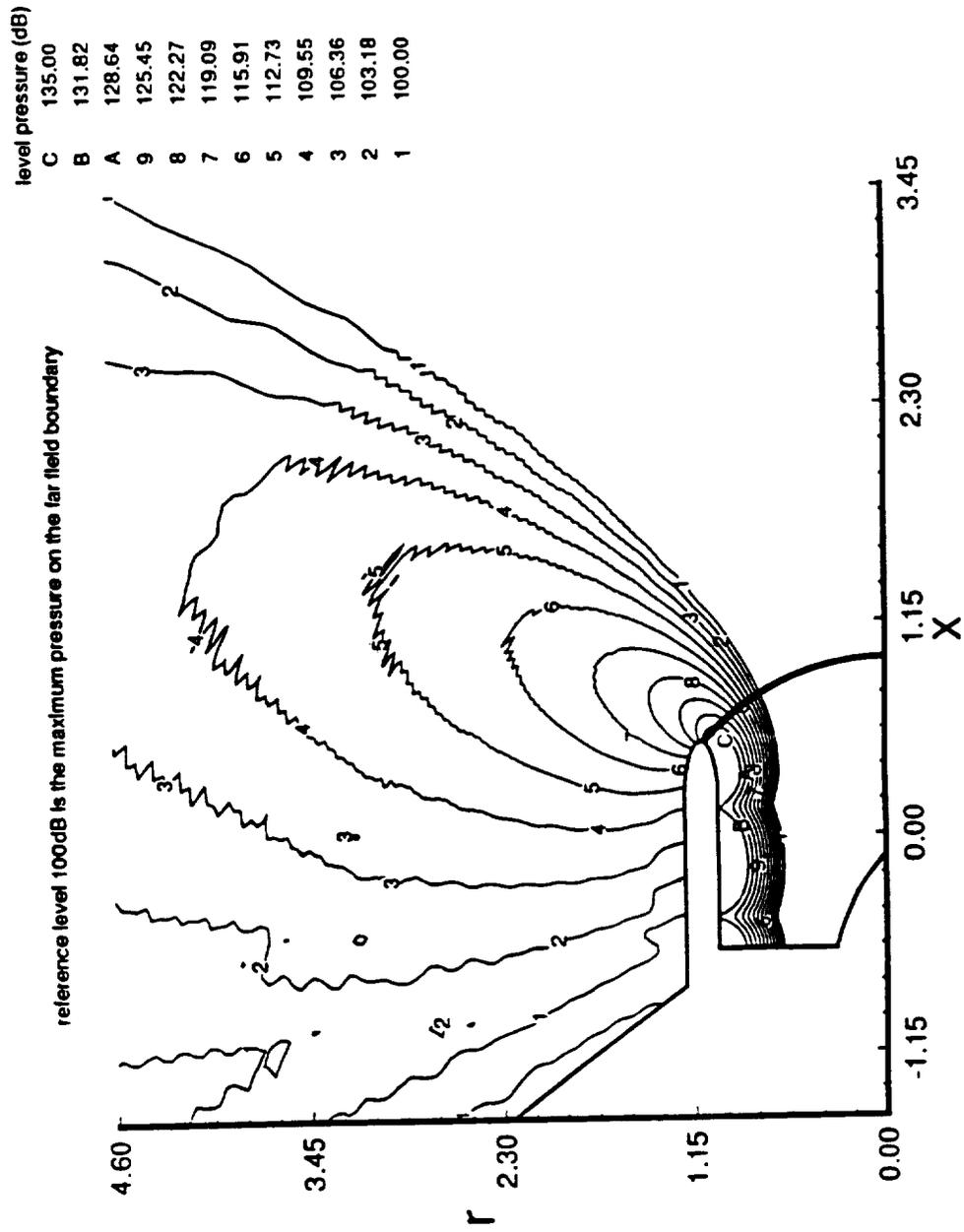
Figure 31: Sound pressure level contours inside the nacelle and in the near field from nodal data; $\eta_r = 20.0$, $m = 20$

the nodal connectivity and the coordinate array is generated in a different way while constructing the finite element mesh.
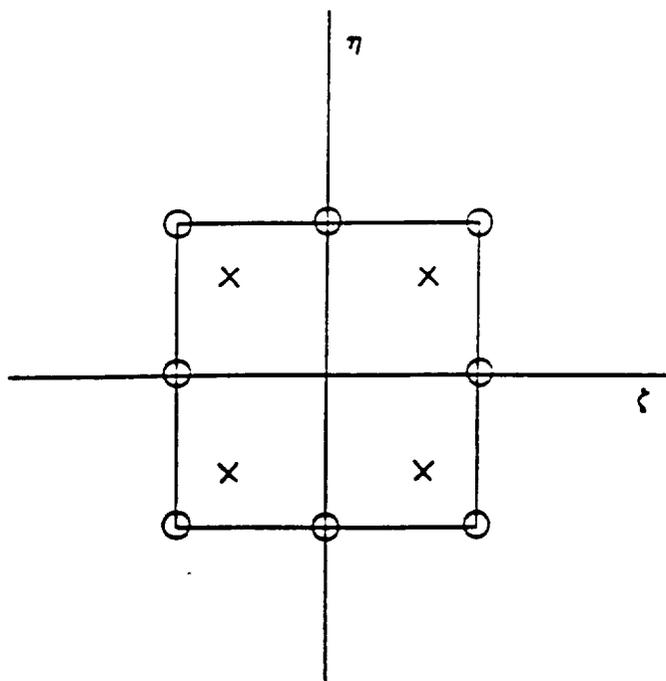
Figure 32: 2 × 2 grid of Gauss points in the parent element

For one dimensional line elements, it can be mathematically proved that the optimum points in the element for the derivative to be calculated are the ones corresponding to the standard Gaussian quadrature points in the parent element. Since these points are internal to an element, the derivatives of the solution calculated there are unique and continuous. Extending this feature to the two dimensional case, we seek to develop a scheme for calculating the acoustic pressure at the interior points of the elements corresponding to a standard 2 × 2 grid of Gauss points in the parent element (see Figure 32).

The nodal velocity potential solutions (both mean flow and acoustic) are interpolated at the Gauss points in an element using

$$\phi_o(x_g, y_g) = \sum_{i=1}^{n_e} \phi_{oi} N_i^e(x_g, y_g) \tag{133a}$$

$$\phi(x_g, y_g) = \sum_{i=1}^{n_e} \phi_i N_i^e(x_g, y_g) \qquad (133b)$$

where (x_g, y_g) are the coordinates of the map of the Gauss points[10] in the element. The derivatives of the potentials are then taken at the Gauss points by appropriately taking the derivatives of the element shape functions at the gauss points since

$$\frac{\partial \phi(x_g, y_g)}{\partial x} = \sum_{i=1}^{n_e} \phi_i \frac{\partial N_i^e(x_g, y_g)}{\partial x} \qquad (134a)$$

$$\frac{\partial \phi(x_g, y_g)}{\partial r} = \sum_{i=1}^{n_e} \phi_i \frac{\partial N_i^e(x_g, y_g)}{\partial r} \qquad (134b)$$

Once the velocity potentials (both mean flow and acoustic perturbation) and their derivatives have been calculated at the Gauss point grid inside the element, the acoustic pressure is evaluated there using equation (130). The sound pressure level contour plots from the data at the Gauss points give smoother curves and represent the acoustic radiated field much better. This is reflected in Figures 33 through 35 where the sound pressure level curves have been plotted for the same combinations of source frequencies and angular mode numbers as in Figures 26 through 31, but using the data at the Gauss points. Therefore the averaging technique for evaluating the nodal pressures as mentioned before seems to be quite inadequate for the acoustic radiation problem especially for higher frequencies. The proper and theoretically more rigorous way to obtain the nodal acoustic pressures is to obtain the pressures at the Gauss points and then interpolate the nodal values from them.

The next part of the study was aimed at investigating the effect of the geometric position of the transition circle C_1 in the mesh. If the transition circle is very far away from the inlet, then, at realistic frequencies which are usually the

---

[10]Gauss points are actually in the parent element. They are mapped onto corresponding points in the actual element.

level	pressure (dB)
C	100.00
B	96.36
A	92.73
9	89.09
8	85.45
7	81.82
6	78.18
5	74.55
4	70.91
3	67.27
2	63.64
1	60.00

reference level 100dB is the maximum pressure in the domain
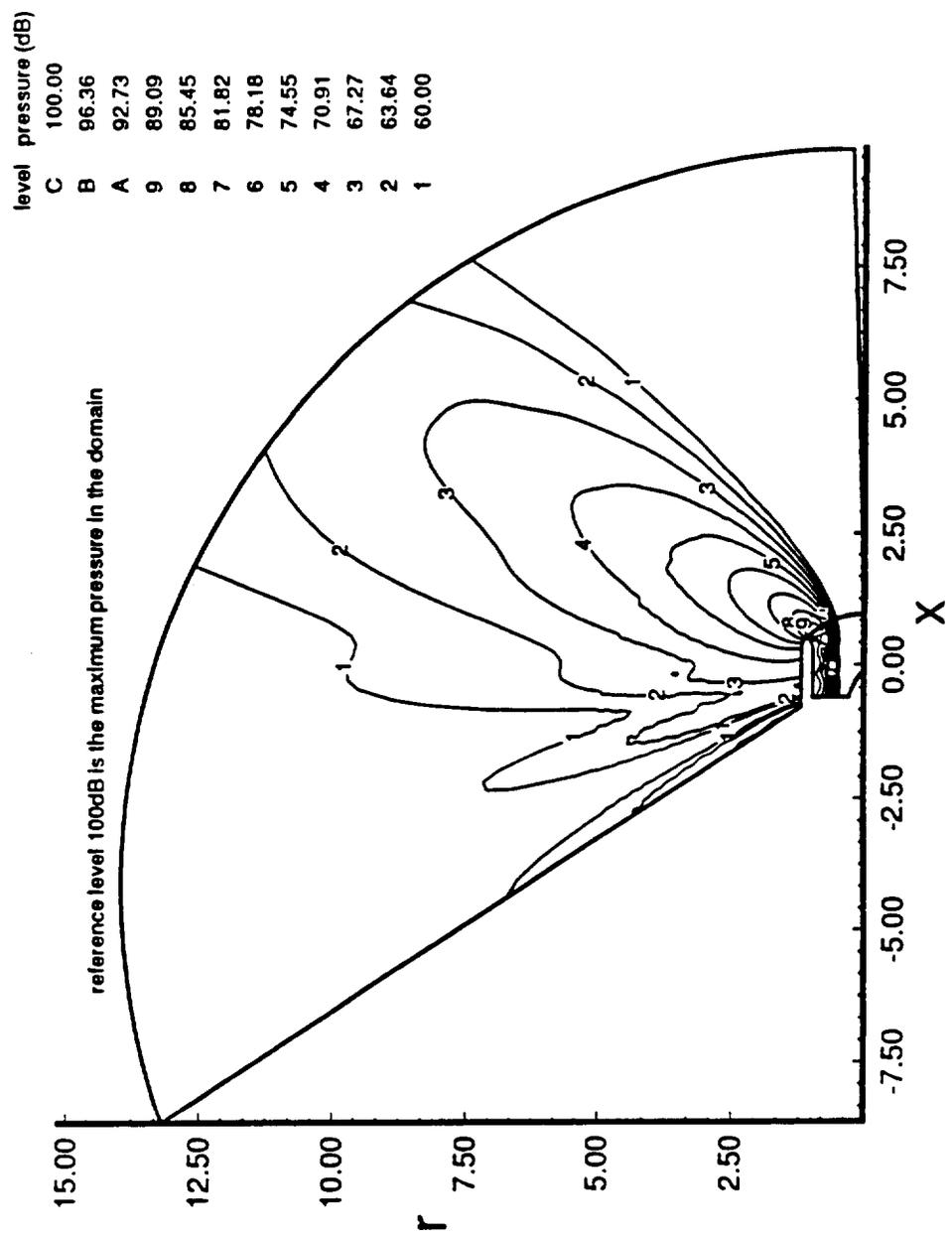
Figure 33: Sound pressure level contours in the whole domain from Gauss points; $\eta_r = 12.0, m = 10$
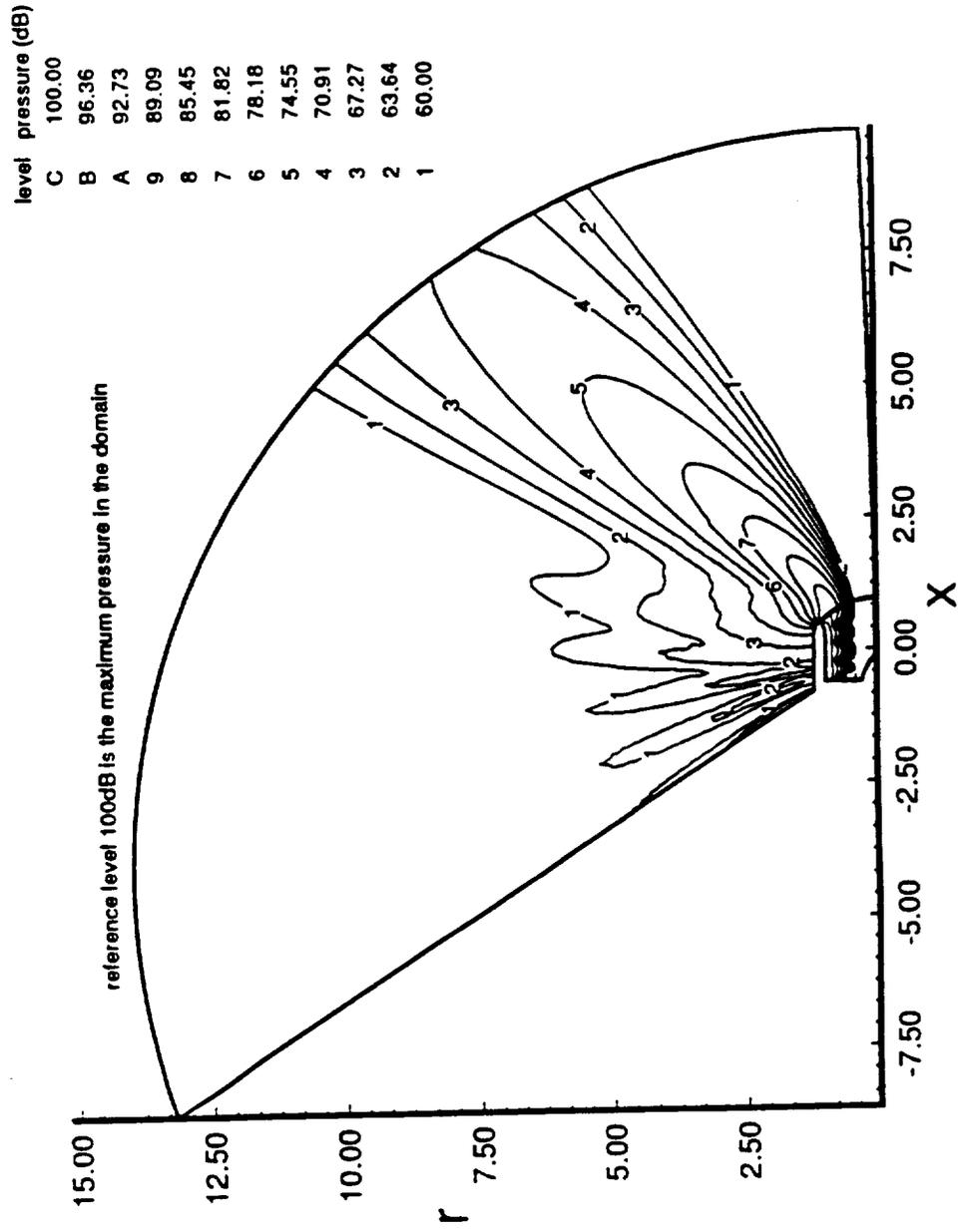
Figure 34: Sound pressure level contours in the whole domain from Gauss points; $\eta_r = 15.0, m = 10$
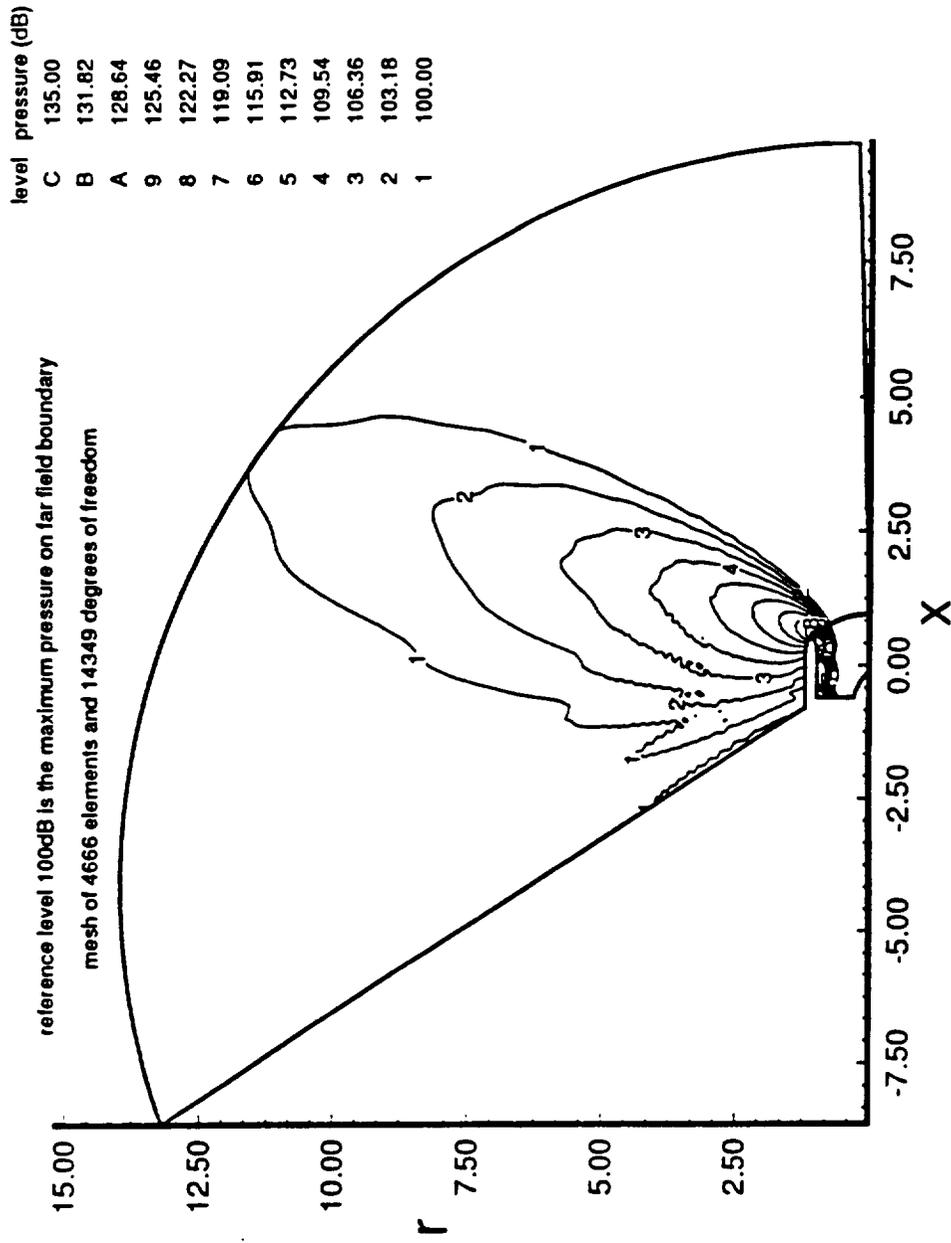
Figure 35: Sound pressure level contours in the whole domain from Gauss points; $\eta_r = 20.0, m = 20$; transition circle at 3.5 duct radius

higher ones, the number of conventional finite elements radially in region II has to be quite large to satisfy the number of elements per wavelength requirement. If the transition circle can be brought closer to the inlet the number of elements radially in region II needed to satisfy the number of elements per wavelength requirement will lessen. In such a case, the wave envelope region III becomes larger, but the number of wave envelope elements in that region does not have to increase proportionally because these elements have inverse decay and exponential terms in them to model the field due to a simple source. As the transition circle is brought closer to the inlet, the number of degrees of freedom associated with the problem drastically reduces, even at higher frequencies. Theoretically it cannot be brought very close to the inlet because the field there does not behave as one due to a harmonic acoustic monopole in uniform flow. Figures 26 through 35 show sound pressure level curves with the transition circle C_1 at 3.5 duct radius from the inlet. Figures 36 and 37 show sound pressure level contours at $\eta_r = 20.0$ and $m = 20$ with the transition circle at 2.5 duct radius and 1.5 duct radius, respectively, from the inlet. Comparing the results in Figures 35, 36 and 37 for $\eta_r = 20.0$ and $m = 20$, it is very surprising and also encouraging to observe that the the sound pressure level contours get smoother as the transition circle is brought closer to the inlet, even as close as 1.5 duct radius from the origin (the x-intercept of the transition circle is at a nondimensional distance of 1.5 from the origin). Furthermore, a drastic reduction in the number of degrees of freedom occurs. Figure 35 shows level curves obtained from a mesh of 4666 elements (14349 dof) while Figures 36 and 37 show the same level curves obtained from meshes having 3441 elements (10624 dof) and 2461 elements (7644 dof), respectively. As the transition circle is brought in closer to the inlet the level curves become significantly smoothen along with the tremendous reduction in the dimensionality of the problem. Even though the transition circle is close to the inlet, the curves have a smooth reflection free

transition from the conventional finite element region II to region III. We can infer from this that though the wave envelope elements are meant for modeling the far field, their shape functions which have the conventional finite element shape function expression in addition to the inverse decay and exponential terms, are also capable of modeling the moderately near field outside the inlet. As the transition circle is brought in closer, the angular resolution of the conventional finite element mesh in region II increases. This probably contributes partly to the improvement in results. However, in an attempt to reduce the dimensionality of the problem, it will be incorrect to apply the "ρc" termination (the Sommerfeld radiation boundary condition) at a boundary quite close to the inlet. Further investigation needs to be carried out to understand the phenomenon more clearly.

Referring to Section VI.B we notice that the acoustic boundary condition at the portion of the baffle C_b belonging to region II is not properly applied with the hope that the errors due to it will be localized. But we observe that especially at higher frequencies and higher angular mode numbers a significant level of sound is radiated around the lip of the nacelle towards the baffle. The portion of the baffle in region II does not act as a reflection free boundary and therefore creates incorrect standing wave patterns near the baffle. Spurious reflections from the baffle in region II are also observed at lower frequencies, but the intensity is much less. As the transition circle C_1 is brought closer to the inlet, the part of the baffle belonging to region II becomes less and therefore the spurious reflections reduce significantly in intensity because the part of the baffle belonging to region III is reflection free. The reduction in dimensionality of the problem as well as improvement in results as the transition circle is brought closer to the inlet are significant results of this study.
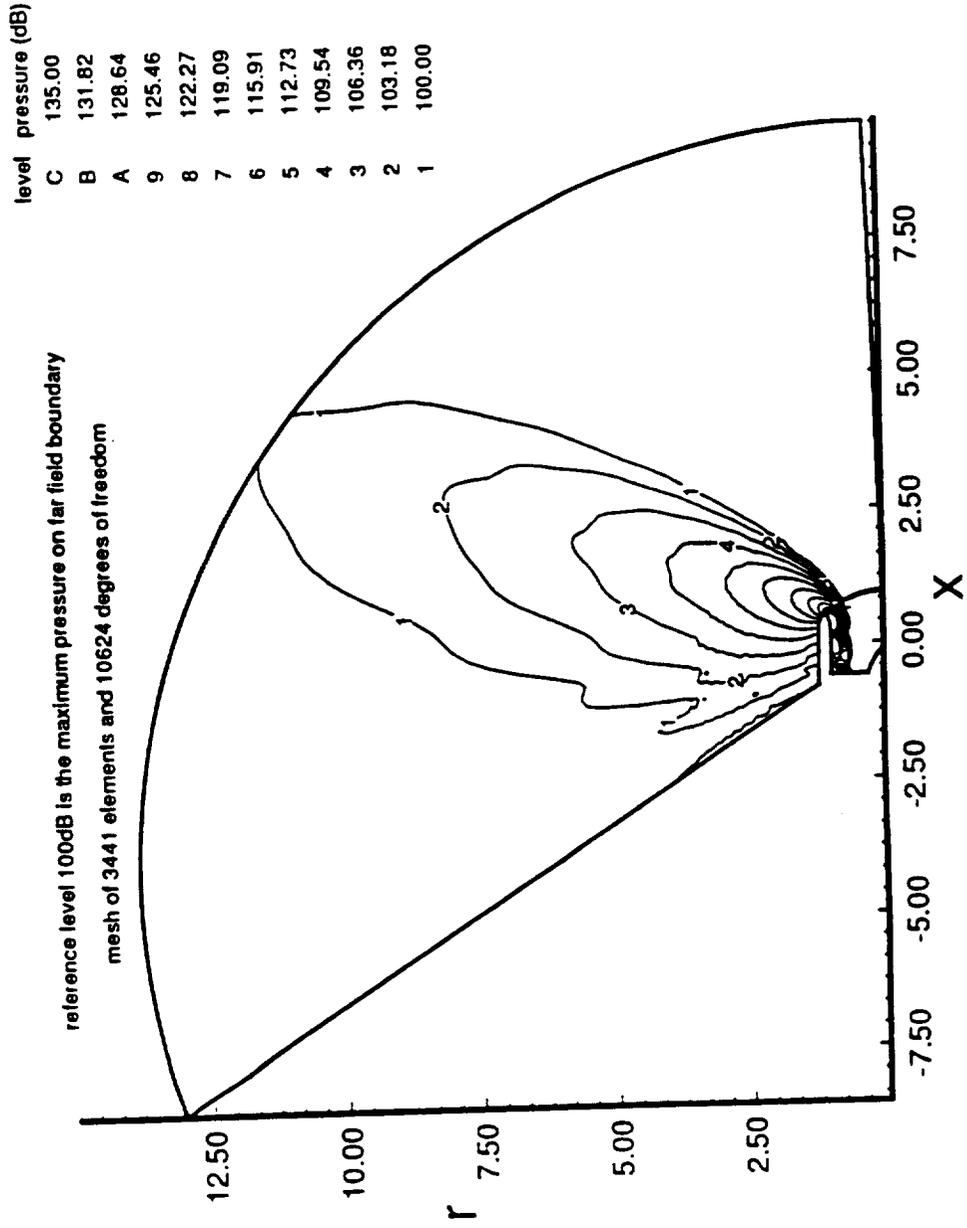
Figure 36: Sound pressure level contours in the whole domain from Gauss points; $\eta_r = 20.0, m = 20$; transition circle at 2.5 duct radius
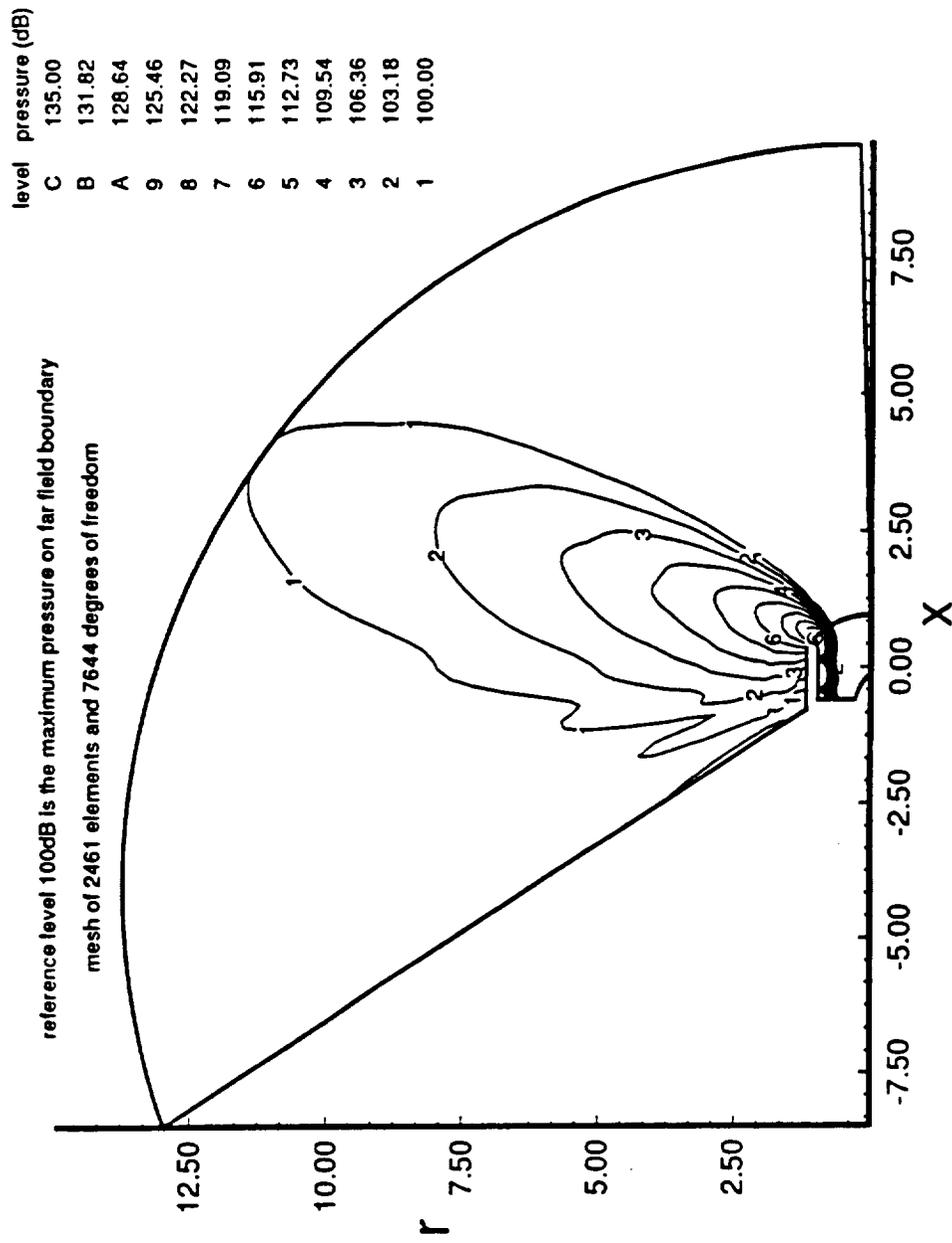
Figure 37: Sound pressure level contours in the whole domain from Gauss points; $\eta_r = 20.0, m = 20$; transition circle at 1.5 duct radius

VII. CONCLUSIONS

Several improvements to the finite element modeling of acoustic radiation from turbofan engine inlets have been presented. They are enumerated below:

• The finite element mesh has been improved in search of an improved solution. In particular, the aspect ratios of the conventional finite elements in the moderately near field (region II) have been maintained, especially in the main direction of sound propagation. The number of conventional finite element regions outside the nacelle was reduced to one thereby eliminating superfluous coding and also obtaining some reduction in the total number of degrees of freedom in the mesh.

• The time invariant mean flow problem has been reformulated with new boundary conditions and a proper solution technique has been incorporated.

• A finite element duct eigenvalue problem has been solved on the fan face mesh and the resulting modal matrix and the eigenvalues have been used to incorporate a source boundary condition on the fan face in the acoustic radiation problem.

• The acoustic velocity potential at the sound source has been modeled as a combination of the positive and negative propagating duct modes evaluated by the finite element duct eigenvalue problem. By employing this, a finite element formulation of the boundary integral on the fan face has been obtained.

• In the post processing of the solution, the acoustic pressure was observed to be discontinuous across inter-element boundaries. The technique of averaging the pressures at a node, calculated from each element sharing that node, was found to give poor results especially at higher frequencies. An improved way of evaluating the acoustic pressure at the Gaussian quadrature points inside the elements and then interpolating it to the nodes has significantly improved the results.

• The geometric position of the transition circle bordering the conventional finite element region and the wave envelope region was seen to be creating a significant effect on the results. It was found out that the wave envelope elements were not only capable of modeling the far field but also the moderately near field outside the nacelle. Therefore, the transition circle could be brought in much closer to the inlet than thought before, and this has lead to better results with a drastic reduction in the number of degrees of freedom. This is probably the most significant result of this study.

These contributions have been implemented in computer programs which are capable of predicting the radiation pattern at frequencies which are comparable to those of actual turbofan engines. With the current version of the computer programs it is possible to accomodate 21000 degrees of freedom which would predict the radiation pattern fairly well at quite high frequencies (for example, $\eta_r = 35$) provided the transition boundary circle is not very far away from the inlet. Future work should aim at imposing a proper and accurate boundary condition on the baffle in the conventional finite element region II in order to make it reflection free. The phenomenon of improvement in the results as the transition circle is brought closer to the inlet should be investigated in more detail. The representation of the sound source in terms of the duct mode amplitudes may not be the best way to model it. Alternative ways should be investigated and the results should be compared with experimental data to see which model works best.

APPENDIX A

USER'S MANUAL

A. DATA DESCRIPTION OF THE MESH GENERATION CODE

1. **Input data**   The finite element mesh generation code $PRATMESH$ not only generates the finite element mesh for the problem but also solves the duct eigenvalue problem on the fan face mesh. Therefore the input data descriptions for these two steps are included together. The program is dimensioned for working with a maximum of 5000 eight node quadratic isoparametric elements, 21000 nodes, 150 boundary line elements on the combination of upper and lower surface of the nacelle, 50 boundary line elements on the fan face and 125 boundary line elements on the far field boundary. The input data file structure has distinct blocks of input data referred to as cards. Each card begins on a new line and the input data on the card is formatted. The record length is of a maximum of 80 characters. If the data format requires more than 80 characters a card is continued on additional lines. The input variables should be input in the file in the sequence given.

Card	Variable	Format	Description
1	NLINU	I5	Number of three-node line elements to describe the upper surface of the nacelle
	NLINI	I5	Number of three-node line elements to describe the lower surface of the nacelle
	NY	I5	Number of elements along the duct radius in region I, which is equal to the number of three-node line elements on the fan face. The fan face is the plane $x =$ constant, at which the input duct modal amplitudes are specified.

100

Card	Variable	Format	Description
1	NX2	I5	Number of elements radially in region II
	NWEEL	I5	Number of wave envelope layers
	NPRINT	I5	= 0, do not write nodal coordinate array = 1, write nodal coordinate array
	NDONT	I5	= 0, do not write output data file = 1, write output data file
	NCNTR	I5	= 0, there is no centerbody = 1, there is a centerbody
	NCNTR1	I5	Sequence number of the first line element on the centerbody. It is the first element from the intersection of the centerbody and the fan face.
	NCNTR2	I5	Sequence number of the last line element on the centerbody. It is the element at the intersection of the centerbody and the x-axis.
2	PCNT(I)	6F10.0	I = 1, NY; end node locations of the three-node line elements lying along the fan face. The node locations are given as fractions of the fan face width and starting from the intersection of the fan face and the lower surface of the nacelle. The first node therefore has a zero fractional distance and is not an input. If there are 5 line elements along the fan face then a typical input for this array would be 0.2, 0.4, 0.65, 0.88, 1.00

Card	Variable	Format	Description
3	ADSHPU(I, J, K)	6F10.0	I = 1, NLINU; J = 1, 3; K =1, 2 nodal coordinates of the three-node line elements defining the upper surface of the nacelle. I is the element number, J is the local node number, K = 1 defines x coordinate value and K = 2 defines r coordinate value. The elements are sequenced from the baffle surface to the to the tip of the nacelle. Each card has the nodal coordinate information of one line element. Therefore, the number of records for this card will be the number of line elements along the upper surface of the nacelle
4	ADSHPI(I, J, K)	6F10.0	I = 1, NLINI; J = 1, 3; K =1, 2 nodal coordinates of the three-node line elements defining the lower surface of the nacelle. I is the element number, J is the local node number, K = 1 defines x coordinate value and K = 2 defines r coordinate value. The elements are sequenced from the fan face to the tip of the nacelle. The number of cards will be the number of line elements along the lower surface of the nacelle
5	CBSHPI(I, J, K)	6F10.0	I = 1, NLINI; J = 1, 3; K =1, 2 nodal coordinates of the three-node line elements defining the center-body and the centerline of the computational domain. The array is similar to that in cards 3 and 4 and so also is the format. The elements are sequenced from the fan face to the intersection of the highlight circle with the x-axis.

Card	Variable	Format	Description
6	R2	F10.0	x-intercept of the outer bounding circle C_1 of region II in multiples of the inlet duct radius
7	RLAYER(I)	6F10.0	I = 1, NWEEL x-intercepts of the outer bounding circles of the wave envelope layers in multiples of the inlet duct radius
8	MT	I5	Angular mode number
	NPOS	I5	Number of positive modes retained in the modal matrix
	VMACH	F10.5	Freestream flow Mach number outside the nacelle (positive directed towards the inlet)

2. Output data   *PRATMESH* has two output data files - unit 6 and 20. Data
file 6 is the printed output data file by default and is well documented in itself.
Therefore, it is not described here.The output data file 20 contains all the infor-
mation about the finite element mesh and serves as an input to the finite element
calculations in subsequent codes. The output data file structure, like input file unit
5, has records which are classified under the heading of different cards because of
the varied nature of input parameters. Each card begins on a new line and the
input data is formatted. The record length is of a maximum of 80 characters.

Card	Variable	Format	Description
1	NE	I10	Number of elements in the domain
	NL1	I10	Number of three-node line elements to describe the surface of the nacelle
	NL2	I10	Number of elements in region I along the duct radius
	NL3	I10	Number of elements in region II or region III in the angular direction
	NNX1	I10	Number of nodes along x-axis in region I
	NNX2	I10	Number of nodes radially in region II
	NNTH1	I10	Number of nodes in region I along the duct radius
2	NNTH2	I10	Number of nodes in region II in the angular direction
	NNODE	I10	Number of nodes in the domain
	NWEEL	I10	Number of wave envelope layers

Card	Variable	Format	Description
2	NX1	I10	Number of elements along x-axis in region I
	NX2	I10	Number of elements in region II along the radial direction
	NY	I10	Number of three-node line elements along the fan face
3	NY2A	I10	Number of three-node line elements along the upper surface of the nacelle
	NY2	I10	Number of elements in region II in the angular direction
	NY3	I10	Number of elements in region III in the angular direction
	NCNTR	I10	1 or 0 value deciding the presence or absence of the centerbody
4	NCNTR1	I10	Sequence number of the first centerbody element
	NCNTR2	I10	Sequence number of the last centerbody element
	NLC	I10	Number of centerbody elements

Card	Variable	Format	Description
5	R2	D15.8	x intercept of the outer bounding circle C_1 of region II
6	RLAYER(I)	4D15.8	x-intercept of the outer bounding circles of the wave envelope layers
7	AN(I, J)	7I10	Nodal connectivity array for the elements I = element number, J = local node number
8	NETYPE(I)	7I10	I = 1, NE identification number of elements
9	AD(I, J, K)	4D15.8	nodal coordinate/topology array of the elements I = Element number, J = local node number, K = x or r coordinte specifier
10	ANL1(I, J)	7I10	Nodal connectivity array for the boundary line elements along the nacelle surface I = line element number, J = local node number
11	ANL2(I, J)	7I10	Nodal connectivity array for the boundary line elements along the fan face I = line element number, J = local node number
12	ANL3(I, J)	7I10	Nodal connectivity array for the boundary line elements along the outer bounding circle C_∞ of the domain I = line element number, J = local node number

Card	Variable	Format	Description
13	ANLC(I, J)	7I10	Nodal connectivity array for the boundary line elements along the centerbody I = line element number, J = local node number
14	ADL1(I, J, K)	4D15.8	Nodal coordinate array of the boundary elements along the nacelle surface I = element number, J = local node number, K = x or r coordinate specifier
15	ADL2(I, J, K)	4D15.8	Nodal coordinate array of the boundary elements along fan face I = element number, J = local node number, K = x or r coordinate specifier
16	ADL3(I, J, K)	4D15.8	Nodal coordinate array of the boundary elements along C_∞ I = element number, J = local node number, K = x or r coordinate specifier
17	ADLC(I, J, K)	4D15.8	Nodal coordinate array of the boundary elements along centerbody I = element number, J = local node number, K = x or r coordinate specifier
18	PCNT(I)	4D15.8	I = 1, NNTH1; fractions in which the fan face has been divided for input nodes (see input data description)
19	MT	I10	Angular mode number

Card	Variable	Format	Description
19	NPOS	I10	Number of positive modes retained in the modal matrix
	NNEG	I10	Number of negative modes retained in the modal matrix
	NVECT	I10	Total number of positive and negative modes retained in the modal matrix
20	VMACH	D15.8	Freestream flow Mach number outside the nacelle (positive directed towards the inlet)
21	DD(I, J)	4D15.8	I = 1, NNTH1; J = 1, NVECT Truncated modal matrix from the finite element duct eigenvalue problem
22	VKAP(I)	4D15.8	I = 1, NPOS Transverse eigenvalues of the annular duct

B. DATA DESCRIPTION OF THE MEAN FLOW CODE

1. Input data   The time invariant mean flow problem on the finite element mesh is solved in the $PRATFLOW$ code. The mesh information in the output file unit 20 from the $PRATMESH$ program serves as an input to the $PRATFLOW$ code. The user input for this program is the data file unit 5. It has only one card and the input data is formatted. The record is a maximum of 80 characters. The input variables should be input in the file 5 in the sequence as described.

Card	Variable	Format	Description
1	NTYPE	I5	= 1, calculates the mean flow velocity potential only for flow from infinity into the blank inlet = 2, calculates the velocity potential for inlet flow alone = 3, calculates both cases sequentially and writes the solution vector to disk for use by the superposition program
	PRINT1	I5	≠ 0, beginning row and column of the assembled stiffness matrix to be printed = 0, do not print
	PRINT2	I5	≠ 0, final row and column of the assembled stiffness matrix to be printed = 0, do not print
	NPLOT	I5	= 0, contour plotting routine bypassed matrix to be printed = 1, plot contour level curves for the solution vector
	NPRINT	I5	= 0, do not print nodal coordinate array = 1, print nodal coordinate array

2. **Output data**   The output data files from the *PRATFLOW* code are files - unit 6 and 21. File 6 is well documented in itself and is not described here. File 21 contains the nodal mean flow velocity potential of problems II and I in that order. It serves as an input to the *PRATVEL* program. In addition to the saved files 6 and 21, seven unformatted scratch files - units 1, 2, 4, 8, 15, 16 and 17 are used. Files 15, 16, 17 are direct access and files 1, 2, 4, 8 are sequential access. Record

lengths for the direct access files 15, 16, and 17 are 36, 144 and 36 respectively. The number of records in each direct access file is the number of elements in the domain.

C. DATA DESCRIPTION OF THE VELOCITY POTENTIAL SUPERPOSITION CODE

1. Input data   Problems I, II and III of the time invariant mean flow problem are superposed in the $PRATVEL$ program to obtain the mean flow velocity potential at the nodes. Subsequent calculations to obtain the nodal mean flow velocity is also carried out in this code. The finite element mesh information in the output file unit 20 from the $PRATMESH$ program serves as an input to the $PRATVEL$ code. The output data file unit 21 from the $PRATFLOW$ code is another source of input. It contains the nodal values of the velocity potential of problems II and I of mean flow in that order. The user input for the $PRATVEL$ code is data file unit 5 which has only one card and the data is formatted. The input variables should be input in file 5 in the sequence described.

Card	Variable	Format	Description
1	VMIN	F10.0	Average compressible inlet Mach number at fan face (positive directed towards inlet) based on local speed of sound
	CFS	F10.0	Free stream speed of sound, outside the nacelle
	RHOFS	F10.0	Free stream density of air, outside the nacelle

2. Output data   The output data files for the superposition program are files unit 6 and 22. Data file 6 is well documented in itself and hence is not described here. File 22 serves as an input data file for the acoustic radiation program. It contains some flow parameter values and the nodal values of the mean flow velocity. The output data description in file 22 is given below. Each card of data begins on a new line.

Card	Variable	Format	Description
1	VMIN	D15.8	Average compressible inlet Mach number at fan face (positive directed towards inlet) based on local speed of sound
	CFS	D15.8	Free stream speed of sound outside the nacelle
	RHOFS	D15.8	Free stream density of air outside the nacelle
	CSTAG	D15.8	Stagnation speed of sound
2	RHOSTG	D15.8	Stagnation density
	TZERO	D15.8	Stagnation temperature
	CF	D15.8	Speed of sound at fan face
	RHOF	D15.8	Density at fan face

Card	Variable	Format	Description
3	VOCFS(I, J)	4D15.8	I = 1, 2, J = Local node number Nodal mean flow velocity values, I = 1 defines x-velocity and I = 2 defines r-velocity
4	ZVX(I)	2D15.8	I = Global node number Nodal mean flow x-component velocity values
	ZVR(I)	2D15.8	I = Global node number Nodal mean flow r-component velocity values

D. DATA DESCRIPTION OF THE ACOUSTIC RADIATION CODE

1. **Input data**   There are two different versions of the acoustic radiation program - $PRATRADA$ and $PRATRADB$. $PRATRADA$ is the version where the nodal acoustic pressure has been evaluated by an averaging technique while $PRATRADB$ is the version where the acoustic pressure has been evaluated at the Gauss points and not at the nodal points. Therefore the postprocessors of the two versions are different but the finite element calculations are the same. The input data files for the acoustic radiation program $PRATRADA$ and $PRATRADB$ are files unit 5, 20 and 22. Data file 20 is the output of $PRATMESH$ and contains the finite element mesh information. File 22 is the output of $PRATVEL$ described before. The user input is in data file 5. The input data has been structured into cards. Each card of data begins on a new line and the input data is formatted. The acoustic radiation program is capable for running multiple cases. It contains the data for all the cases with an alphanumeric input separating the data for any two cases which determines whether the case is to be run or not.

Card	Variable	Format	Description
1	HDR(I)	14A4	I = 1, 14 Character*4; it is the control for multiple cases; if HDR(1) = 'stop' the program stops execution and hence it is at the beginning of the data for each case
2	NSYM	I10	= 0, rectangular duct = 1, circular or annular duct
	ETAR	F10.5	Nondimensional frequency of the sound source $(\eta_r = \omega R/c_r)$ ω = fan rotational speed in rad/sec R = reference duct radius at the fan face c_r = freestream speed of sound outside the nacelle
3	PRINT1	I5	$\neq 0$, Beginning row and column in stiffness matrices printed = 0, Beginning row and column in stiffness matrices not printed
	PRINT2	I5	$\neq 0$, Final row and column in stiffness matrices printed = 0, Final row and column in stiffness matrices not printed
	NPLOT	I5	> 0, level curves for the solution vector plotted = 0, plotting routine bypassed
	NCONT	I5	Number of level curves to be plotted

Card	Variable	Format	Description
3	CMAXO	F10.5	Value of maximum level curve
	CMINO	F10.5	Value of minimum level curve
4	ZAI(I)	6F10.5	I = 1, NPOS; complex incident modal amplitudes, real and imaginary parts
5	NLINED	I5	Number of acoustically lined elements on the inner surface of nacelle (if NLINED = 0, there is no lining and lining impedances are not required)
	MBEGIN	I5	Element number (counted from fan face along the inner nacelle surface) on which the lining begins
6	ZADM(I)	6F10.5	I = 1, NLINED; admittances in the elements on the nacelle inner surface (complex values), real and imaginary parts

2. Output data   The output file for the acoustic radiation codes $PRATRADA$ and $PRATRADB$ is the file unit 6 which is well documented in itself and therefore is not described here. In addition to the saved files, seven unformatted scratch files - units 1, 2, 3, 4, 15, 16 and 17 are used. Files 15, 16, 17 are direct access and files 1, 2, 3, 4 are sequential access. Record lengths for the direct access files 15, 16, and 17 are 36, 144 and 36 respectively. The number of records in each direct access file is the number of elements in the domain. In $PRATRADB$, the data for the acoustic pressure evaluated at the Gaussian quadrature points inside the elements has been written to file 6. The user may write it to a separate file

114

if he/she wishes to. It may then be used by some convenient plotting package like *TECPLOT* to plot the sound pressure levels in the domain. The acoustic pressure data at the Gauss points is written down element by element. In each element there are four Gauss points. Therefore, the number of records for the acoustic pressure data is four times the total number of elements in the domain. The description of the acoustic pressure data evaluated at Gauss points follows.

Card	Variable	Format	Description
1	XG(I, J, K)	1X,E14.7	I = element number; J, K = 1, 2; (J, K) refers to a particular Gauss point in the 2 × 2 grid; x coordinate of the Gauss point
	RG(I, J, K)	2X,E14.7	I = element number; J, K = 1, 2; (J, K) refers to a particular Gauss point in the 2 × 2 grid; r coordinate of the Gauss point
	PGAU(I, J, K)	2X,E14.7	I = element number; J, K = 1, 2; (J, K) refers to a particular Gauss point in the 2 × 2 grid; acoustic pressure at the Gauss point

E. DATA DESCRIPTION OF THE CUBIC SPLINE INTERPOLATION PROGRAM

1. Input data   This program is for generating the input data for nacelle and centerbody geometry. The nacelle and centerbody geometry is generated by a spline curve fit procedure using x and r coordinates of enough points to define the shape of the outer nacelle, the inner nacelle, and the center body. Using the spline information, the surfaces of the nacelle are discretized into line elements whose end points are defined. The center node of the elements is created from

the knowledge of the end points. The curve fit is a natural cubic spline. The cubic spline interpolation program prepares the input data for the mesh generation program *PRATMESH*. Details of the scheme have been described in section III. The input data is of free format. Each card of data begins on a new line.

Card	Variable	Description
1	NELU	Number of line elements describing the upper surface of the nacelle; the number of this parameter is one less than the number of points being input to represent the surface (see FRACTU(I))
	NELC1	Number of line elements describing the centerbody between fan face and centerbody tip; the number of this parameter is one less than the number of points being input to represent the surface (see FRAC1(I))
	NELC2	Number of line elements describing the centerline between centerbody tip and intersection of highlight circle with x-axis; the number of this parameter is one less than the number of points being input to represent the surface (see FRAC2(I))
2	XBAF	x-coordinate of the intersection of the baffle with the upper surface of the nacelle
	XTIP	x-coordinate of the nacelle tip
	YTIP	r-coordinate of the nacelle tip
	XFAN	x-coordinate of the fan face

Card	Variable	Description
2	XCB	x-coordinate of the centerbody tip
3	FRACTU(I)	I = 1, NELU + 1; Fractional distance of the end nodes of the line elements on the upper nacelle surface sequenced from baffle surface onwards (fraction based on the entire length of the upper nacelle surface)
4	FRAC1(I)	I = 1, NELC1 + 1; Fractional distance of the end nodes of the line elements on the centerbody sequenced from fan face onwards (fraction based on the entire length of the centerbody)
5	FRAC2(I)	I = 1, NELC2 + 1; Fractional distance of the end nodes of the line elements on the centerline sequenced from the centerbody tip to the highlight circle (fraction is based on this distance along the centerline)

2. Output data   The output of this program are the variables ADSHPU(I, J, K), ADSHPI(I, J, K), CBSHPI(I, J, K) (see input data description of *MESHGEN*) written onto output file unit 7 with the same format as the corresponding data in input file 5 of *MESHGEN*. In a typical application, the spline program output file is imported into data file 5 for *MESHGEN*. A listing of the program follows.

F. CUBIC SPLINE INTERPOLATION PROGRAM LISTING

```
c******program for generating the input data for nacelle geometry*****
      implicit real*8 (a-h,o-z)
      dimension xnodu(200),ynodu(200),xnodi(200),ynodi(200),xnodc(200)
```

```
      dimension ynodc(200),adshpu(100,3,2),adshpi(100,3,2)

      dimension adshpc(100,3,2),fractu(200),frac1(100),frac2(100)

c    xbaf = x coordinate of point where baffle starts

c    xtip = x coordinate of nacelle tip

c    ytip = y coordinate of nacelle tip

c    xfan = x coordinate of fan face

c    xcb = x coordinate of the end of centerbody

      read(5,*) nelu, nelc1, nelc2

      nelc = nelc1 + nelc2

      nodeu = 2*nelu + 1

      nodec = 2*nelc + 1

      nodec1 = 2*nelc1 + 1

      nodec2 = 2*nelc2 + 1

      read(5,*) xbaf, xtip, ytip, xfan, xcb

      read(5,*) (fractu(i),i=1,nelu+1)

      read(5,*) (frac1(i),i=1,nelc1+1)

      read(5,*) (frac2(i),i=1,nelc2+1)

c.....generating x coordinate nodal points on the upper nacelle surface

      do 20 i = 1, nelu

      xnodu(2*i-1) = xbaf + fractu(i)*(xtip - xbaf)

      xnodu(2*i+1) = xbaf + fractu(i+1)*(xtip - xbaf)

      xnodu(2*i) = (xnodu(2*i+1) + xnodu(2*i-1))/2.0d0

20    continue

      call spline(nodeu,xnodu,ynodu)

      do 30 i = 1, nelu

      adshpu(i,1,1) = xnodu(2*i-1)

      adshpu(i,1,2) = ynodu(2*i-1)
```

```fortran
      adshpu(i,2,1) = xnodu(2*i)

      adshpu(i,2,2) = ynodu(2*i)

      adshpu(i,3,1) = xnodu(2*i+1)

      adshpu(i,3,2) = ynodu(2*i+1)

      write(7,1001) adshpu(i,1,1),adshpu(i,1,2),adshpu(i,2,1),
   &  adshpu(i,2,2),adshpu(i,3,1),adshpu(i,3,2)

 30   continue
c......generate the highlight circle
c.....center of highlight circle

      chc = xtip - ytip

c.....radius of highlight circle

      radhc = dsqrt(2.0d0*ytip*ytip)

c..intercept of highlight circle with the x-axis

      xhci = chc + radhc

c.....generating x coordinate nodal points on the center body

      do 25 i = 1, nelc1

      xnodc(2*i-1) = xfan + frac1(i)*(xcb - xfan)

      xnodc(2*i+1) = xfan + frac1(i+1)*(xcb - xfan)

      xnodc(2*i) = (xnodc(2*i+1) + xnodc(2*i-1))/2.0d0

      write(6,*) 'xnodc(',2*i+1,')=', xnodc(2*i+1)

 25   continue
c.....generating x coordinate nodal points on the centerline

      ll = 0

      do 31 i = nelc1 + 1, nelc

      ll = ll + 1

      xnodc(2*i-1) = xcb + frac2(ll)*(xhci - xcb)

      xnodc(2*i+1) = xcb + frac2(ll+1)*(xhci - xcb)
```

119

```fortran
      xnodc(2*i) = (xnodc(2*i+1) + xnodc(2*i-1))/2.0d0

      write(6,*) 'xnodc(',2*i - 1,')=', xnodc(2*i- 1)

31    continue

      call spline(nodec,xnodc,ynodc)

      do 35 i = 1, nelc

      adshpc(i,1,1) = xnodc(2*i-1)

      adshpc(i,1,2) = ynodc(2*i-1)

      adshpc(i,2,1) = xnodc(2*i)

      adshpc(i,2,2) = ynodc(2*i)

      adshpc(i,3,1) = xnodc(2*i+1)

      adshpc(i,3,2) = ynodc(2*i+1)

35    continue

c

c....compute a new set of fractions for the nodal points on the lower

c....surface of the nacelle which have the same fractions as the

c..corresponding nodes on the c.b & centerline based on the entire length

      dist = xtip - xfan

      do 75 k = 1, nodec

      fracti = (xnodc(k) - xfan)/(xhci - xfan)

      xnodi(k) = xfan + fracti*dist

75    continue

c     do 76 k = nodec1 + 1, nodec

c     fracti(k) = frac2(k)*(xhci - xcb)/(xhci - xfan)

c     xnodi(k) = xfan + fracti(k)*dist

c 76  continue

      call spline(nodec,xnodi,ynodi)

      do 85 i = 1, nelc
```

120

```fortran
      adshpi(i,1,1) = xnodi(2*i-1)

      adshpi(i,1,2) = ynodi(2*i-1)

      adshpi(i,2,1) = xnodi(2*i)

      adshpi(i,2,2) = ynodi(2*i)

      adshpi(i,3,1) = xnodi(2*i+1)

      adshpi(i,3,2) = ynodi(2*i+1)

      write(7,1001) adshpi(i,1,1),adshpi(i,1,2),adshpi(i,2,1),
     &  adshpi(i,2,2),adshpi(i,3,1),adshpi(i,3,2)

 85   continue

      do 334 i = 1, nelc

      write(7,1001) adshpc(i,1,1),adshpc(i,1,2),adshpc(i,2,1),
     &  adshpc(i,2,2),adshpc(i,3,1),adshpc(i,3,2)

 334  continue

 1001 format(6f10.4)

      stop

      end

c*******************************************************************

c    to fit a curve through a set of points using cubic spline

c    interpolation.

c*******************************************************************

      subroutine spline(nnode,pt,spl)

      implicit real*8 (a-h,o-z)

      dimension x(100),f(100),b(100),ed(100),eu(100),el(100),dfp(100)

      dimension pt(200), spl(200)

c.......read the data points from the data file

      read(5,*) n

      read(5,*) (x(i),f(i),i=1,n+1)
```

```fortran
      do 10 i = 2, n
      if(i.eq.2) go to 6
      el(i-1) = x(i) - x(i-1)
6     ed(i-1) = 2.0d+00*(x(i+1) - x(i-1))
      if(i.eq.n) go to 7
      eu(i-1) = x(i+1) - x(i)
7     b(i-1) = 6.0d+00*(f(i+1) - f(i))/(x(i+1) - x(i))
     &  + 6.0d+00*(f(i-1) - f(i))/(x(i) - x(i-1))
10    continue
      n1 = n - 1
      call tridag(n1,ed,eu,el,b)
      write(6,*) 'the solution is'
      write(6,*) (b(i),i=1,n-1)
      dfp(1) = 0.0d0
      dfp(n+1) = 0.0d0
      do 70 i = 1, n-1
      dfp(i+1) = b(i)
70    continue
      do 75 k = 1, nnode
      do 80 i = 1, n
      if(pt(k).gt.x(i).and.pt(k).lt.x(i+1))then
      spl(k) = dfp(i)*((x(i+1)-pt(k))**3)/(6.0d0*(x(i+1)-x(i)))
     &  + dfp(i+1)*((pt(k)-x(i))**3)/(6.0d0*(x(i+1)-x(i)))
     &  + (f(i)/(x(i+1)-x(i))
     &  - dfp(i)*(x(i+1)-x(i))/6.0d0)*(x(i+1)-pt(k))
     &  + (f(i+1)/(x(i+1)-x(i)) - dfp(i+1)*(x(i+1)-x(i))/6.0d0)
     &  *(pt(k)-x(i))
```

```fortran
      else if(pt(k).eq.x(i)) then
      spl(k) = f(i)
      else if(pt(k).eq.x(i+1)) then
      spl(k) = f(i+1)
      else if(pt(k).gt.x(n+1)) then
      spl(k) = 0.0d0
      endif
80    continue
75    continue
      write(6,*) 'the calculated value is'
      write(6,*) (spl(k),k=1,nnode)
      return
      end
c
c*****************************************************************************
      subroutine tridag(n1,ed,eu,el,b)
      implicit real*8 (a-h,o-z)
      dimension ed(100),eu(100),el(100),b(100)
      m = n1 - 1
      do 1040 i = 1,m
      fa = el(i+1)/ed(i)
      ed(i+1) = ed(i+1) - fa*eu(i)
      b(i+1) = b(i+1) - fa*b(i)
1040  continue
      b(n1) = b(n1)/ed(n1)
      do 1070 i = 1,m
      b(n1-i) = (b(n1-i) - eu(n1-i)*b(n1-i+1))/ed(n1-i)
```

```
1070   continue

       return

       end
```

APPENDIX B

MATHEMATICAL NOTATIONS

$\psi : \Omega \longrightarrow \mathbf{R}$ = ψ is a real valued function defined on the domain Ω which is one-dimensional

$\psi : \Omega \longrightarrow \mathbf{R^2}$ = ψ is a real valued function defined on the domain Ω which is two-dimensional

$\psi : \Omega \longrightarrow \mathbf{C^2}$ = ψ is a complex valued function defined on the domain Ω which is two-dimensional

$[0, r_o]$ = an interval between and including the values of 0 and r_o

$\ni$ = such that

$\forall$ = for every

$\cup$ = symbol representing union of two sets

H^1 = Hilbert space; the space of functions which are square integrable, which, in other words, implies that the functions are continuous, but their derivatives are piecewise continuous

BIBLIOGRAPHY

1. Astley, R. J., and W. Eversman, "A Finite Element Method for Transmission in Non-uniform Ducts without Flow: Comparison with the Method of Weighted Residuals", *Journal of Sound and Vibration*, 57(3), pp. 367-388, 1978.

2. Eversman, W., R. J. Astley, and V. P. Thanh, "Transmission in Non-uniform Ducts - A Comparative Evaluation of Finite Element and Weighted Residuals Computational Schemes", *AIAA* 77-1299.

3. Majjigi, R. K., R. K. Sigman, and B. T. Zinn, "Wave Propagation in Ducts using the Finite Element Method," *AIAA* 79-0965.

4. Tag, I., and E. Lumsdaine, "An Efficient Finite Element Technique for Sound Propagation in Axisymmetric Hard Wall Ducts Carrying High Subsonic Mach Number Flow," *AIAA* 78-1154.

5. Baumeister, K. J., "Application of the Velocity Potential Function to Acoustic Duct Propagation and Radiation from Inlets using Finite Element Theory," *AIAA* 79-0680.

6. Eversman, W., and R. J. Astley, "Acoustic Transmission in Non-Uniform Ducts with Mean Flow. Part I: The Method of Weighted Residuals," *Journal of Sound and Vibration*, 74(1), pp. 89-101, 1981.

7. Walkington, N.J., and W. Eversman, "Finite Difference Solutions to Shocked Acoustic Waves," *AIAA* 83-0671.

8. Walkington, N.J., "A Numerical Model for Subsonic Acoustic Choking", Ph.D. Dissertation, University of Missouri-Rolla, 1983.

9. Ville, J. M., and R. J. Silcox, "Experimental Investigation of the Radiation of Sound from an Unflanged Duct and a Bellmouth, Including the Flow Effect," *NASA Technical Paper* 1697.

10. Silcox, R. J., "Experimental Investigation of Geometry and Flow Effects on the Acoustic Radiation from Duct Inlets," *AIAA* 83-0713.

11. Kempton, A. J., and M. G. Smith, "Ray Theory Predictions of the Sound Radiated from Realistic Engine Inlets," *AIAA* 81-1987

12. Meyer, W. L., W. A. Bell, and B. T. Zinn, "Sound Radiation from Finite Length Axisymmetric Ducts and Engine Inlets," *AIAA* 79-0675.

13. Meyer, W. L., B. R. Daniel, and B. T. Zinn, "Acoustic Radiation from Axisymmetric Ducts - A Comparison of Theory and Experiment," *AIAA* 80-0097.

14. Horowitz, S. J., R. K. Sigman, and B. T. Zinn, "An Iterative Finite Element-Integral Technique for Predicting Sound Radiation from Turbofan Inlets," *AIAA* 81-1987.

15. Horowitz, S. J., R. K. Sigman, and B. T. Zinn, "An Iterative Finite Element-Integral Technique for Predicting Sound Radiation from Turbofan Inlets in Steady Flight," *AIAA* 82-0124.

16. Baumeister, K. J., "Utilizing Numerical Techniques in Turbofan Inlet Acoustic Suppressor Design," *NASA TM* 82994.

17. Astley, R. J., and W. Eversman, "Finite Element Formulations for Acoustical Radiation," *Journal of Sound and Vibration*, 88(1), pp. 47-64, 1983.

18. Bettess, P., "Infinite Elements," *International Journal for Numerical Methods in Engineering*, Vol. 11 , pp. 53-64, 1977.

19. Astley, R. J., and W. Eversman, "Wave Envelope and Infinite Element Schemes for Fan Noise Radiation from Turbofan Inlets," *AIAA* 83-0709.

20. Astley, R. J., "Acoustical Radiation in Moving Flows: A Finite Element Approach," *Proceedings of the 1983 International Conference on Computational Techniques and Applications, Sydney, Australia*, 1983, pp. 685-698.

21. Eversman, W., A. V. Parrett, J. S. Preisser, and R. J. Silcox, "Contributions to the Finite Element Solution of the Fan Noise Radiation Problem," *ASME* 84-WA/NCA-1.

22. Irons, B. M., "A Frontal Solution Program for Finite Element Analysis," *International Journal for Numerical Methods in Engineering*, Vol. 2, pp. 5-32, 1970.

23. Preisser, J. S., R. J. Silcox, W. Eversman, and A. V. Parrett, "A Flight Study of Tone Radiation Patterns Generated by Inlet Rods in a Small Turbofan Engine," *AIAA* 84-0499, 1984.

24. Parrett, A. V., and W. Eversman, "Wave Envelope and Finite Element Approximations for Turbofan Noise Radiation in Flight," *AIAA Journal*, Vol. 24, No. 5, May 1986.

25. Lieblein, S., and, N. O. Stockman, "Compressibility Corrections for Internal Flow Solutions," *Journal of Aircraft*, Vol. 9, No. 4, pp. 312-313.

26. Astley, R. J., and W. Eversman, "Acoustic Transmission in Non-Uniform Ducts With Mean Flow, Part II: The Finite Element Method," *Journal of Sound and Vibration*, 74(1), pp. 103-121.

27. Becker E., G. F. Carey, and J. T. Oden, *"Finite Elements*: An Introduction," Prentice-Hall, Inc., Englewood Cliffs, NJ, 1981.

ACOUSTIC RADIATION CODE
INSTALLATION NOTES

H. D. Meyer
United Technologies Corporation
Hamilton Standard Division
Windsor Locks, Connecticut

August 1992

ACOUSTIC RADIATION CODE
INSTALLATION NOTES

INTRODUCTORY REMARKS

The Acoustic Radiation Code is a FORTRAN program used to study far field radiation from turbofan engines. It was developed for the IBM (tm) mainframe at the University of Missouri-Rolla, under the direction of Professor Walter Eversman. It has subsequently been modified at Hamilton Standard to run on Sun (tm) and Silicon Graphics Iris (tm) UNIX (tm) workstations.

The program consists of five separate modules. These are run, one after the other, in the order of their listing in the next section. However, PRATPREH, the first of these, may not always be used.

The purpose of these notes is to assist users in the installation of the code on either of the two above-mentioned workstations. In the pages that follow, there is a brief description of the modules making up the program and then brief descriptions of how to compile, run, and test these modules.

For further details, refer to Appendix A.

ACOUSTIC RADIATION CODE MODULES

Five modules have been provided for installation:

PRATPREH

- ► Generates cards 3-5 of the PRATMESH.INP input to PRATMESHH (i.e., the coordinates of the element nodes for the upper nacelle, center body and lower nacelle)

129

PRATMESHH

- ► Generates the finite element mesh used for both flow and acoustic solutions

- ► Calculates the duct eigenvalues and eigenfunctions used for acoustic calculations

PRATFLOWH

- ► Obtains the potential flow solutions

PRATVELH

- ► Provides a superposition of the solutions above with a uniform mean flow to give the final flow needed by PRATRADH

PRATRADH

- ► Generates the acoustic solution for two-dimensional or cylindrically symmetric nacelles

Note that the equivalent University of Missouri-Rolla IBM (tm) mainframe versions of these modules are designated PRATPRE, PRATMESH, PRATFLOW, PRATVEL, and PRATRADA. An "H" for Hamilton has been added to the names of the workstation versions (or in the case of PRATRADA, the final "A" has been changed to "H"), to distinguish between the two versions.

TO COMPILE

PRATPREH

f77 -o pratpreh -O pratpreh.f   (Sun)

f77 -o pratpreh -O -old_rl pratpreh.f   (SGI)

PRATMESHH

f77 -o pratmeshh -O pratmeshh.f   (Sun)

f77 -o pratmeshh -O -old_rl pratmeshh.f   (SGI)

PRATFLOWH

   f77 -o pratflowh -O pratflowh.f   (Sun)

   f77 -o pratflowh -O -old_rl pratflowh.f   (SGI)

PRATVELH

   f77 -o pratvelh -O pratvelh.f   (Sun)

   f77 -o pratvelh -O -old_rl pratvelh.f   (SGI)

PRATRADH

   f77 -o pratradh -O pratradh.f   (Sun)

   f77 -o pratradh -O -Olimit 1100 -old_rl pratradh.f (SGI)

TO RUN

PRATPREH

   (pratpreh < pratpre.inp > pratpre.out) >& pratpre.err &
       (fort.5)   (fort. 6)   (stderr)

Files Generated:

* fort.7   - Cards 3-5 for pratmesh.inp   (3.3 Kb)
* pratpre.out - Numeric output data   (9 Kb)
* pratpre.err - System error messages

PRATMESHH

   (pratmeshh < pratmesh.inp > pratmesh.out) >& pratmesh.err &
       (fort.5)   (fort.6)   (stderr)

Files Generated:

* fort.14   - PostScript plot file   (450 Kb)
* fort.20   - Needed as input by all other modules (732 Kb)
* pratmesh.out - Numeric output data   (360 Kb)
* pratmesh.err - System error messages

PRATFLOWH

(pratflowh < pratflow.inp > pratflow.out) >& pratflow.err &
           (fort.5)   (fort.6)   (stderr)

Note: fort.20, generated by PRATMESHH, must be
       available as UNIT=20 input.

Files Generated:

* fort.2-4, 8	- Work files; delete	(6.5 Mb total)
& 5 tmp files	the fort.2-4, 8 ones	
	at end of run	
* fort.14	- PostScript plot file	(1.6 Mb)
* fort.21	- Needed as input by PRATVELH	(195 Kb)
* pratflow.out	- Numeric output data	(196 Kb)
* pratflow.err	- System error messages	

PRATVELH

(pratvelh < pratvel.inp > pratvel.out) >& pratvel.err &
           (fort.5)   (fort.6)   (stderr)

Note: fort.20, generated by PRATMESHH, and fort.21,
       generated by PRATFLOWH, must be available,
       respectively, as UNIT=20 and UNIT=21 input.

Files Generated:

* 4 tmp files	- Work files	(443 Kb total)
* fort.14	- PostScript plot file	(513 Kb)
* fort.22	- Needed as input by PRATRADH	(700 Kb)
* pratvel.out	- Numeric output data	(13 Kb)
* pratvel.err	- System error messages	

PRATRADH

(pratradh < pratrad.inp > pratrad.out) >& pratrad.err &
           (fort.5)   (fort.6)   (stderr)

Note: fort.20, generated by PRATMESHH, and fort.22,
       generated by PRATVELH, must be available,
       respectively, as UNIT=20 and UNIT=22 input.

Files Generated:

* fort.3, 4 & 5 tmp files	- Work files; delete the fort 3, 4 ones at end of run	(70 Mb total)
* fort.14	- PostScript plot file	(1 Mb per case)
* fort.23 (and fort.24-27, one for each additional case that is run)	- Used previously for additional plotting; not needed for the present setup, so can be deleted	(15 Kb per case)
* pratrad.out	- Numeric output data	(107 Kb per case)
* pratrad.err	- System error messages	

Note that the plot files, fort.14, are easily plotted using a standard PostScript printer. They also can be previewed on a monitor if a PostScript viewing utility is available.

A test case has been provided to check each of the five Acoustic Radiation Code modules. For test purposes, PRATPREH can be run independently. However, the other programs should be run in sequence with the output (i.e., fort.20, fort.21, fort.22) of one feeding into the next. The test input files to use have the same names as those used in the "To Run" instructions above (i.e., pratpre.inp, pratmesh.inp, pratflow.inp, pratvel.inp, pratrad.inp).

Output data (fort.7) from the PRATPRE test run should be as follows:

```
0.0000  1.2000  0.0225  1.2000  0.0450  1.2000
0.0450  1.2000  0.0675  1.2000  0.0900  1.2000
0.0900  1.2000  0.1125  1.2000  0.1350  1.2000
0.1350  1.2000  0.1575  1.2000  0.1800  1.2000
0.1800  1.2000  0.2025  1.2000  0.2250  1.2000
0.2250  1.2000  0.2475  1.2000  0.2700  1.2000
0.2700  1.2000  0.2925  1.2000  0.3150  1.2000
0.3150  1.2000  0.3375  1.2000  0.3600  1.2000
0.3600  1.2000  0.3825  1.2000  0.4050  1.2000
0.4050  1.2000  0.4275  1.2000  0.4500  1.2000
0.4500  1.2000  0.4725  1.2000  0.4950  1.2000
0.4950  1.2000  0.5175  1.2000  0.5400  1.2000
0.5400  1.2000  0.5625  1.2000  0.5850  1.2000
0.5850  1.2000  0.6075  1.1999  0.6300  1.1995
0.6300  1.1995  0.6525  1.1985  0.6750  1.1968
0.6750  1.1968  0.6975  1.1946  0.7200  1.1917
0.7200  1.1917  0.7425  1.1880  0.7650  1.1835
0.7650  1.1835  0.7875  1.1781  0.8100  1.1714
0.8100  1.1714  0.8325  1.1632  0.8550  1.1527
0.8550  1.1527  0.8662  1.1460  0.8775  1.1381
0.8775  1.1381  0.8887  1.1269  0.9000  1.1000
0.0000  1.0000  0.0207  1.0000  0.0415  1.0000
0.0415  1.0000  0.0622  1.0000  0.0830  1.0000
0.0830  1.0000  0.1037  1.0000  0.1245  1.0000
0.1245  1.0000  0.1452  1.0000  0.1660  1.0000
0.1660  1.0000  0.1867  1.0000  0.2075  1.0000
0.2075  1.0000  0.2282  1.0000  0.2490  1.0000
0.2490  1.0000  0.2697  1.0000  0.2905  1.0000
0.2905  1.0000  0.3112  1.0000  0.3319  1.0000
0.3319  1.0000  0.3518  1.0000  0.3717  1.0000
0.3717  1.0000  0.3916  1.0000  0.4115  1.0000
0.4115  1.0000  0.4314  1.0000  0.4512  1.0000
0.4512  1.0000  0.4711  1.0000  0.4910  1.0000
0.4910  1.0000  0.5109  1.0000  0.5308  1.0000
0.5308  1.0000  0.5506  1.0000  0.5705  1.0000
0.5705  1.0000  0.5904  1.0000  0.6103  1.0001
0.6103  1.0001  0.6302  1.0006  0.6501  1.0014
0.6501  1.0014  0.6699  1.0027  0.6898  1.0046
0.6898  1.0046  0.7097  1.0069  0.7296  1.0098
0.7295  1.0098  0.7495  1.0133  0.7693  1.0175
0.7693  1.0175  0.7892  1.0224  0.8091  1.0283
0.8091  1.0283  0.8290  1.0354  0.8489  1.0441
0.8489  1.0441  0.8588  1.0495  0.8688  1.0556
0.8688  1.0556  0.8844  1.0685  0.9000  1.1000
0.0000  0.3000  0.0312  0.2911  0.0625  0.2818
0.0625  0.2818  0.0938  0.2716  0.1250  0.2601
0.1250  0.2601  0.1562  0.2471  0.1875  0.2328
0.1875  0.2328  0.2188  0.2172  0.2500  0.2003
0.2500  0.2003  0.2812  0.1819  0.3125  0.1619
0.3125  0.1619  0.3438  0.1402  0.3750  0.1166
0.3750  0.1166  0.4062  0.0911  0.4375  0.0635
0.4375  0.0635  0.4688  0.0332  0.5000  0.0000
0.5000  0.0000  0.5299  0.0000  0.5599  0.0000
0.5599  0.0000  0.5898  0.0000  0.6198  0.0000
0.6198  0.0000  0.6497  0.0000  0.6797  0.0000
0.6797  0.0000  0.7096  0.0000  0.7396  0.0000
0.7396  0.0000  0.7595  0.0000  0.7995  0.0000
0.7995  0.0000  0.8294  0.0000  0.8594  0.0000
0.8594  0.0000  0.8893  0.0000  0.9193  0.0000
0.9193  0.0000  0.9492  0.0000  0.9792  0.0000
0.9792  0.0000  1.0091  0.0000  1.0390  0.0000
1.0390  0.0000  1.0690  0.0000  1.0989  0.0000
1.0989  0.0000  1.1289  0.0000  1.1588  0.0000
1.1588  0.0000  1.1888  0.0000  1.2187  0.0000
1.2187  0.0000  1.2487  0.0000  1.2786  0.0000
1.2786  0.0000  1.2936  0.0000  1.3086  0.0000
1.3086  0.0000  1.3321  0.0000  1.3556  0.0000
```

Output plots from runs of the remaining modules should match those shown below. Note that plots here are reduced in size. The actual ones will be 8½" x 11".

PRATMESHH

PRATFLOWH

PRATVELH

137

ACOUSTIC POTENTIAL

FLOW MACH NUMBER: -0.30
INLET MACH NUMBER: -0.50

ADMITTANCE REAL: 0.24
ADMITTANCE IMAG: 0.09
REDUCED FREQUENCY: 25.00
ANGULAR MODE: 25

R/A

X/A

SPL DIRECTIVITY

FLOW MACH NO.   -0.30
INLET MACH NO.   -0.50
WAVE NO.   25.00
ANGULAR MODE NO.   25
ADMITTANCE REAL   0.240
ADMITTANCE IMAG   0.094

RELATIVE SPL (DB) AT R= 100 INLET RADII

ANGLE (DEG) OFF AXIS

138

PRESSURE DIRECTIVITY

FLOW MACH NO.	-0.30
INLET MACH NO.	-0.50
WAVE NO.	25.00
ANGULAR MODE NO.	25
ADMITTANCE REAL	0.240
ADMITTANCE IMAG	0.094

RELATIVE PRESSURE AT R= 100 INLET RADII

ANGLE (DEG) OFF AXIS

ADMITTANCE REAL	0.240
ADMITTANCE IMAG	0.094
FLOW MACH NO.	-0.30
INLET MACH NO.	-0.50
WAVE NO.	25.00
ANGULAR MODE NO.	25

RELATIVE SPL (DB) AT R= 10.0 INLET RADII

POLAR SPL DIRECTIVITY

139

ACOUSTIC PRESSURE

FLOW MACH NUMBER: -0.30
INLET MACH NUMBER: -0.50

ADMITTANCE REAL: 0.24
ADMITTANCE IMAG: 0.09
REDUCED FREQUENCY: 25.00
ANGULAR MODE: 25

X/A